Politecnico di Torino

Corso di Laurea Ingegneria Energetica e Nucleare
A.a. 2024/2025
Novembre 2025

Techno-economic analysis of Methanol-Based Electricity and Hydrogen Production

Tutors:
Marta Gandiglio
Vladimir Luis Meca López

Candidate:
Azzurra D'Ascanio

Table of Contents

1 INTRODUCTION 1-7

1.1 Carbon emission and global warming 1-7
1.2 Role of Hydrogen and derivates in the energy transition 1-7
1.3 Methanol as Hydrogen carrier 1-8
1.4 Technologies for Carbone Capture and Storage 1-10

2 STATE OF THE ART 2-10

2.1 Maritime transport of methanol 2-10
2.2 Direct Methanol Fuel Cell 2-12
2.2.1 Working principle 2-13
2.2.2 Components 2-15
2.3 Methanol Electrolysis Cell 2-16
2.4 CO_2 capture and storage 2-17
2.4.1 Amines 2-18
2.4.2 Zeolites 2-19

3 METHODOLOGY FOR TECHNO-ECONOMIC ANALYSIS 3-21

3.1 Desalination treatment plant 3-21
3.2 Water Electrolysis plant 3-23
3.3 Methanol synthesis plant 3-25
3.4 Methanol storage facility 3-26
3.5 Methanol carrier ship 3-26
3.6 Direct methanol fuel cell plant 3-29
3.7 Methanol electrolysis plat 3-34
3.8 Carbon capture 3-35

4 EXPERIMENTAL PROCEDURE 4-37

4.1 Nafion 117 membrane treatment 4-37
4.2 MEA and single cell assembly 4-39
4.3 DMFC test bench 4-41
4.4 CO2 emission measurement test bench 4-43

5 RESULTS AND DISCUSSION 5-44

5.1 Polarization curves and power curves 5-44
5.1.1 DMFC 1 5-45
5.1.2 DMFC 2 5-47
5.1.3 DMFC 3 5-49
5.1.4 DMFC 4 5-51
5.1.5 DMFC 5 5-52
5.1.6 DMFC 6 5-54
5.2 Efficiencies 5-56
5.3 CO2 emissions 5-59
5.4 Economic analysis 5-61
5.4.1 Analysis of system facilities and scenario comparison 5-63
5.4.2 Sensitivity and cost-reduction analysis 5-75

6 CONCLUSION 6-79

7 REFERENCES 7-83

List of Figures

Figure 1. Circular carbon utilization ecosystem to produce net-zero fuels using RES [8] 1-8
Figure 2. Circular economy applied for the e-methanol (PowerPoint) 1-9
Figure 3. Diagram of use of methanol as energy vector and hydrogen carrier [42] 2-11
Figure 4. Schematic diagram Direct Methanol Fuel Cell (PowerPoint) 2-14
Figure 5. Schematic diagram Methanol Electrolysis Cell (PowerPoint) 2-17
Figure 6. Costs per unit of CO2 capture for the minimum cost design at 90% recovery [39] 3-37
Figure 7. (7.1) and (7.2) Heater with the crystallizer containing the 30% hydrogen peroxide solution and the two Nafion membranes; (7.3) Thermostatic bath in which is placed the beaker with the membranes and a thermometer. 4-39
Figure 8. Anode and Cathode after the coating spray with liquid Nafion on the catalyst layer 4-40
Figure 9. (9.1) Heated press for the MEA treatment at 130°C and 60 bar; (9.2) Close-up of the MEA inside the press 4-40
Figure 10. Schematic diagram of the DMFC test benchmark (PowerPoint) 4-42
Figure 11. DMFC positioned in the double insulating chamber and the cryothermostat heating the cell 4-43
Figure 12. Gas-liquid separator connected to the anode output of CO2/water mixture 4-44
Figure 13. Gas cromatograph used for the CO2 measurements 4-44
Figure 14. (14.1) Polarization curves and (14.2) Power curves measured in the first day for the DMFC 1(Excel) 5-45
Figure 15. (15.1) Polarization curves and (15.2) Power curves measured in the last day for the DMFC 1(Excel) 5-46
Figure 16. Best curve measured for the DMFC 1(Excel) 5-47
Figure 17. (17.1) Polarization curves and (17.2) Power curves measured in the first day for the DMFC 2 (Excel) .. 5-47
Figure 18. (18.1) Polarization curves and (18.2) Power curves measured in the last day for the DMFC 2 (Excel) 5-48
Figure 19. Best curve measured for the DMFC 2 (Excel) 5-48
Figure 20. (20.1) Polarization curves and (20.2) Power curves measured in the first day for the DMFC 3 (Excel) .. 5-49
Figure 21. (21.1) Polarization curves and (21.2) Power curves measured in the last day for the DMFC 3 (Excel) 5-50
Figure 22. Best curve measured for the DMFC 3 (Excel) 5-50
Figure 23. (23.1) Polarization curves and (23.2) Power curves measured in the first day for DMFC 4 (Excel) 5-51
Figure 24. (24.1) Polarization curves and (24.2) Power curves measured in the last day for DMFC 4 (Excel) 5-51
Figure 25. Best curve measured for DMFC 4 (Excel) 5-52
Figure 26. (26.1) Polarization curves and (26.2) Power curves measured in the first day for DMFC 5 (Excel) 5-53
Figure 27. (27.1) Polarization curves and (27.2) Power curves measured in the last day for DMFC 5 (Excel) 5-53
Figure 28. Best curve measured for DMFC 5 (Excel) 5-54
Figure 29. (29.1) Polarization curves and (29.2) Power curves measured in the first day for DMFC 6 (Excel) 5-54
Figure 30. (30.1) Polarization curves and (30.2) Power curves measured in the last day for DMFC 6 (Excel) 5-55
Figure 31. Best curve measured for DMFC 6 (Excel) 5-55
Figure 32. Chronovoltammetry test at 0,8A for 30min (Excel) 5-60
Figure 33. Time-Voltage graph from galvanostatic test (Excel) 5-60
Figure 34. LCOE contribution by component for DMFC 6 (Excel) 5-70
Figure 35. LCOE contribution by component for DMFC DURAMET [25] (Excel) 5-71
Figure 36. LCOE contribution by component for DMFC Efoy Pro 12000 Duo [40] (Excel) 5-72
Figure 37. LCOH contribution by component (Excel) 5-74
Figure 38. LCOE sensitivity to the methanol price (Excel) 5-76
Figure 39. LCOH sensitivity to electricity price (Excel) 5-77
Figure 40. LCOE sensitivity to methanol price, showing the cases with reduced storage costs (Excel) 5-78
Figure 41. LCOH sensitivity to methanol price, showing the cases with reduced storage costs (Excel) 5-79

List of Tables

Table 1. Advantages and disadvantages of absorption and adsorption methods (Excel) [35] 2-21
Table 2. Assumptions for the desalination treatment plant (Excel) [32] 3-23
Table 3. Assumptions for the water electrolysis plant (Excel) [32] 3-25
Table 4. Assumptions for a methanol synthesis plant (Excel) [32] 3-26
Table 5. Assumptions for methanol storage facilities (Excel) [32] 3-26
Table 6. Assumptions for a methanol fleet (Excel) [32] 3-29
Table 7. Costs estimation of the DURAMET stack prototype in a small-scale production (excel) [25] 3-30
Table 8. Costs of raw material for the components of a single unit in a large-scale production (Excel) [25] 3-31
Table 9. Investment in machinery for stack production (Excel) [25] 3-31
Table 10. Assumptions for methanol electrolysis plant (Excel) [32] 3-35
Table 11. Physical properties of the 13X zeolite [36] 3-36
Table 12. Technical comparison between the MEA absorption and the 13X zeolite adsorption (Excel) [35] 3-36
Table 13. Anode flow field plate characteristcs (Excel) 4-41
Table 14. Maximum power point (mpp) parameters for the best performing curve of each DMFC and reactant flow rates, both stoichiometric and real (Excel) 5-57
Table 15. Fuel utilization (FU) and efficiency values for each DMFC, based on the maximum power point conditions (Excel) 5-58
Table 16. Results obtained for the chronovoltammetry test: stoichiometric methanol and CO2 moles, CO2 produced in grams and CO2 emission in grams per kWh (Excel) 5-61
Table 17. Desalination plant results (Excel) 5-63
Table 18. Water electrolysis plant results (Excel) 5-64
Table 19. Methanol synstesis plant results (Excel) 5-65
Table 20. Methanol storage costs (Excel) 5-65
Table 21. Methanol transport results (Excel) 5-66
Table 22. Costs for stack and module with DMFC 6 from laboratory test and DMFC from reference [25] (Excel) . 5-67
Table 23. DMFC plants results with laboratory fuel cell 6 and reference [25] fuel cell (Excel) 5-67
Table 24. Costs and results for plant with DMFC Efoy Pro 12000 Duo [40] (Excel) 5-68
Table 25. CCS plant results for DMFC 6 from laboratory test (Excel) 5-69
Table 26. CCS plant results for DMFC DURAMET [25] (Excel) 5-69
Table 27. CCS plant results for DMFC Efoy Pro 12000 Duo [40] (Excel) 5-69
Table 28. LCOE cost breakdown for DMFC 6 from laboratory test (Excel) 5-70
Table 29. LCOE cost breakdown for DMFC DURAMET [25] (Excel) 5-71
Table 30. LCOE cost breakdown for DMFC Efoy Pro 12000 Duo [40] (Excel) 5-72
Table 31. Methanol Electrolysis cell plant results (Excel) 5-73
Table 32. CCS plant results for MEC plant (Excel) 5-74
Table 33. LCOH cost breakdown (Excel) 5-74
Table 34. Methanol storage cost for different tank capacities from literature data (Excel) 5-78

Abstract

The aim of this study is to carry out a techno-economic analysis of the methanol supply chain for hydrogen and electricity production. This includes the transportation of methanol to coastal areas via ships and its subsequent utilization in either a Direct Methanol Fuel Cell (DMFC) or a Methanol Electrolysis Cell (MEC).

In the first case, experimental tests will be carried out in the laboratory on various single-cell DMFC prototypes, under the same operating conditions but with different anode plate active area geometries.

For the MECs, previously acquired experimental data from the same laboratory will be used. In both cases, the collected data will be used to perform an economic analysis aimed at determining the production cost of electricity and hydrogen.

Additionally, the study will include a theoretical assessment of carbon capture and storage (CCS), initially considering both zeolite and amine technologies. The focus will then shift specifically to zeolites, particularly zeolite 13X. A laboratory experiment will also be conducted in this context to quantify the amount of CO_2 in the output stream of a DMFC single cell.

1 INTRODUCTION

1.1 Carbon emission and global warming

In recent years, the world has been shifting from the use of fossil fuels to renewable energy sources. The increase in anthropogenic greenhouse gas (GHG) emissions, driven by economic growth and population growth, is contributing to global warming with devastating environmental effects. In particular, CO_2 is the most abundant GHG in the atmosphere, as it has the longest lifetime compared to other GHGs and because deforestation has reduced a part of the CO_2 sink. This means that once CO_2 is in the atmosphere, it can take many years (from 5 to 200 years) to reach equilibrium. Therefore, in addition to reducing future emissions, it is crucial to remove the CO_2 currently present in the atmosphere via Direct Carbon Capture (DACC) [1, 2].

As stated in the Fifth Assessment Report of the Intergovernmental Panel on Climate Change (IPCC), eliminating CO_2 emissions would lead to a nearly stable global temperature for centuries due to the climate system's significant inertia and the slow dynamics of the carbon cycle [4]. The emissions accumulated since the Industrial Revolution are the primary cause of current global warming, with atmospheric CO_2 concentrations rising from 280 ppm to 417 ppm by 2022. The largest sources of CO_2 emissions include industrial plants, such as cement and ammonia production facilities, as well as thermal power plants [4,10].

In the 2015 Paris Climate Agreement, global leaders committed to limiting global warming to 2°C, or ideally 1,5°C, above pre-industrial levels [3]. Subsequently, the 2019 European Green Deal set an ambitious target of reducing GHG emissions by at least 55% compared to 1990 levels. Another key objective is to achieve carbon neutrality (net-zero emissions) across the EU by 2050. To meet these goals, the rapid development of clean and efficient technologies is essential, including renewable energy, electrification, and the replacement of fossil fuels in sectors that are difficult to electrify [5]. Given the expected rise in population and the increasing electrification of end users coupled with the increasing of the quality of life, energy demand is expected to grow significantly [6,18]. This underscores the need to generate power cleanly and store it efficiently.

1.2 Role of Hydrogen and derivates in the energy transition

In the context of the energy transition, the main objectives are RES energy-to-X conversion, electrification of end uses, CO_2 management, mitigation and reuse (CCSU), and the use of energy carriers such as hydrogen and its derivatives.

One of the main challenges of renewable energy sources is their intermittency and uneven geographic distribution. Therefore, it is crucial to have an energy carrier that enables the transport and storage of renewable energy, ultimately eliminating the

reliance on fossil fuels [7]. Several pathways exist to convert renewable energy into the so-called platform molecules (H_2 and CO_2), which can be used for transportation, storage, and the production of other chemicals. These include electrochemical conversion, thermochemical conversion, photocatalytic conversion, and biological conversion.

Hydrogen and its derivatives are particularly important in sectors where electrification is challenging, such as international shipping, aviation, chemicals, steel production, and seasonal energy storage. By storing renewable energy in molecular form, it can later be retrieved through thermal or electrochemical processes when needed.

Beyond hydrogen, synthetic hydrocarbons such as methanol, formic acid, and methane can also serve as storage molecules. These are particularly valuable because they allow industries to reuse carbon emissions, enabling the production of net-zero fuels through Carbon Capture and Utilization (CCU). Using hydrocarbons as energy storage solutions simultaneously addresses industrial emission reductions and renewable energy storage challenges while providing highly demanded raw material in the market, such as methanol [8].

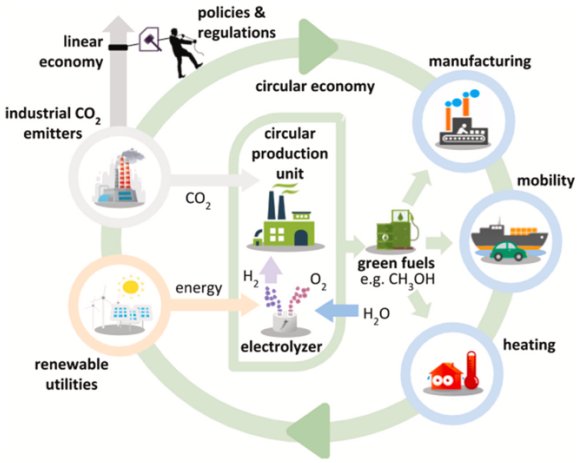

Figure 1. Circular carbon utilization ecosystem to produce net-zero fuels using RES [8]

Based on the points mentioned earlier, it is evident that the transition is moving toward a circular economy model, which is essential for reducing carbon emissions alongside the adoption of renewable energy. By reusing industrial emissions and waste, it is possible to create commercial products (such as plastics and concrete) or chemicals that can serve also as energy sources, such as methanol in direct methanol fuel cells (DMFC) [8].

1.3 Methanol as Hydrogen carrier

Focusing on methanol, it is particularly interesting as it can function both as a hydrogen storage molecule and as a direct source of electricity generation. Additionally, methanol

is a well-established material that can be produced using high Technology Readiness Level (TRL) technologies with hydrogen and CO_2. It serves not only as an energy carrier but also as a key chemical feedstock and a marine fuel, making it particularly valuable for the shipping industry [9].

Methanol has a wide range of applications in the chemical industry, with an annual production of over 100 million tons in 2020 [15]. It is currently regarded as a promising future fuel for maritime applications and can also be used to produce jet fuel for the aviation sector [9].

This study will analyze both cases: hydrogen production via methanol electrolysis cells (MEC) and electricity generation through direct methanol fuel cells (DMFC). Methanol is particularly advantageous because it enables both hydrogen storage and the reutilization of captured CO_2. Moreover, it can be produced in locations where renewable energy is more affordable and efficiently transported by ship. However, one of its drawbacks is that CO_2 is emitted during both the MEC and DMFC processes. This highlights the necessity of carbon capture and storage (CCS) in both cases.

From the perspective of a circular supply chain, one possible approach is to return the captured CO_2 to the site where methanol is produced so that it can be reused [7].

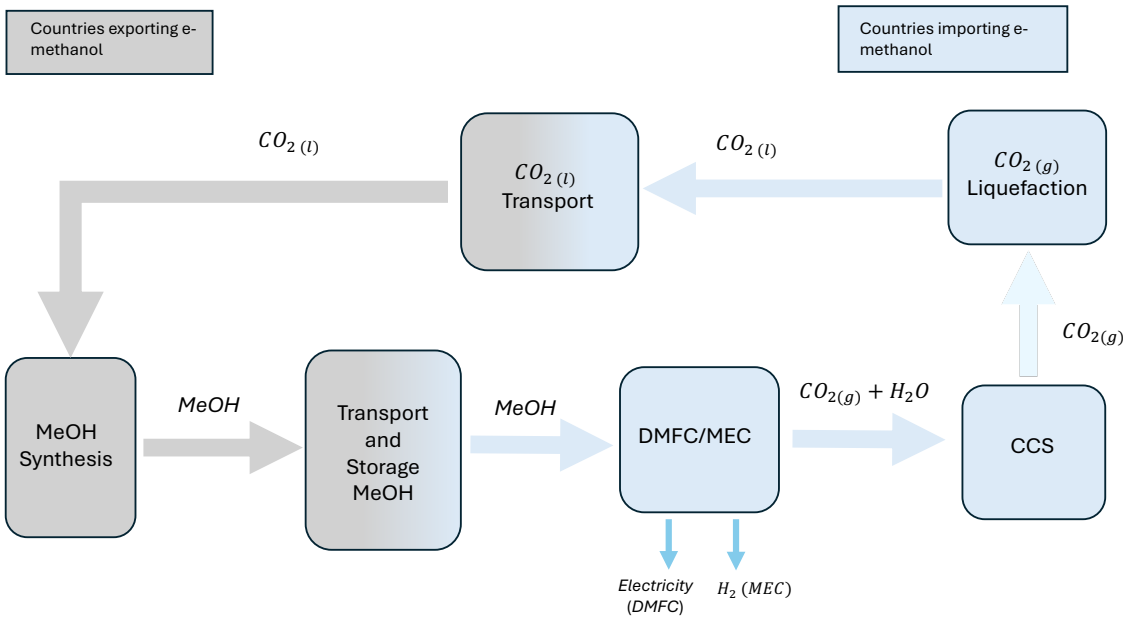

Figure 2. Circular economy applied for the e-methanol (PowerPoint)

It is possible to reuse the captured CO_2 to produce methanol again, thereby closing the cycle, like shown in *Figure 2*. Chong Wei Ong et al. [7] investigated the feasibility of this closed-carbon-cycle international renewable energy supply chain. However, in their study, methanol was converted back into hydrogen via steam reforming.

1.4 Technologies for Carbone Capture and Storage

Regarding the CCS, this study will focus on the methods using amines and zeolites from a theoretical perspective, based on the CO_2 emission stream obtained from the experiment.

Chemical absorption of CO_2 using an aqueous monoethanolamine (MEA) solution (20-30%) is a mature technology dating back to the 1930s and is widely used in various chemical industries. It is known for its fast absorption rate and high CO_2 capture capacity [10]. This method is primarily employed for post-combustion carbon capture, meaning it treats flue gases emitted from industrial plants and power stations. This approach is particularly useful for retrofitting existing industrial plants. The process involves passing the flue gas through two reactors: the first is an absorber (stripper/scrubber), where the gas flows countercurrent to the MEA solution, allowing CO_2 absorption. The second is a regenerator, where heat is supplied to release a purer CO_2 stream, regenerating the solution for reuse in a new cycle. However, MEA based carbon capture has several drawbacks, including the high heat duty required for regeneration, significant solvent degradation, and its corrosive nature [3, 11, 12].

A recently developed alternative for CCS involves the use of solid adsorbent materials, with the most promising being carbon-based materials, zeolites, and metal-organic frameworks (MOFs). Solid materials have gained significant attention due to their easier regeneration process since CO_2 is adsorbed physically rather than chemically, as with liquid solvents [3].

An ideal CO_2 adsorbent should possess the following properties: high CO_2 adsorption capacity, high CO_2 selectivity, fast adsorption/desorption kinetics, and easy regeneration. For what concerns the zeolites, they exhibit different structural types depending on the size and shape of their channels and cages, categorized as medium and large-pore zeolites or small-pore zeolites. The adsorption mechanism varies accordingly. In the first case, adsorption is driven by electrostatic interactions, while in the second, it is governed by diffusion and size exclusion [3].

The next chapter will analyze the previous mentioned technologies, starting with methanol transportation by ship to a coastal area where it will be used in either a DMFC or an MEC, followed by the capture and storage of the resulting CO_2 emissions.

2 STATE OF THE ART

2.1 Maritime transport of methanol

To transport the energy generated by renewable energy sources over thousands of kilometers, even across continents, the best option is to use a hydrogen carrier. This is

because hydrogen has a very low volumetric energy density compared to typical fossil fuels, for instance, it is 3.000 times lower than that of gasoline [13]. To be transported, hydrogen must either be compressed or liquefied, but these methods present challenges related to the tank weight and leakage, respectively [13]. For this reason, an alternative solution is to transport hydrogen in the form of Liquid Organic Hydrogen Carrier (LOHC), such as methanol, which is considered the most promising candidate for an international renewable energy supply chain [7].

Methanol is a simple alcohol that remains liquid at ambient temperature and pressure, making it easier to transport, store, and handle compared to hydrogen [14]. The most cost-effective method for transporting methanol is by ship rather than by trucks, pipelines, or railways [13]. Indeed, with minor modifications, existing crude oil cargo vessels can be adapted to transport methanol [9].

The concept behind an international renewable energy supply chain is to produce methanol using green hydrogen, generated in locations with abundant RES, and CO_2 captured from the atmosphere or derived from biomass or municipal solid waste feedstock [14,16]. Depending on the source of CO_2, the product is classified as e-methanol (from captured CO_2) or bio-methanol (from biomass) [15].

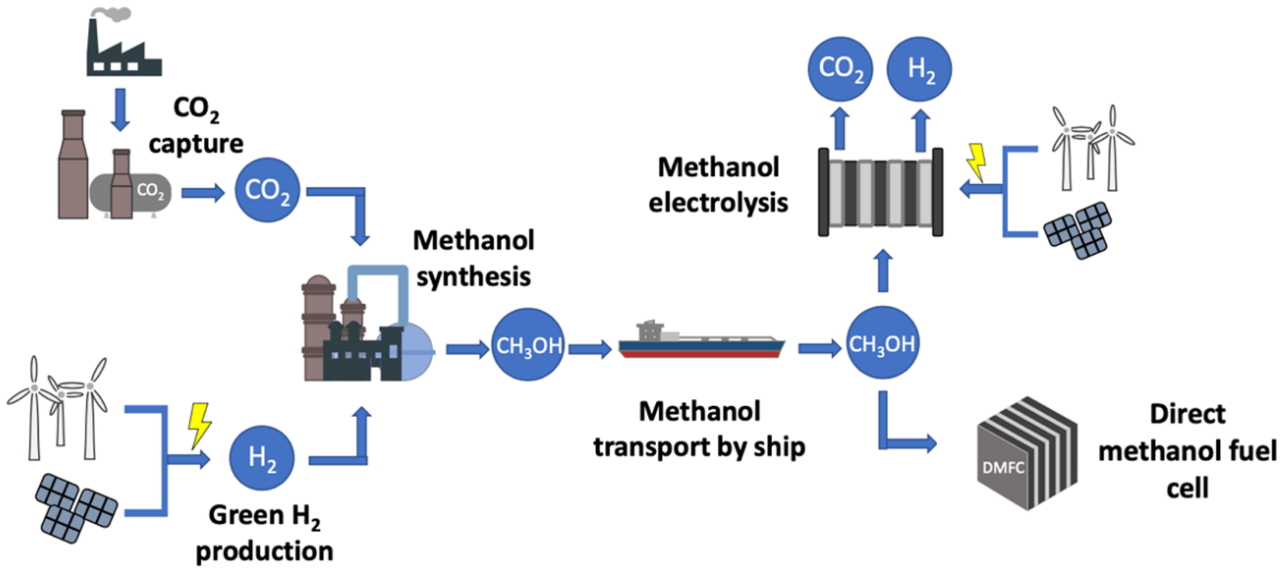

Figure 3. Diagram of use of methanol as energy vector and hydrogen carrier [42]

Since this study focuses on a coastal area, the hydrogen required for methanol synthesis can be produced via a water electrolyzer powered by RES. The water used can be desalinated seawater. It must be purified to meet the requirements of the electrolyzer. Desalination can be carried out using reverse osmosis, currently the most reliable membrane-based technique. This process operates on the principle that water molecules, subjected to a pressure gradient higher than the osmotic pressure, are forced

to move in the opposite direction to natural osmosis, passing through a membrane from a higher to a lower salt concentration solution [24].

The electrolyzer supplied with desalinated water can be of various types, including Proton Exchange Membrane Electrolyzer, Alkaline Water Electrolyzer (AWE) and Solid Oxide Electrolyzer Cell (SOEC).

Once methanol is synthesized in dedicated facilities powered by RES, it must be stored at the port for approximately three days to comply with port requirements before being shipped.

With a boiling point of 64,67°C, methanol is stored at ambient temperature [17]. This storage step is crucial at both the departure and arrival ports, and it is part of the packing and unpacking process. Packing refers to the entire process of methanol production, storage, and loading into the ship, while unpacking includes unloading methanol from the ship's tanks, storing it again, and all subsequent processes [15].

Regarding storage, its size depends on the capacity of the ship's tanks, the number of ships, the voyages, and the amount of methanol delivered [15]. Most ship tanks used for long distances have a volume between 120.000 and 160.000 m^3. The loading and unloading time depend on their size, and these operations are carried out using pipelines controlled by pumps [17].

2.2 Direct Methanol Fuel Cell

A fuel cell is an electrochemical generator capable of producing electricity and waste heat by converting the chemical energy of the input fuel through oxidation and reduction reactions occurring at the anode and cathode, respectively [18]. The proton exchange membrane fuel cell (PEMFC) is one of the most well-known and widely used fuel cells in the portable power and automotive sectors [18]. As the name suggests, its electrolyte membrane allows the transport of H^+ ions, which migrate toward the cathode. It is a low-temperature fuel cell, operating within a range of 60-80°C [18]. The fuel used is hydrogen, enabling clean energy production with zero emissions. However, hydrogen storage and its high flammability raise safety concerns [19,20].

The acid-based direct methanol fuel cell (DMFC) is essentially a PEMFC that uses liquid methanol (CH_3OH) as fuel. In addition to generating electricity and water as byproducts, it also emits CO_2 [21]. Like PEMFCs, DMFCs operate at low temperatures, typically between 60-120°C [18]. The interest in DMFCs spans multiple sectors, including military applications, transport, and telecommunications, due to their ability to be integrated into compact and portable devices requiring low power (small-scale applications). Nevertheless, they can also be utilized for larger-scale stationary power generation systems [18,20].

As mentioned in Section 2.1, methanol is easier to handle than hydrogen, has a high energy density, and is considered environmentally friendly [20]. However, it is toxic and flammable, for this reason, DMFCs must be designed to minimize the risk of methanol leakage [18].

DMFCs can be classified into three types: active, semi-passive, and passive, based on the method of fuel and oxidant supply. In active DMFCs, components such as pumps, fans, sensors, heaters, and humidity control systems regulate fuel and oxidant flow in a controlled and precise manner, enhancing fuel cell performance. This one is the DMFC that it is used in the experimental procedure. In contrast, passive DMFCs rely on capillary forces, gravity, and concentration gradients to transport fuel and oxidants without the need for additional components [22].

2.2.1 Working principle

Regarding the operating principle of an acid-based Direct Methanol Fuel Cell (DMFC), a methanol-water solution enters the anode, where methanol undergoes oxidation to produce carbon dioxide, protons and electrons. Simultaneously, oxygen is supplied to the cathode, where the reduction reaction occurs. As in the Proton Exchange Membrane Fuel Cells (PEMFCs), protons migrate from the anode to the cathode through the Nafion electrolyte membrane, which must remain hydrated to facilitate proton transport. This is because the proton conductivity of Nafion is inversely proportional to its water content [19]. Nafion consists of a hydrophobic Teflon backbone modified with a side chain terminating in a hydrophilic HSO_2 ionic site [23]. Meanwhile, electrons travel through the external circuit from the anode to the cathode, generating electricity [21].

The reactions involved are as follows:

anode side	$CH_3OH + H_2O \rightarrow CO_2 + 6H^+ + 6e^-$	(Eq. 1)
cathode side	$\frac{3}{2}O_2 + 6H^+ + 6e^- \rightarrow 3H_2O$	(Eq. 2)
overall reaction	$CH_3OH + \frac{3}{2}O_2 \rightarrow CO_2 + 2H_2O$	(Eq. 3)

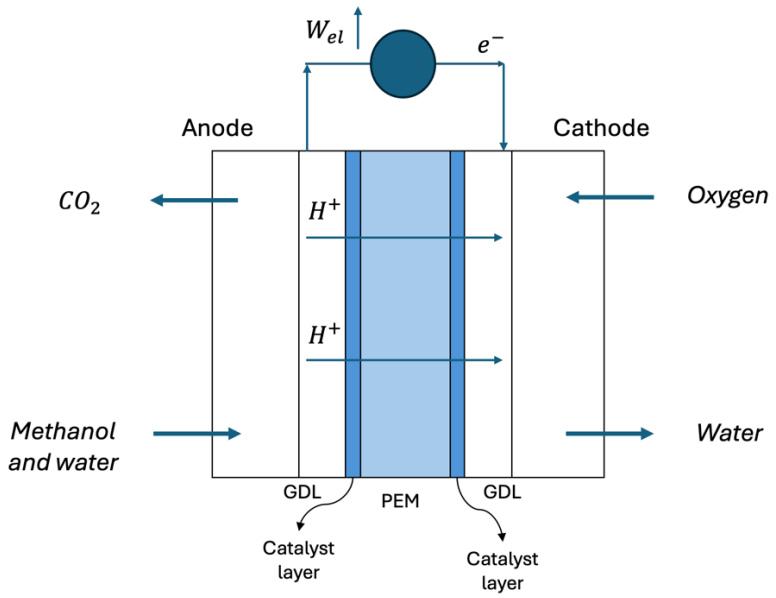

Figure 4. Schematic diagram Direct Methanol Fuel Cell (PowerPoint)

At the anode, intermediate species such as carbon monoxide, formaldehyde, and formic acid may form, which slow down the methanol oxidation reaction (MOR) kinetics [23].
All reaction products (liquid water at the cathode and gaseous CO_2 at the anode) must be efficiently and rapidly removed from the gas diffusion layer and flow channels to prevent performance degradation and ensure continuous fuel cell operation. If they are not properly removed, water flooding can occur at the cathode, while at the anode CO_2 molecules can block the pores, obstructing fuel passage and diffusion.
In both cases, surface oxides form, leading to reversible degradation of the fuel cell [22]. However, irreversible degradation occurs when material changes or alterations in the membrane electrode assembly (MEA) configuration take place. Examples include the deactivation of catalytic active sites, loss of proton conductivity, and oxidation of the catalyst support [22].

Regarding the performance of a DMFC, the theoretical open-circuit voltage is 1,21 V. However, the actual operating voltage is lower, typically around 0,6–0,7 V, due to losses associated with activation overvoltage, related to charge transfer at the electrode interface; ohmic overvoltage, associated with charge migration/conduction through the electrolyte, electrodes, and external circuit; concentration overvoltage, caused by mass transport limitations [18].

An essential factor influencing fuel cell efficiency and performance is temperature. The optimal operating range is between 50°C and 90°C. At lower temperatures, methanol viscosity increases, worsening mass transport and leading to higher concentration overvoltage. At higher temperatures, the risk of methanol crossover and membrane dehydration rises.

Methanol crossover is a major issue in DMFCs. It occurs when methanol permeates from the anode to the cathode, where it reacts with oxygen without generating electrical current. This reduces cell voltage and increases fuel consumption beyond theoretical expectations [23]. As previously mentioned, the membrane must remain hydrated to allow proton transport. However, this also enables methanol crossover from the anode to the cathode. To mitigate this issue, the membrane needs to be modified by developing new types of polymeric membranes [19].

Another critical parameter is methanol concentration in the water-methanol mixture supplied to the fuel cell. The methanol-to-water ratio should be greater than 1:1 to prevent partial methanol oxidation, which could poison the catalyst layer. Additionally, high methanol concentrations can lead to CO_2 crossover to the cathode, increasing mass transport resistance and making CO_2 removal more difficult. A CO_2 capture system can help address this issue [19].

2.2.2 Components

The core component of a Direct Methanol Fuel Cell (DMFC) is the membrane electrode assembly (MEA), which consists of the electrolyte and electrodes (anode and cathode) with their catalyst layer and gas diffusion layer (GDL), [19]. Each of these components is described below.

The electrodes are made of porous carbon fibers. Carbon-based materials are typically used due to their advantageous properties, including long life cycles, high electrical conductivity, and chemical stability [23].

A layer of catalytic material is deposited into the electrodes to facilitate the reactions. Platinum is the most used catalyst. However, it is expensive and requires stabilization with an inert support, such as a carbon black matrix. A significant drawback of using pure Pt at the anode is that the methanol oxidation reaction (MOR) does not proceed completely due to the formation of CO and other intermediate species, as mentioned in the previous section [23]. To address this issue, Pt alloys with transition metals have been developed, with ruthenium (Ru) showing the highest potential for MOR catalysis [19]. At the cathode, pure Pt remains the most effective catalyst, despite the sluggish kinetics of the oxygen reduction reaction (ORR) [23].

The electrolyte membrane must meet several essential requirements: it should exhibit high proton conductivity, low methanol permeability to prevent crossover, and stability under fuel cell operating conditions [19]. The most used electrolyte is Nafion, a perfluorosulfonic acid membrane. The interface where reactants, the catalyst, and the electrolyte come into contact is known as the three-phase interface. These interfaces are distributed within the three-dimensional network of the porous electrodes.

The gas diffusion layer (GDL) facilitates the transport of reactants to the active sites, namely the catalyst layer supported by the electrode. In catalyst-coated membrane (CCM) configurations, the GDL is applied after the catalytic layer on both sides [23]. This layer must possess hydrophobicity and good electrical conductivity. It is typically composed of a polytetrafluoroethylene (PTFE) suspension mixed with sugar or ammonium carbonate [19].

Another essential component completing the MEA is the gasket, which ensures a proper seal of the assembly [25].

Bipolar plates, also known as flow field plates, are one of the key components. They separate the reactant gases between adjacent cells, electrically connect the cells in series, and serve as a structural support. They feature flow channels on the external surface to ensure efficient reactant distribution across the electrode and facilitate product removal. The internal surface usually has a different flow field design to accommodate the cooling fluid channels, both in the of natural or forced cooling [25]. Bipolar plates are typically made of stainless steel or graphite, but for large-scale production, polymer composite bipolar plates are being developed due to their lower cost, reduced weight, and easier manufacturing process [19].

Finally, in the complete fuel cell stack assembly, terminal current collectors are required to gather the produced electrical current and close the circuit. Clamping plates or end plates, positioned at both ends of the stack, apply pressure to the cells, maintain structural integrity, prevent fuel and gas leaks, and allow for the inlet and outlet of the manifolds [25].

2.3 Methanol Electrolysis Cell

The most used method for hydrogen production is electrolysis, as it is the most convenient and fastest approach. However, the major drawback of water electrolysis is the high energy demand required for the process [26].

In recent years, research has shifted towards the electrolysis of a water-methanol solution, which can produce a highly pure hydrogen stream while operating at a significantly lower voltage [27]. In fact, while the theoretical voltage required for water electrolysis is 1,23 V, for the electrolysis of a water-methanol solution, it is only 0,03 V. This means that the electricity input needed is considerably lower [28].

The system under analysis is an electrolyzer with a polymer electrolyte membrane (PEM). The Methanol Electrolysis Cell (MEC) is a PEM electrolysis cell that operates with a methanol solution instead of water. Essentially, it is a DMFC operating in reverse. In this setup, hydrogen is produced, and electricity is supplied as an input using a DC power source, along with methanol as the fuel.

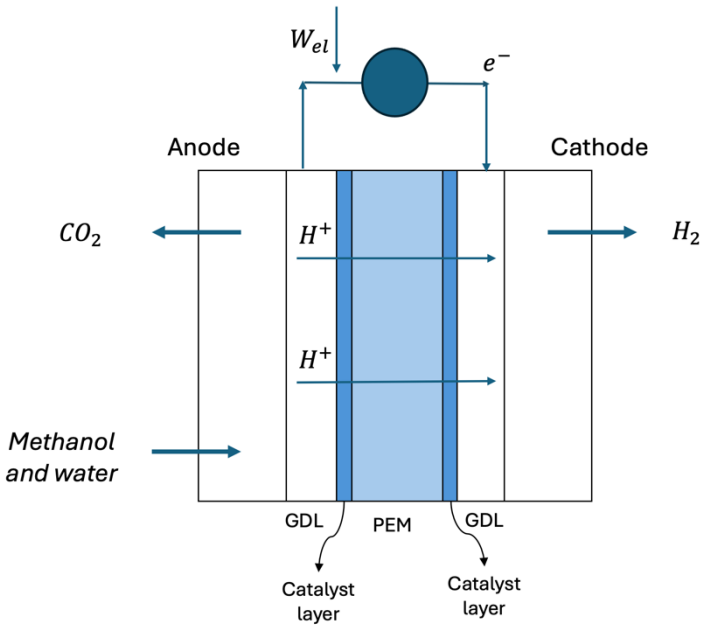

Figure 5. Schematic diagram Methanol Electrolysis Cell (PowerPoint)

The reactions occurring inside the electrolyzer are the following [28]:

anode side	$CH_3OH + H_2O \rightarrow CO_2 + 6H^+ + 6e^-$	(Eq. 4)
cathode side	$6H^+ + 6e^- \rightarrow 3H_2$	(Eq. 5)
overall reaction	$CH_3OH + H_2O \rightarrow CO_2 + 3H_2$	(Eq. 6)

As seen from the reactions, CO_2 is also produced in this process. However, due to its high concentration in the anode exhaust gas, it can be effectively captured [28].

The configuration is similar to that of the DMFC described in Section 2.2. It includes the MEA, which consists of the electrodes separated by a proton exchange membrane. The catalyst layers are positioned between the electrodes and the membrane. A titanium mesh or carbon cloth is used as a support for the MEA, ensuring uniform distribution of methanol and gas. Titanium or graphite distributor plates with flow channels facilitate reactant flow. The outer components are the end plates. [27].

The materials used for the various components are the same as those in a DMFC: Nafion for the proton-conducting polymer electrolyte membrane, Pt and PtRu for the catalyst layers at the cathode and anode, respectively, both supported by carbon [26].

2.4 CO_2 capture and storage

As highlighted in the previous paragraphs, using methanol to produce both electricity and hydrogen results in CO_2 emissions. The technologies considered for capturing this CO_2 are amines and zeolites.

2.4.1 Amines

To perform post-combustion carbon capture, which involves capturing CO_2 from a stream with a high concentration of CO_2 along with other components, the most used technology is chemisorption via amine-based solvents [11]. Capturing 0,5 kmol of CO_2 requires 1 kmol of amine [34].

The most well-known amine is monoethanolamine (MEA). However, the aqueous absorption-based process presents several challenges, including high regeneration costs and high amount of degraded solvent. The regeneration temperature ranges between 100 and 120°C [11].

The minimum work required for separation can be determined for any separation method. For a typical flue gas CO_2 concentration of 0,15, the minimum separation work is 107 kJ/kg, and it increases as the CO_2 concentration decreases. When accounting for the heat required, equivalent to mechanical work, the efficiency of amine-based separation methods drops to between 8% and 15% [34].

As explained in the introduction, an aqueous MEA solution is counter currently flowed against the CO_2-rich gas stream. The solution captures CO_2, which is then separated, allowing the solvent to be regenerated and reused in another cycle. At 40°C, CO_2 reacts with the amine to form carbamates. Breaking the strong bonds in carbamates requires a significant amount of energy, which must be supplied in the stripper.

Amines can be classified as primary, secondary, or tertiary, depending on the number of alkyl or aryl groups attached to the nitrogen atom. These amines differ in terms of the heat of absorption (also called enthalpy of absorption) required: for primary amines (such as MEA), it is -84 kJ/mol, for secondary amines (such as DEA) -67 kJ/mol, and for tertiary amines (such as MDEA) -55 kJ/mol.

Since absorption is an exothermic process, while desorption is endothermic, tertiary amines are less favorable for CO_2 absorption but require less heat for regeneration [30].

Other liquid mixtures being developed to address the aforementioned issues with MEA include diethanolamine (DEA) and N-methyldiethanolamine (MDEA), for example. Sterically hindered amines have also been studied for CO_2 capture. By introducing a bulky group adjacent to the amino nitrogen site, the stability of the carbamate is reduced, leading to lower regeneration costs and improved absorption rates [30].

Another possibility for using amines could be to use solid porous adsorbents with surfaces modified by amine compounds to enhance their affinity for CO_2 [29]. In this case mechanism is chemical adsorption and not anymore chemical absorption. In solid materials, CO_2 adsorption occurs at the solid-gas interface [11]. Amine-functionalized materials show great potential due to their high CO_2 capacity and relatively low

regeneration temperatures. The most used amine for functionalizing solid materials is TEPA (tetraethylenepentamine), which contains five amine groups and is thus theoretically capable of absorbing up to five CO_2 molecules per TEPA molecule. Recently, research has also explored amine-containing polymers, particularly branched polyethylenimine (BPEI), due to its low cost, market availability, CO_2 absorption capacity similar to or slightly lower than TEPA, and low regeneration temperature [11].

2.4.2 Zeolites

Zeolites are aluminosilicates composed of tetrahedral SiO4 or AlO4 units interconnected by oxygen bridges. They have a three-dimensional structure with uniform molecular-sized pores [31]. Zeolites can adsorb molecules that fit into their pores while excluding larger ones. Commercially used zeolites are synthetic rather than natural, as natural zeolites may contain impurities or contaminants [31].

Zeolites belong to the category of solid adsorbents used for CO_2 capture, alongside carbon-based materials such as activated carbon, carbon nanotubes, and graphene, as well as mesoporous silica and metal-organic frameworks (MOFs) [31].

In general, CO_2 adsorption mechanisms include interaction between one of the oxygen atoms in CO_2 and the extra-framework cation of the zeolite, and a bridging mechanism where both oxygen atoms of CO_2 interact with the extra-framework cation of the zeolite [3].

Physical adsorption, associated with Van der Waals forces, is favored at low temperatures and high pressures. Furthermore, modifying the adsorbent can enhance CO_2 adsorption capacity, selectivity, and moisture tolerance [31]. In physisorption, the enthalpy of adsorption ranges between -25 and -50 kJ/mol, which is lower than the enthalpy for chemisorption, such as in amine-based solutions [3]. However, zeolites generally have an energetically heterogeneous surface, except for all-silica zeolites. The cationic sites exhibit higher adsorption enthalpy, ranging from -30 to -90 kJ/mol, and have the strongest interaction with CO_2. Once these cationic sites become saturated with CO_2, the adsorption enthalpy decreases [3].

Zeolites offer good structural stability and can be produced at a low cost with simplicity [3]. However, in gas mixtures containing water, the adsorption sites may be occupied by both CO_2 and H_2O. This issue is particularly relevant for low Si/Al ratio zeolites due to their strong affinity for water. Conversely, high Si/Al ratio zeolites are less affected by water presence, making them more suitable for wet streams in decarbonization processes. Another challenge is the regeneration energy required for zeolites, which is higher than that for carbon-based materials [3].

Various types of zeolites exist, but the most used for carbon capture and storage (CCS) are A (also called LTA or NaA), X, and Y [31]. These are characterized by different numbers

of member rings: A has 8-member rings, while X and Y have 12-member rings. Another classification is based on the Si/Al ratio: A and X have a low ratio (between 1 and 1,5), while Y has an intermediate ratio (between 2 and 5). Both physical and chemical adsorption mechanisms contribute to CO_2 capture in zeolite A. The Si/Al ratio in zeolite A plays a fundamental role in CO_2 capture, enabling chemical adsorption through bicarbonate or carbonate formation [31]. Additionally, pore size influences adsorption: CO_2 can easily enter zeolite A pores due to their diameter (0,4 nm) compared to the kinetic diameter of CO_2 (0,33 nm) [31].

Due to their higher affinity for CO_2, NaA zeolites are often used in post-combustion carbon capture, compared to NaX and NaY zeolites. Other factors influencing CO_2 adsorption capacity include temperature and pressure: adsorption capacity increases with higher CO_2 partial pressure and decreases with rising temperature. At high pressures, the pore volume of zeolites controls the adsorption mechanism, whereas at low pressures, the cationic density of zeolites directly correlates with the amount of CO_2 adsorbed [31]. Finally, zeolite basicity and electric field also influence performance. These depend on the nature of the counter-cations, also known as exchangeable cations, present in the zeolite framework cavities. By increasing the zeolite's basicity through the selection of suitable cations, CO_2 capture capacity can be enhanced.

To improve adsorption performance at higher temperatures, zeolites A, X, and Y can be modified with amines, thereby increasing their basicity. For zeolite A, the best results are obtained with iso-butylamine modification, while for zeolite 13X, monoethanolamine (MEA) modification is most effective [31]. Another approach to enhancing CO_2 adsorption capacity involves altering zeolite pore size, transitioning from micropores to mesopores [31].

Regarding the industrial application of zeolites for carbon capture, the most promising method is Pressure Swing Adsorption (PSA). This process utilizes two column reactors where different cycle steps occur: pressurization of a CO_2-lean stream in the adsorption bed, CO_2 adsorption as the CO_2-containing stream passes through the adsorption bed, and, once saturation is reached, a blow-down step in which depressurization releases CO_2, forming a CO_2-rich stream. Residual CO_2 can be further removed through purging with another stream. For this application, zeolites are not used in powder form but rather as pellets or other macroscopically shaped structures. Pellets with high pore volume improve mass transfer and reduce cycle time but at the expense of volumetric efficiency [3].

In the following *Table 1*, the summary of the advantages and disadvantages of the technologies just analyzed are presented.

	Absorption	Adsorption	
	Chemical (e.g. MEA solution)	**Chemical (e.g. amine based adsorbents)**	**Physical (e.g. zeolites)**
Pros	High absorption efficiency for concentrated CO2 gas stream (> 90% vol. CO2)	High adsorption efficiency (>85% vol.CO2)	
	High capacity at low T and high p		Reversible physical adsorption process
	Low -cost solvent	Adsorbent can be recycled (low waste generation)	
	Most mature technology	High capacity at low CO2 pressure	High capacity with low T and high p
		Less corrosion	
Cons	Energy-intensive solvent regeneration	Degradation by heat, oxidation and contaminats	Low CO2 selectivity
	Corrosive solvents and degradation by contaminants		
	High operating cost	High energy consumption for the high T of adsorption and regeneration	Decreasing capacity with T and presence of moisture
	Low capacity at high T and low p		

Table 1. Advantages and disadvantages of absorption and adsorption methods (Excel) [35]

3 METHODOLOGY FOR TECHNO-ECONOMIC ANALYSIS

This chapter will present the considerations made and the calculations to be performed for the techno-economic analysis of methanol transport and usage. All data and equations reported refer to reference [32], except for the paragraph about DMFC plant and CCS.

3.1 Desalination treatment plant

To evaluate the cost of a methanol synthesis plant, it is essential to consider the cost of hydrogen and CO_2 required for its production. For hydrogen, the cost of the water electrolysis plant used to produce it must be considered.

As mentioned in Section 2.1, in a coastal area, seawater can first be treated and desalinated to make it suitable for use in a PEM electrolyzer for hydrogen production.

For this reason, the study begins by analyzing the cost of the seawater desalination system. The key components of such a system include: two seawater pumps (one low-pressure and one high-pressure), filters, a chemical treatment system, valves, reverse osmosis (RO) cartridges, a Pelton turbine, and a mixing chamber.

For each of these components, the following costs must be assessed: purchase cost, annual energy consumption (for the two pumps), O&M costs, annual chemical treatment costs, the cost for two replacements for the pumps and turbine over the plant's lifetime (assumed to be 30 years) and for the annual replacement of the RO membrane.

Going into detail, the purchased equipment cost of the SWIP that corresponds to the seawater intake and pre-treatment section, is analyzed. This section includes the low-pressure pump, filter, and chemical treatment system. The following formulation allows for its calculation while accounting for annual inflation:

$$PC_{SWIP} = 1184 \cdot \dot{V}_t^{4/5} \quad \text{(Eq.7)}$$

Where $\dot{V}_t$ is the volumetric flow rate of seawater feeding the plant, expressed in m³/day.

For the purchased cost of the high-pressure pump, the following formulation is used:

$$\log_{10}\left(\frac{PC_{HPP}}{1.189}\right) = 3{,}3892 + 0{,}0536\log_{10}\left(p_{HPP}\cdot\dot{V}_{RO}\cdot\frac{f_1}{\eta_{HPP}}\right) + 0{,}1538[\log_{10}\left(p_{HPP}\cdot\dot{V}_{RO}\cdot\frac{f_1}{\eta_{HPP}}\right)]^2 \quad \text{(Eq.8)}$$

The terms of the equation are defined as follows:

- p_{HPP} is the pump pressure in kPa;
- $\dot{V}_{RO}$ is the volumetric flow rate of water to the pump, in m³/s;
- η_{HPP} is the pump efficiency;
- f_1 is the plant load factor.

For both pumps, it is possible to calculate the annual cost of energy consumption. In this case, the formula for the low-pressure pump is provided below:

$$\dot{c}_{e,SWIP} = p_{SWIP}\cdot\dot{V}_t\cdot f_1\cdot\frac{C_e}{\eta_{SWIP}} \quad \text{(Eq.9)}$$

Clearly, for the high-pressure pump, it is sufficient to replace pressure and efficiency with p_{HPP} and η_{HPP}. In this case, the volumetric flow rate of seawater is expressed in m³/s. C_e represents the electricity price in $/kW·year.

The cost of the membrane is calculated using the following expression:

$$PC_{RO} = 10\cdot N\cdot A \quad \text{(Eq.10)}$$

Where N is the number of membranes installed and A is the area of each membrane.

As for the Pelton turbine, its cost is also adjusted to account for inflation:

$$\log_{10}\left(\frac{PC_{PT}}{1.189}\right) = 2{,}2476 + 1{,}4965\log_{10}(p_{PT}\cdot\dot{V}_{brine}\cdot f_1\cdot\eta_{PT}) + 0{,}1618[\log_{10}(p_{PT}\cdot\dot{V}_{brine}\cdot f_1\cdot\eta_{PT})]^2 \quad \text{(Eq.11)}$$

Where p_{PT} is the pressure before the turbine (kPa), $\dot{V}_{brine}$ is the volumetric flow rate through the turbine (m³/s), and η_{PT} is the turbine efficiency.

It is important to highlight that, for this analysis, the total capital investment (TCI) is assumed to be 6,32 times the equipment purchase cost.

The cost of chemical treatments is defined using the following expression:

$$\dot{c}_{op,ch} = \dot{V}_t\cdot \mathrm{f_1}\cdot \mathrm{C_{ch}} \quad \text{(Eq.12)}$$

Here, the total volumetric flow rate of seawater is expressed in m³/year and C_{ch} represents the cost of chemical treatment per unit volume of water.

As previously mentioned, the RO cartridges must be replaced annually, and the cost of this replacement is calculated as follows:

$$\dot{c}_{op,RO} = r_m \cdot cc_{RO} \cdot \dot{V}_{RO} \quad \text{(Eq.13)}$$

r_m is the membrane replacement factor, cc_{RO} is the cost of a cartridge filter, and $\dot{V}_{RO}$ is the volumetric flow rate of water to the pump, in this case expressed in m³/year.

Parameter	Value	Uncertainty
η_{HPP}	90%	5%
η_{SWIP}	87%	5%
η_{PT}	79%	5%
f_1	0,9	5%
r_m	0,1	10%
C_ch ($/m^3)	0,018	5%
p_{SWIP} (kPA)	650	5%
p_{HPP} (kPA)	5350	5%
p_{PT} (kPA)	5100	5%
cc_RO ($/m^3)	0,01	5%
End of Life (%TCI)	10%	5%
O&M low pressure pump (%TCI)	5%	-
O&M high pressure pump (%TCI)	4%	-
O&M RO (%TCI)	1%	-
O&M turbine (%TCI)	4%	-

Table 2. Assumptions for the desalination treatment plant (Excel) [32]

3.2 Water Electrolysis plant

Once this assessment is complete, the cost of the water electrolysis plant must be evaluated.

To estimate the cost of the PEM electrolyzer, the following empirical formula is used as a function of the nominal hydrogen mass flow rate in kg/s:

$$C_{EC} = 90588585 \cdot \frac{\dot{m}_{H_2}^{0.79}}{j^{0.32}} \quad \text{(Eq.14)}$$

Where j is the current density (A/cm²).

Regarding O&M costs, these are 1,5% of the CAPEX. Additionally, given the lifespan of an electrolyzer, two complete midlife refurbishments are expected.

Next, the electrical consumption of the PEM electrolyzer will be analyzed, as it is used in the calculation of the levelized cost of hydrogen:

$$\dot{W}_{ext,electrol} = \frac{\dot{m}_{H_2} h_{H_2} + \dot{m}_{O_2} h_{O_2} - \dot{m}_{H_2O} h_{H_2O}}{\eta_{electrol}} \quad \text{(Eq.15)}$$

The flow rates are calculated as $\dot{m}_{H_2} = \frac{M_{H_2}}{M_{H_2O}} \cdot \dot{m}_{H_2O}$ and $\dot{m}_{O_2} = \frac{M_{O_2}}{M_{H_2O}} \cdot \frac{\dot{m}_{H_2O}}{2}$.

The enthalpies have been determined using the generic formula for the element *i*:

$$h_i = \Delta h_{f,i}^0 + [h_i(T,p) - h_i(T^0,p^0)] \quad \text{(Eq. 16)}$$

The efficiency of the electrolyzer is less than one, as part of the supplied energy is lost as heat. To evaluate this loss, *Eq. 17* can be used:

$$\left(\frac{dE}{dt}\right)_{lost} = \dot{W}_{ext,electrol} - \dot{m}_{H_2} HHV_{H_2} \quad \text{(Eq.17)}$$

Parameter	Value	Uncertainty
j (A/cm^2)	1	5%
electrolyzer efficiency	0,8	5%
Yearly O&M (%C_electrol)	1,50%	5%
M-L refurbishment (%C_electrol)	200%	5%
End of Life (%C_electrol)	10%	5%
T0 (°C)	25	1%
T_O2 (°C)	80	1%
T_H2 (°C)	80	1%
T_H2O (°C)	25	1%
p0 (kPa)	100	1%
p_O2 (kPa)	5000 (pipeline) 3000 (LH2 & cH2)	1%
p_H2 (kPa)	5000 (pipeline) 3000 (LH2 & cH2)	1%
p_H2O (kPa)	5000 (pipeline) 3000 (LH2 & cH2)	1%
$\Delta h^0_{f,H2}\left(\frac{kJ}{mol}\right)$	0	0%
$\Delta h^0_{f,O2}\left(\frac{kJ}{mol}\right)$	0	0%
$\Delta h^0_{f,H2O}\left(\frac{kJ}{mol}\right)$	-285,83	0%
HHV_H2 (MJ/kg)	141,88	0%

Table 3. Assumptions for the water electrolysis plant (Excel) [32]

3.3 Methanol synthesis plant

The cost of the methanol synthesis plant depends on both the methanol production rate $\dot{m}_{meOH}$ (kg/s) and the cost of the electrolysis plant C_{EC} :

$$C_{synth} = 57348390 \cdot \dot{m}_{meOH}^{0.9086808} - 3C_{EC} \quad \text{(Eq.18)}$$

Regarding O&M costs, fixed OPEX is expressed as a percentage of the initial investment. Additionally, the cost of CO_2 and the electricity consumed must be accounted for.

Parameter	Value	Uncertainty
H2 usage (kgH2/kgMeOH)	0,192	5%
CO2 usage (kgCO2/kgMeOH)	1,397	5%
Energy consumption on mass flow of methanol produced (MWh/t)	0,175	-
CO2 cost ($/kg)	0,0229	5%
M-L refurbishment (%C_synth)	200%	5%
Yearly Fixed O&M (%C_synth)	1,50%	5%
End of Life (%C_synth)	10%	5%

Table 4. Assumptions for a methanol synthesis plant (Excel) [32]

3.4 Methanol storage facility

To calculate the methanol storage cost, an equation is used as a function of the facility's maximum storage capacity m_{MeOH} in kg.

$$C_{S\mathrm{MeOH}} = 53{,}1 \cdot m_{\mathrm{MeOH}} \qquad \text{(Eq.19)}$$

This cost formulation does not account for scale effects, since it is based on the price of relatively small storage tanks (200 tons tanks) and its linear extrapolation to large-scale facilities may therefore overestimate the total investment cost.
It should be noted that the net volume of methanol stored at the sending terminal corresponds to the volume that can be transported by the cargo vessels; at the receiving terminal, instead, the net stored volume refers to the amount remaining on board the vessels that is not consumed by them.

Parameter	Value	Uncertainty
M-L refurbishment (%C_sMeOH)	100%	5%
End of Life (%C_sMeOH)	5%	5%

Table 5. Assumptions for methanol storage facilities (Excel) [32]

3.5 Methanol carrier ship

For the transportation of methanol by ship, the techno-economic model of liquefied hydrogen (LH_2) transport by sea can be used as a reference. The key difference lies in the characteristics of the vessels employed, which directly impact the assumptions and input data used for calculations. Additionally, there is no specific economic data available for methanol carriers, meaning that existing data from tanker ships, which share some similarities, must be used as a starting point to make the necessary assumptions.

Referring to LH_2 transport ships, vessels can be chartered under three types of agreements: bareboat charter, time charter, and voyage charter. Among these, the time

charter will be considered the most cost-effective option. Under this model, the shipowner is only responsible for fixed costs, which include CAPEX and fixed operational expenses, while voyage costs are excluded. Voyage costs are further categorized into proportional costs and non-proportional costs. Proportional costs refer to consumption-related expenses incurred during the voyage, while non-proportional costs include port fees, marine pilot services, and tug services, which depend on both the port of operation and the ship's characteristics.

A time charter is the most advantageous contract for companies that are not specialized in shipping, as these cargo vessels operate between fixed points. Opting for a voyage charter would be too expensive in this context. The charter cost itself depends on several factors, including charter duration, vessel size, and the age of the ship. Regarding charter duration, there are two main types of contracts: spot charter, which is valid for six months or less, and long-term charter, which applies for more than five years.

Finally, similar to hydrogen carriers, methanol-fueled ships also consume part of their cargo as fuel. The methanol used onboard is considered a cost associated with lost energy, meaning that proportional voyage costs do not apply in this case.

The equations to be used are provided below. The first one is used to estimate the duration of a roundtrip:

$$t_{RT} = 2 \cdot \frac{l}{s_V} + t_{LS} + \frac{V_{MeOH}}{\dot{V}_L} + \frac{m_{OL}}{\rho_{met}(1\ bar) \cdot \dot{V}_{OL}} \quad \text{(Eq.20)}$$

Where:

- l is the length of the route;
- s_V is the speed at which the ship is traveling;
- t_{LS} is the additional time required for departure and approach to the arrival port, during which the ship's speed is lower than its cruising speed;
- V_{MeOH} is the volume capacity of the ship;
- $\dot{V}_L$ is the mass flow rate loaded onto the ship. By dividing these two terms, the loading time of the ship is obtained;
- m_{OL} is the mass of methanol off-loaded from the ship at the arrival port;
- $\rho_{met}(1\ \text{bar})$ is the saturation density of methanol at 1 bar;
- $\dot{V}_{OL}$ is the mass flow rate off-loaded at the arrival port.

To calculate the mass of methanol unloaded:

$$m_{OL} = m_L - m_C \quad \text{(Eq.21)}$$

m_L represents the mass of methanol loaded into the ship (which coincides with the total capacity of the tanks), while m_C is the methanol consumed by the ship as fuel during the roundtrip.

The latter is calculated as follows:

$$m_C = 2 \cdot \frac{l}{s_V} \cdot cr_C + \left(\frac{V_{MeOH}}{\dot{V}_L} + \frac{m_{OL}}{\rho_{met}(1\ bar) \cdot \dot{V}_{OL}}\right) cr_{L;OL} \quad \text{(Eq. 22)}$$

cr_C refers to the methanol consumption rate for navigation, while $cr_{L;OL}$ refers to the consumption rate during the loading and off-loading phases.

Another important value to calculate is the number of ships required:

$$N_{ships} = \frac{t_{RT}}{m_L} \dot{m}_{MeOH} \quad \text{(Eq.23)}$$

$\dot{m}_{MeOH}$ represents the methanol mass flow rate produced.

If a whole number of ships is not obtained, the navigation speed of the ships, s_V, is progressively reduced. This will, in turn, decrease the methanol consumption rate cr_C according to the following formulation:

$$cr_C = \left(\frac{s_V}{s_{V,nom}}\right)^3 \frac{\dot{W}_{nom}}{LHV \cdot \eta_{FC}} \quad \text{(Eq.24)}$$

where:

- $s_{V,nom}$ is the nominal navigation speed;
- $\dot{W}_{nom}$ is the power developed at the nominal cruising speed;
- *LHV* is the lower heating value of methanol;
- η_{FC} is the efficiency of the fuel cell used as the ship's engine.

At this point, it is possible to estimate the operational lifetime $N_{voyages}$:

$$N_{voyages} = \frac{t_L}{t_{RT}} \quad \text{(Eq.25)}$$

with t_L representing the lifetime cycle.

For a fleet, the life cycle cost C_{fleet} can be calculated as:

$$C_{fleet} = N_{ships} \cdot (t_{RT} \cdot c_{TC} + C_V) \quad \text{(Eq.26)}$$

c_{TC} represents the time charter rate, while C_V represents the voyage costs for a roundtrip.

Parameter	Value	Uncertainty
c_TC (kUSD/d)	19	10%
Cv (kUSD/round trip-land terminal)	15	10%
Ship capacity (t_MeOH)	95040	5%
V_MeOH (m^3)	120000	5%
Nominal pressure (bar)	1	-
Min pressure (bar)	1	-
s_vel_nom (kn)	15,4	5%
s_vel_nom (m/s)	7,92	5%
W_nom (sailing) (MW)	15	5%
W_nom (Loading and offloading) (MW)	2	5%
Power plant efficiency (based on LHV_MeOH)	0,35	5%
t_LS (s)	3600	5%
Volumetric flow L (m^3/h)	12000	5%
Volumetric flow OL (m^3/h)	12000	5%

Table 6. Assumptions for a methanol fleet (Excel) [32]

3.6 Direct methanol fuel cell plant

In this study, a plant with modules with nominal power output of 3 kW will be considered. Due to the lack of commercial-scale power plants of this kind, at first, the analysis will be carried out using data from the best-performing fuel cell prototype assembled in the laboratory. Cost-related data will be integrated with findings from scientific literature. A model will be developed to estimate the levelized cost of the produced energy.

Regarding the cost analysis of a direct methanol fuel cell (DMFC), the reference model will be the fuel cell stack developed under the DURAMET Project, a European initiative aimed at developing cost-effective components for DMFCs in small-scale production. The selected stack consists of 10 cells, with a nominal power output of approximately 200 W and an active area of 100 cm^2 [25].

The total cost of a DMFC stack includes the membrane, noble metals for the catalyst, electrodes, current collectors, gasket components, bipolar plates, clamping plates, and the assembly process. Additionally, labour costs and energy costs must be considered [25].

The small-scale production costs for the DURAMET stack (200 units per year) are summarized in the table below, considering labour costs, energy consumption, and investment costs.

	Component	Cost (€)
MEA	Anade	251
	Cathode	169
	GDL layer	160
	Membrane	71
Stack parts	Bipolar plates	680
	Clamping plates	413
	Current collectors	640
Manufacturing MEA and bipolar plates		400
Stack gasketing and stack hardware		100

Table 7. Costs estimation of the DURAMET stack prototype in a small-scale production (excel) [25]

The materials used in the DURAMET prototype are as follows:

- Anode catalyst: 50% Pt-Ru (1:1) /C
- Cathode catalyst: 30% Pt/C
- Membrane: FUMATECH F1850, 50-micrometer thickness
- Bipolar plates: Composite graphite
- Clamping plates: Anodized aluminum
- Current collectors: Gold-plated copper
- Polymeric gaskets
- Bolts, nuts, washers, and fittings (hardware components)

The total cost amounts to 2.884 €.

For small-scale production, such as laboratory prototypes, the MEA assembly process is typically handmade. However, for large-scale production, an automated process is required. Large-scale production refers to an annual output of 10.000 units, which is not particularly high considering the advanced technology and the specialized applications of these fuel cells.

According to the study conducted by Mauro Francesco Sgroi et al. [25], the cost of raw materials for a single stack produced at an industrial scale would amount to 223 €/unit.

	Component	Cost (€)
MEA	Catalysts	127
	GDL layer	17
	Membrane	27
Stack parts	Bipolar plates	3
	Clamping plates	8
	Current collectors	14
	Conductive gasket	2
	Insulation plates	3
	Nonconductive gaskets	7
	Hardware components	15
Total		223

Table 8. Costs of raw material for the components of a single unit in a large-scale production (Excel) [25]

In addition to raw material costs, investment in production machinery for mass manufacturing amounts to 511.000 €, while maintenance costs are estimated at 613.000 € (*Table 9*).

Machinary	Units	Unit/Price (€)	Investment (€)	Maintenance
Spray coater	1	35000	35000	10%
Die cutter	1	75000	75000	10%
Laminator press	3	92000	276000	2 years
Press assembling	1	40000	40000	2 years
Stack testing	1	85000	85000	102.200 €
Total	-	-	511.000 €	613.200 €

Table 9. Investment in machinery for stack production (Excel) [25]

The labour cost is estimated at 29 €/stack, while the electricity cost is 1 €/stack [25].

By adding these two costs to the raw material cost (223 €) from *Table 8*, the production cost of the plates by casting and modulating (72€), and the maintenance cost for the machinery (6€, calculated as 10% per year), it is possible to estimate the stack cost at 1.650 €/kW. The replacement of machinery is not considered, as a lifetime of 14 years is assumed for these components.

The stack considered operates with 5 M methanol, at an operating temperature of 100°C and an absolute pressure of 2 bar. However, if we consider a DMFC operating under the same conditions as the laboratory-tested system, namely 1 M methanol, 60°C, and 1 bar, the stack cost increases to 1.666 €/kW.

By adding the balance of plant to the stack cost per kW, the total reaches 4.000 €/kW.

At this point, it is essential to evaluate key parameters to characterize the analyzed DMFC, including efficiency, fuel utilization, and mass flow rates at the inlet and outlet.

We begin by defining the voltage efficiency of the DMFC, which, as with all fuel cells, is given by:

$$\eta_V = \frac{E_{cell}}{E_{rev}} \quad \text{(Eq.27)}$$

where E_{cell} is the voltage at the terminals, given by E_{cathode}- E_{anode} , while E_{rev} is the reversible potential for the process during cell operation under constant temperature and pressure. It is therefore the theoretical voltage of the cell.

Additionally, the fuel efficiency must be defined, as not all the supplied methanol reacts to generate electricity; part of it remains unconverted. This efficiency is given by the ratio of the measured electrical current to the current calculated using Faraday's law [23]:

$$\eta_f = \frac{I_{measured}}{I_{Faraday}} \quad \text{(Eq.28).}$$

Now, it is possible to calculate the overall chemical-to-electrical efficiency of the cell as:

$$\eta = \eta_V \cdot \eta_{rev} \cdot \eta_f \quad \text{(Eq.29)}$$

η_{rev} is the term that accounts for the irreversible entropy losses and is calculated as:

$$\eta_{rev} = \frac{\Delta G}{\Delta H} \quad \text{(Eq.30)}$$

Where ΔG and ΔH are the Gibbs free energy and the enthalpy of the entire reaction [23]. With this formulation, we are comparing the electrical energy produced by the cell (ΔG) with the heat that would be produced if the fuel were burned (ΔH). It is possible to consider the combustion enthalpy as coincident with the formation enthalpy shown in *Eq. 32* [19].

Recalling the complete reaction that occurs within the DMFC:

$$CH_3OH + \frac{3}{2}O_2 \rightarrow CO_2 + 2H_2O$$

It is possible to apply the following formulas to find the molar formation enthalpy (*Eq. 32*) and the molar formation entropy (*Eq. 33*), which can be used to calculate the molar Gibbs free energy of formation (*Eq. 31*) [19]:

$$\Delta g_f = \Delta h_f - \mathrm{T}\Delta \mathrm{s} \quad \text{(Eq.31)}$$

$$\Delta h_f = 2h_{\mathrm{f},H_2\mathrm{O}} + h_{\mathrm{f},CO_2} - h_{\mathrm{f},C\mathrm{H_3OH}} - \frac{3}{2}h_{\mathrm{f},O_2} \quad \text{(Eq.32)}$$

$$\Delta s_f = 2\mathrm{s}_{\mathrm{f},H_2\mathrm{O}} + \mathrm{s}_{\mathrm{f},CO_2} - \mathrm{s}_{\mathrm{f},C\mathrm{H_3OH}} - \frac{3}{2}\mathrm{s}_{\mathrm{f},O_2} \quad \text{(Eq.33)}$$

The typical value for the overall efficiency of a current DMFC is between 40-60% [18].

Other key parameters to consider when characterizing a DMFC are the mass flow rates of reactants and products at the inlet and outlet. To do this, it is first necessary to know the output voltage of the DMFC (this is referred to as E_{cell} in *Eq. 27*). It is important to note that when referring to the actual operating voltage of the cell, V_c, it is given by:

$$V_c = E_{Nernst} - E_{activation} - E_{ohmic} - E_{concentration} \quad \text{(Eq. 34)}$$

Where E_{Nernst} is the reversible open-circuit voltage, and the other terms represent the overvoltages due to activation losses, ohmic losses, and concentration losses, respectively.
Knowing this value, the power output is calculated as:

$$W_e = V_c \cdot n_c \cdot I \quad \text{(Eq.35)}$$

Where *I* is the measured current and n_c is the number of cells in series.

Now, the various mass flow rates can be calculated in kg/s:

$$\dot{m}_{O_2,c} = \frac{MM_{O_2} \cdot I \cdot n_c}{zF} \quad \text{(Eq.36)}$$

For the calculation of the mass flow rate of oxygen consumed by the fuel cell: Where MM_{O_2} is the molar mass, equal to 0,032 kg/mol; *z* is equal to 4 and it is the number of electrons per mole of fuel; *F* is the Faraday constant, which is 96.485 C/mol.

With the same formulation, it is possible to calculate the stoichiometric air consumption rate, using the molar mass of air, equal to 0,02897 kg/mol. By then multiplying it by the λ_{air} stoichiometric ratio (also called air utilization), the actual mass flow rate of the supplied air can be determined:

$$\dot{m}_{air,s} = \dot{m}_{air,c} \cdot \lambda_{air} \quad \text{(Eq.37)}$$

Now, the air flow exiting the fuel cell can be calculated as:

$$\dot{m}_{air,e} = \dot{m}_{air,s} - \dot{m}_{O_2,c} \quad \text{(Eq.38)}$$

In the same way, the stoichiometric mass flow rate of methanol can be calculated as:

$$\dot{m}_{CH_3OH,c} = \frac{MM_{CH_3OH} \cdot I \cdot n_c}{z \cdot F} \quad \text{(Eq.39)}$$

Now, the molar mass is 0,03204 kg/mol and *z* is 6. To calculate the mass flow rate of the supplied methanol, simply add the fuel utilization to the denominator.

As for the water produced at the cathode, we have:

$$\dot{m}_{H_2O,p} = \frac{MM_{H_2O} \cdot I \cdot n_c}{z \cdot F} \quad \text{(Eq. 40)}$$

The molar mass is 0,01802 kg/mol and *z* is 2 [19].

3.7 Methanol electrolysis plat

In this case as well, there is no specific data available for the technology under study. Therefore, the analysis is based on a well-known reference technology: the PEM electrolyzer. However, it is essential to consider the differences between the two technologies, which are listed below.

The first key difference concerns the catalytic layer. In the case of MEC, it contains platinum and ruthenium in concentrations of 1,5–2,0 mg/cm², whereas in PEM electrolyzers, the catalytic layer consists of 0,8 mg/cm² of platinum and 2,5 mg/cm² of iridium. This difference also affects the cost: the catalytic membrane of a PEM electrolyzer costs 8,29 × 10^{-2} USD/cm², while for MEC, it costs 2,60 × 10^{-2} USD/cm².

Another significant difference lies in the polarization curve, which influences the stack size. MECs operate at lower current densities and have lower efficiencies compared to PEM electrolyzers. As a result, to achieve the same hydrogen production rate, a larger and consequently more expensive stack is required. Specifically, an MEC can operate at a current density of 150 mA/cm² while maintaining a 45% efficiency, significantly lower than the 1 A/cm² typical of PEM electrolyzers at 0,5 V.

As previously mentioned, given the same hydrogen production rate and the specified current density, this leads to an increase in the system size by a factor of 1,3–1,4. Based on these considerations, the cost of this electrolyzer can now be calculated:

$$C_{EC} = (663894313 + 131158196) \cdot \frac{\dot{m}_{H_2}^{0,79}}{j^{0,32}} \quad \text{(Eq.41)}$$

Where *j* represents the current density, expressed in A/cm², and $\dot{m}_{H_2}$ is the mass flow rate of hydrogen, measured in kg/s.

As for the yearly O&M costs, they are estimated at 0,20% of the eletrolyzer cost, corresponding to the CAPEX. Additionally, at least two complete midlife refurbishments could be expected.

The formula for calculating electricity consumption is the following:

$$\dot{W}_{ext,meth-electrol} = \frac{\dot{m}_{H_2} h_{H_2} + \dot{m}_{CO_2} h_{CO_2} - \dot{m}_{H_2O} h_{H_2O} - \dot{m}_{CH_3OH} h_{CH_3OH}}{\eta_{meth-electrol}} \quad \text{(Eq.42)}$$

The enthalpy terms were determined using the same method previously analyzed in Section 3.2.

Similarly, the energy loss is calculated using the same formula applied for the PEM electrolyzer:

$$\left(\frac{dE}{dt}\right)_{lost} = \dot{W}_{ext,meth-electrol} - \dot{m}_{H_2} HHV_{H_2} \quad \text{(Eq.43)}$$

It is used to calculate the life cycle cost.

Parameter	Value	Uncertainty
j (A/cm^2)	0,15	5%
electrolyzer efficiency	0,3397	5%
Yearly O&M (%C_electrol)	0,20%	5%
M-L refurbishment (%C_electrol)	200%	5%
End of Life (%C_electrol)	10%	5%
T0 (°C)	25	1%
T_CO2 (°C)	80	1%
T_H2 (°C)	80	1%
T_H2O (°C)	25	1%
T_CH3OH (°C)	25	1%
p0 (kPa)	100	1%
p_O2 (kPa)	5000	1%
p_H2 (kPa)	5000	1%
p_H2O (kPa)	5000	1%
p_CH3OH (kPa)	5000	1%
$\Delta h^0_{f,H2}\left(\frac{kJ}{mol}\right)$	0	0%
$\Delta h^0_{f,CO2}\left(\frac{kJ}{mol}\right)$	-393,522	0%
$\Delta h^0_{f,H2O}\left(\frac{kJ}{mol}\right)$	-285,83	0%
$\Delta h^0_{f,CH3OH}\left(\frac{kJ}{mol}\right)$	-238,81	0%
HHV_H2 (MJ/kg)	141,88	0%

Table 10. Assumptions for methanol electrolysis plant (Excel) [32]

3.8 Carbon capture

This study focuses on CO_2 capture using zeolites, with particular attention to 13X-type zeolites. These are the most widely studied in the scientific literature, both from a technical and economic perspective. Recent research highlights their potential for CO_2 capture from flue gas streams due to their high adsorption capacity and strong selectivity towards CO_2. This type of zeolite features a combination of micropores and mesopores; its physical characteristics are presented in *Table 11* [36].

Parameter	Value
Particle Porosity	0,37
Crush Stregth	≥ 50 N
Bed Void Fraction	0,4912
Langumuir Surface Area	585,5 (m^2/ g)
Total Pore Volume	0,27 (cm^3/ g)
Apparent Density	641 (kg/m^3)
Average Pore Diameter	0,8 (nm)
Average Particle Diameter	1,4 8mm)
Particle Shape	Spherical

Table 11. Physical properties of the 13X zeolite [36]

The main characteristics of 13X zeolite include its porous structure, high selectivity, large surface area, thermal stability, and adsorption capacity. The spherical shape of the particles enhances optimal gas-solid interaction and allows for more efficient packing [36].

The choice of zeolites over amine-based solutions is driven not only by these favorable properties, but also by their higher CO_2 removal efficiency and lower energy consumption, as illustrated in the comparison in *Table 12*.

	CO2 sorption capacity (mol CO2/kg solvent)	CO2 removal efficiency (% vol.)	Energy consumption for CO2 Capture (GJ/tCO2)	CO2 capture cost (USD/t CO2)
Absorption (MEA)	4,09	85-90	3,8	62,8
Adsorption (13X zeolite)	6,18	88-95	1,17	89,66

Table 12. Technical comparison between the MEA absorption and the 13X zeolite adsorption (Excel) [35]

However, it is important to note that energy consumption also depends on the specific regeneration process used for the zeolites, namely TSA (Temperature Swing Adsorption), PSA (Pressure Swing Adsorption), or VPSA (Vacuum Pressure Swing Adsorption).

Considering the commercial zeolite 13X-APG as the adsorbent material, the reference system will be a VPSA (Vacuum Pressure Swing Adsorption) plant, as studied by R. Gonzalez-Olmos et al. [37]. This process was selected because it has been identified as the most effective method in terms of both productivity and energy efficiency [37].

As previously mentioned, carbon capture is necessary for both the DMFC plant, which generates electricity, and the MEC plant, which produces hydrogen. From an economic point of view, the goal is to calculate the LCOE and LCOH, respectively, once CCS (Carbon Capture and Storage) is implemented.

To evaluate the cost of a zeolite 13X-based CCS system, reference will be made to the data presented in *Figure 6*.

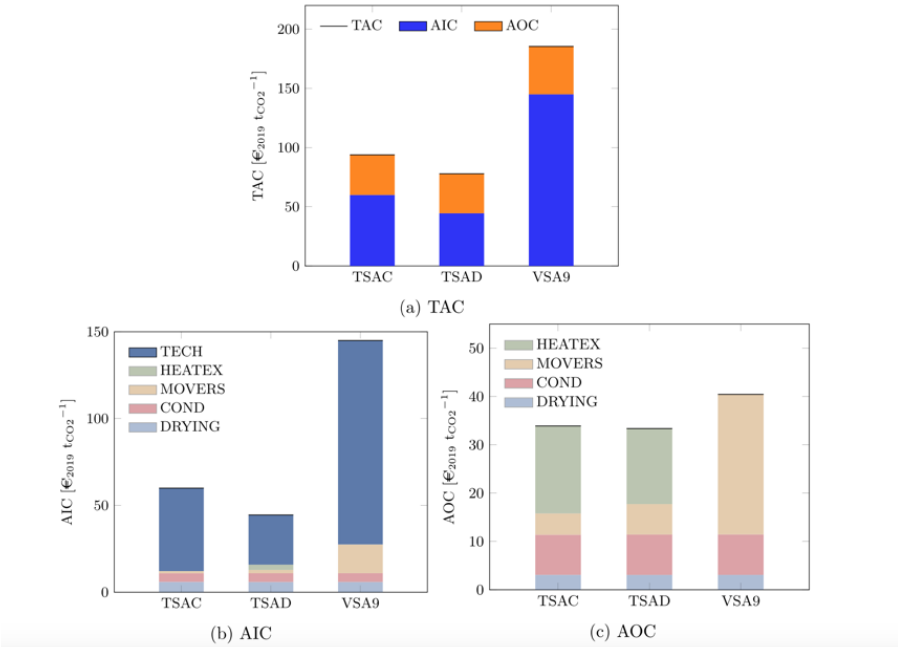

Figure 6. Costs per unit of CO2 capture for the minimum cost design at 90% recovery [39]

TAC stands for Total Annualized Cost, expressed in euros per unit mass of CO_2 captured. It is defined as the sum of the Annualized Investment Costs (AIC) and the Annual Operating Costs (AOC). The AOC mainly consists of the cost of the energy consumed, whereas the AIC accounts for the costs of all the equipment required for CO_2 capture.

The cost calculation is performed for two Temperature Swing Adsorption (TSA) cycle configurations and for the Vacuum Swing Adsorption (VSA) process. In particular, the VSA9 configuration is considered in this analysis, as it represents a more advanced and efficient variant of the base cycle.

For the VSA process, the main cost contribution falls under the TECH category, which refers to the adsorption columns. The other components include fans, compressors, and vacuum pumps, grouped under the MOVERS category. Heat exchangers (HEATEX) are not present in a pressure-driven system such as the one analyzed in this study.

Finally, the auxiliary units comprise the conditioning unit (COND) for CO_2 liquefaction and the pre drying unit (DRYING) [39].

4 EXPERIMENTAL PROCEDURE

4.1 Nafion 117 membrane treatment

The membrane material used in the single DMFC to be tested is Nafion 117. The first two digits indicate the equivalent weight of Nafion, which is defined as the weight of the polymer that neutralizes one equivalent of base. Typically, and in this case as well, the equivalent weight is 1100.

The last digit, 7, represents the membrane thickness, which is 7 mils (0,1778 mm). Nafion 117 membranes were the first to be studied, and their use today is mostly limited to DMFC applications [33].

The procedure followed by the PiCoHiMA research group to treat the Nafion membrane, which will later be used as the electrolysis layer in the DMFC, is outlined below. Two membranes were treated simultaneously.

1. Cut the Nafion membranes into 5x5 cm squares using a cutter, handling them with gloves and being careful not to bend them.
2. Place the membranes in a glass crystallizer containing a 30% hydrogen peroxide (H_2O_2)solution at 80ºC for one hour. During this step, it is crucial to ensure that no bubbles form on the membranes, as they could damage them. To prevent this, use a glass rod to gently move the membranes, being careful not to touch the center, in order to remove any bubbles and keep the membranes at the bottom of the crystallizer, preventing them from floating.
3. Carefully remove the membranes from the solution using tweezers, holding them by the edges, and rinse them with distilled water.
4. Place the membranes vertically in a beaker with one liter of distilled water at 80ºC, which is then placed in a thermostatic bath set at 90ºC for one hour, taking care to avoid bubble formation.
5. After this, remove the membranes from the distilled water and rinse them again with distilled water at room temperature.
6. Now, place the membranes in the crystallizer with 0,5 M sulphuric acid (H_2SO_4) at 80ºC for one hour, again ensuring that bubble formation is avoided, though it will be less than in the previous solution. This step is necessary to activate the membranes.
7. After removing the membranes, wash them again with distilled water.
8. Place the membranes back into the beaker with distilled water at 80ºC for another hour.
9. Once removed, place the membranes between two sheets of paper for about two hours to allow any excess moisture to evaporate.
10. Finally, place the membranes between two dry sheets of paper with a weight on top, leaving them in this state for at least 48 hours.

It is important to note that all equipment used for preparing the solutions and treating the Nafion must be washed with a micosol solution and distilled water.

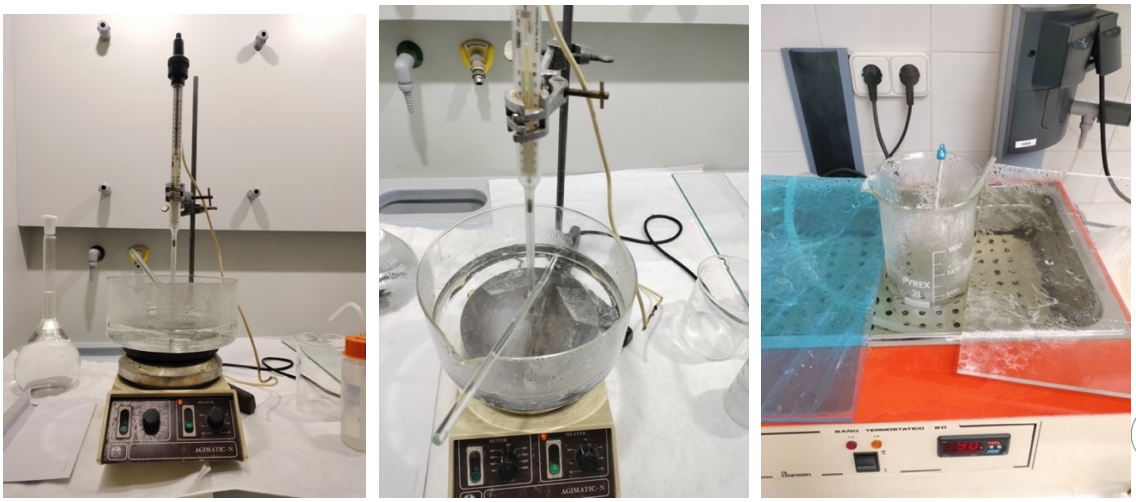

Figure 7. (7.1) and (7.2) Heater with the crystallizer containing the 30% hydrogen peroxide solution and the two Nafion membranes; (7.3) Thermostatic bath in which is placed the beaker with the membranes and a thermometer.

4.2 MEA and single cell assembly

Once the Nafion membrane is ready, it is time to assemble the Membrane Electrode Assembly (MEA). As previously described, the MEA consists of a central Nafion membrane with two electrodes on either side. For this assembly process, a specialized tool, 3D-printed directly in the laboratory, will be used.

The procedure step by step is the following one.

1. Take the pre-cut electrodes (4x4 cm). The anode has a PtRu catalytic layer, while the cathode has a Pt catalytic layer. On the opposite side of both electrodes, there is the Gas Diffusion Layer.
2. Spray the catalytic side of the electrodes with a Nafion solution using an airbrush connected to a compressor. This helps bond the electrode to the membrane.
3. Let the electrodes dry on a sheet of paper for a few minutes, like it is shown in *Figure 8*.
4. Proceed with the assembly by positioning the electrodes on both sides of the membrane, ensuring they face the Nafion-coated side. An aluminum foil is placed between the tool surface and the Gas Diffusion Layer side of the membrane.
5. Carefully remove the two frames holding the membrane in place and secure the MEA using clamps.
6. Now that the MEA is positioned between two aluminum foils, place it between two metal plates and insert them into a heated press.
7. Once the MEA reaches 130°C (as measured with a thermal probe), apply a pressure of 60 bar and maintain it for three minutes (*Figure 9.1* and *Figure 9.2*).
8. Remove the MEA from the press and peel off the aluminum foils attached to the electrodes.
9. Place 0,3 mm thick silicone gaskets (previously cut to size with a cutter) on both steel plates.

10. Position the MEA on the plates, ensuring that the anode and cathode align correctly with the corresponding plate faces.
11. Secure the silicone gaskets and bolts, tightening them evenly to distribute pressure uniformly, at first applying 1,5 Nm and then increasing it at 1,8 Nm.

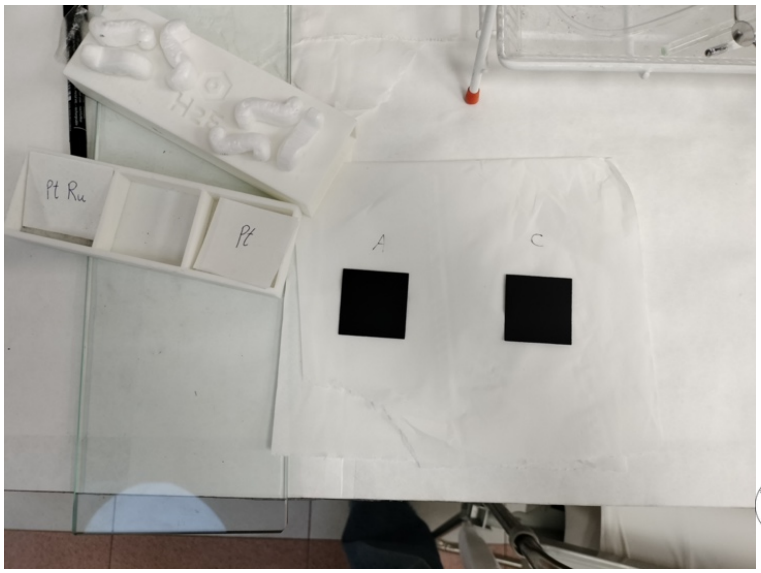

Figure 8. Anode and Cathode after the coating spray with liquid Nafion on the catalyst layer

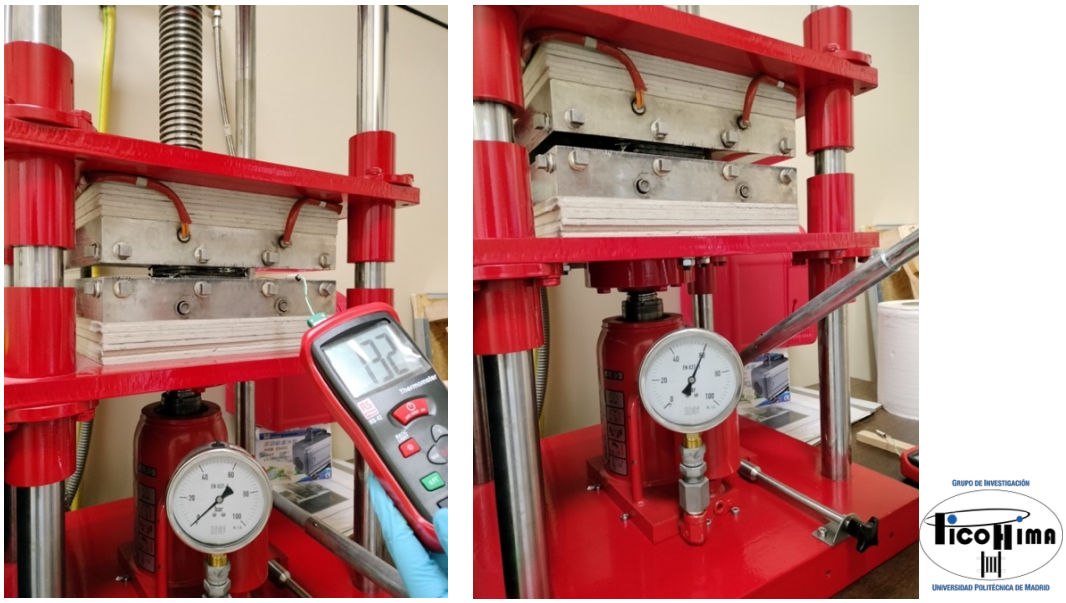

Figure 9. (9.1) Heated press for the MEA treatment at 130°C and 60 bar; (9.2) Close-up of the MEA inside the press

The procedure described above will be repeated six times. This is because measurements will be taken on single fuel cells with different types of flow field plates on the anode side. The cathode-side plate remains unchanged. Consequently, the Nafion membrane treatment procedure must also be repeated. The characteristics of the different flow field plates are summarized in *Table 13*.

	Number of channels	Channels width (mm)	Channels depth (mm)
DMFC 1 (2025-03-31)	21	1,133	0,9
DMFC 2 (2025-05-05)	29	0,825	0,9
DMFC 3 (2025-05-19)	14	0,825	1,7
DMFC 4 (2025-06-02)	14	0,825	0,9
DMFC 5 (2025-06-16)	21	1,133	1,7
DMFC 6 (2025-06-30)	10	1,133	1,7

Table 13. Anode flow field plate characteristcs (Excel)

In contrast to what was described in Section 2.2.2 for the DMFC stack components, the flow field plates used in a single fuel cell are clearly not bipolar. They have flow channels only on the surface in contact with the electrodes.

4.3 DMFC test bench

To evaluate the operation of the assembled fuel cell, a test bench consisting of several components is required:

- two insulating chambers, inside which the fuel cell is placed (1);
- a fan outside the internal chamber;
- a cryothermostat to heat the chamber containing the fuel cell to 60°C and maintain this temperature (2);
- a thermostat to heat the water supplied to the fuel cell only during activation;
- a tank with the methanol solution (3);
- a pump that delivers the methanol solution to the anode (4);
- temperature and pressure sensors;
- a potentiometer and current booster (5);
- two computers for data acquisition (6);
- an oxygen vessel (7).

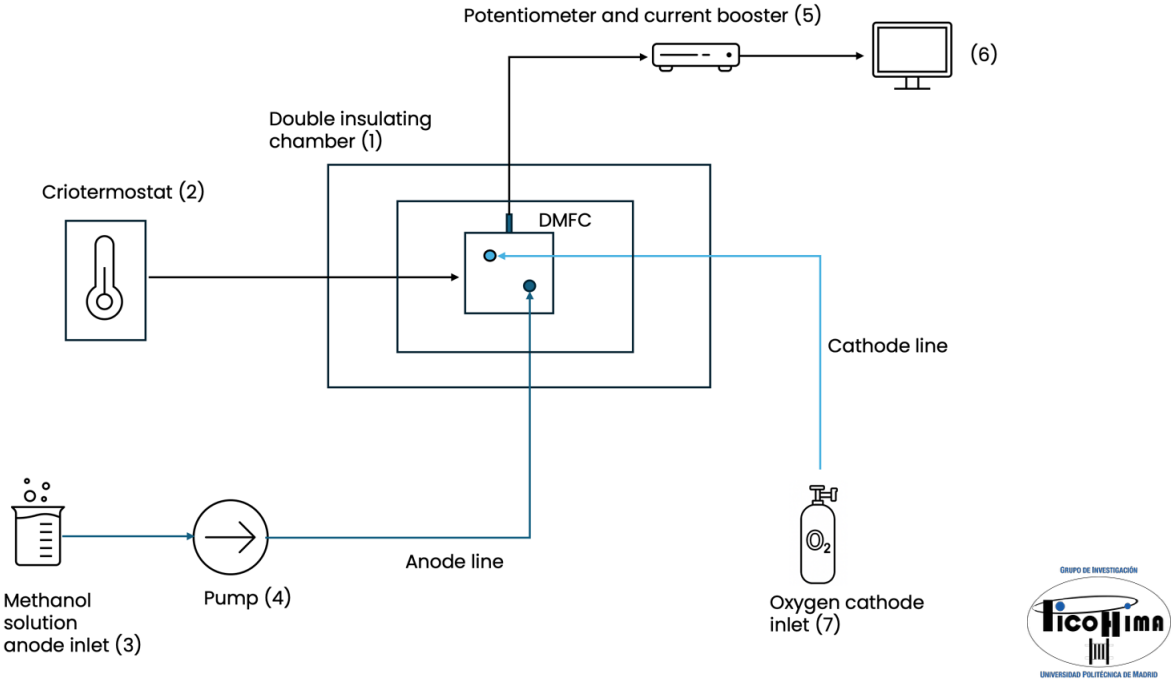

Figure 10. Schematic diagram of the DMFC test benchmark (PowerPoint)

The procedure for starting up, operating, and measuring the performance of the assembled single fuel cell begins by turning on the cryothermostat to bring the fuel cell to 60ºC, using a temperature probe to monitor the temperature inside the insulated chamber and ensure it remains constant. The fan is also activated. Measurements can only begin once the fuel cell has reached the set temperature. The thermostat reservoir (water bath) is filled with distilled water and heated to 60ºC, as the Nafion membrane must remain hydrated to facilitate proton transport. Initially, external water supply is necessary, but once the fuel cell starts operating, the water it produces is sufficient. This step is required only for the first activation of the fuel cell. A tank with a 1M methanol-water solution is prepared and placed at an elevated, tilted position. It has two openings: one for adding the solution and another connected to the pump that supplies methanol to the fuel cell. The pump operates at 0,06 MPa and 3 mL/min. The pump valve remains closed initially and is opened once all air is purged from the circuit.

The fuel cell is housed in a transparent insulated box, which is itself enclosed within another insulating chamber. Operators can access the cell through an opening on top to connect the tubes, which pass through a small front hole in both boxes. At the anode, methanol solution enters from the bottom inlet, while CO_2 and water exit through the top outlet and flow into a beaker. At the cathode, oxygen enters from the top, and water and residual methanol exit from the bottom into a separate container. Another front hole allows for the insertion of the temperature probe to continuously monitor the fuel cell's temperature. The electrical wires (red and black) are connected through the upper openings of the enclosures, and both chambers are closed, sealing any remaining openings with plugs. The oxygen tank valve is opened, the knob is adjusted, and the

indicator light is turned on; all of these components are located on the right side of the fuel cell system.

Once the setup is complete, the potentiometer and Autolab current booster are switched on, and the computers are started to monitor the fuel cell's operation. One computer controls the mass flow rate and pressure, while the other acquires data for the polarization curve, averaging values for each point. The measured cathode pressure must be 1 bar, and the oxygen volumetric flow rate is 110,01 mL/min. The currents used to plot the polarization curve are acquired using Nova 2.1 software, decreasing the voltage by 0,02 V every three minutes. The data are saved in an Excel file. Four polarization curves are typically measured per day for two weeks, with the first curve generally being the least efficient and improving as the fuel cell warms up. Before starting a new measurement, it is essential to ensure that no air bubbles remain in the methanol circuit, as they could distort the results.

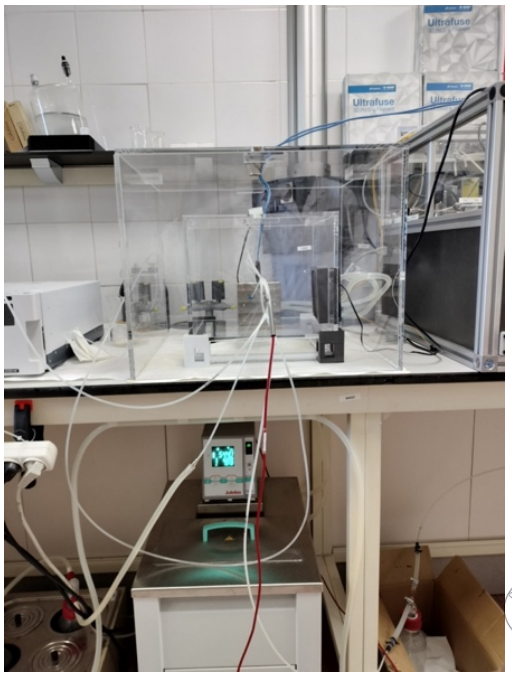

Figure 11. DMFC positioned in the double insulating chamber and the cryothermostat heating the cell

4.4 CO2 emission measurement test bench

The measurement of CO_2 emissions is carried out using a gas chromatograph. The water/CO_2 mixture coming from the anode of the DMFC is connected to a gas-liquid separator, which collects the water and sends only the CO_2 to the gas chromatograph. The separated gas first passes through a filter to ensure its purity and then flows through two chromatographic columns for analysis. The amount of CO_2 is determined based on the signal detected on Channel 4, which is set at the beginning of the procedure. After completing the measurements, the DMFC is disassembled to assess its internal condition.

Figure 12. Gas-liquid separator connected to the anode output of CO2/water mixture

Figure 13. Gas cromatograph used for the CO2 measurements

5 RESULTS AND DISCUSSION

5.1 Polarization curves and power curves

The following section analyzes the results obtained from tests conducted on the assembled DMFCs. To evaluate their performance, it is necessary to study the derived polarization curves and power curves.

It is important to note that each DMFC was tested over a two-week period, with measurements taken four times a day, excluding the first two runs, which were used for cell activation.

Identifying the best-performing DMFC is crucial, as it will serve as the reference for the economic calculations. Therefore, the different DMFCs will be compared based on their best recorded polarization and power curves.

5.1.1 DMFC 1

For the first DMFC tested, the anode plate has a single serpentine flow field design with a countercurrent flow of the inlet and outlet. The technical specifics of the geometry are in *Table 13.*

Figure 14 and *Figure 15* show the curves measured on the first day (after activation) and the last day of testing, respectively.

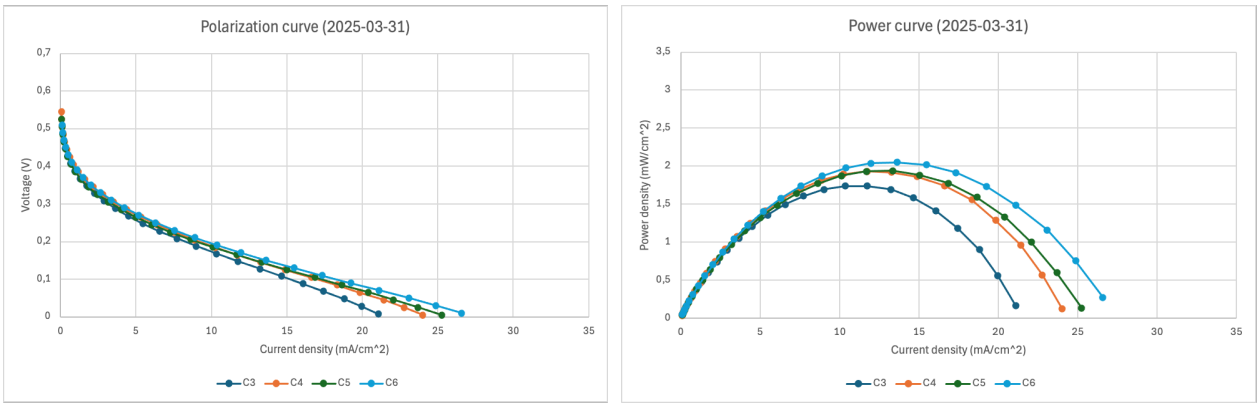

Figure 14. (14.1) Polarization curves and (14.2) Power curves measured in the first day for the DMFC 1(Excel)

In *Figure 14*, it can be observed that in the activation region, the curves are closely aligned, but they begin to diverge in the ohmic region.

The limiting current density corresponds to the current density at which the cell voltage drops to zero. It represents the maximum current the cell can sustain before complete voltage loss. For these initial curves, the limiting current density is between 20 and 30 mA/cm², which is relatively low. This suggests that there are issues with reactant diffusion within the cell.

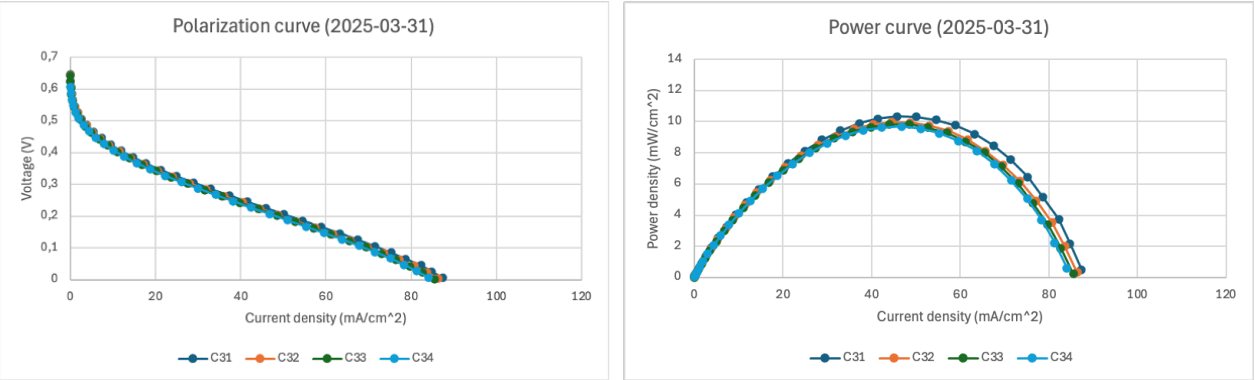

Figure 15. (15.1) Polarization curves and (15.2) Power curves measured in the last day for the DMFC 1(Excel)

Figure 15 shows the curves measured on the last day of testing. In this case, the curves are much closer to each other along their entire length. They exhibit a higher open-circuit voltage compared to those shown in *Figure 14* from the first day, as well as a higher limiting current density, ranging between 80 and 90 mA/cm². Additionally, they show a greater power density, which is achieved at a higher current density.

Under identical operating conditions of temperature, pressure, and reactant flow rate, the performance of the DMFC on the last day proves to be clearly better than on the first day. One possible explanation is that the Nafion membrane was not yet fully hydrated during the first day of testing, despite the activation process carried out the day before. As previously mentioned, Nafion hydration plays a fundamental role in proton transport and, consequently, in the electrochemical performance of the cell.

Another factor that may have contributed to the improvement is a better contact between the electrodes and the electrolyte layer, resulting from membrane expansion over time, which occurs both due to thermal effects and water absorption. CO_2 bubbling is also a likely cause. The incomplete removal of CO_2 bubbles formed in the flow channels can lead to their blockage, which in turn causes mass transport losses, as the necessary amount of reactants cannot reach the electrode surface efficiently. This type of issue is closely related to the channel configuration.

The first DMFC tested was equipped with 21 flow channels, each with a channel width of 1,133 mm and a channel depth of 0,9 mm. It featured a single serpentine flow field design, with the inlet and outlet located on opposite sides of the anode plate, specifically, the inlet at the bottom and the outlet at the top. This setup leads to a countercurrent-like configuration between anode and cathode flow paths. Although this improves reactant distribution uniformity, it also results in the highest pressure drop along the serpentine, generating differential mechanical stress across the MEA [20].

In order to calculate the efficiency of the first DMFC, the curve corresponding to the highest current density will be used. This is the second curve from the last day of testing, identified as curve number 31.

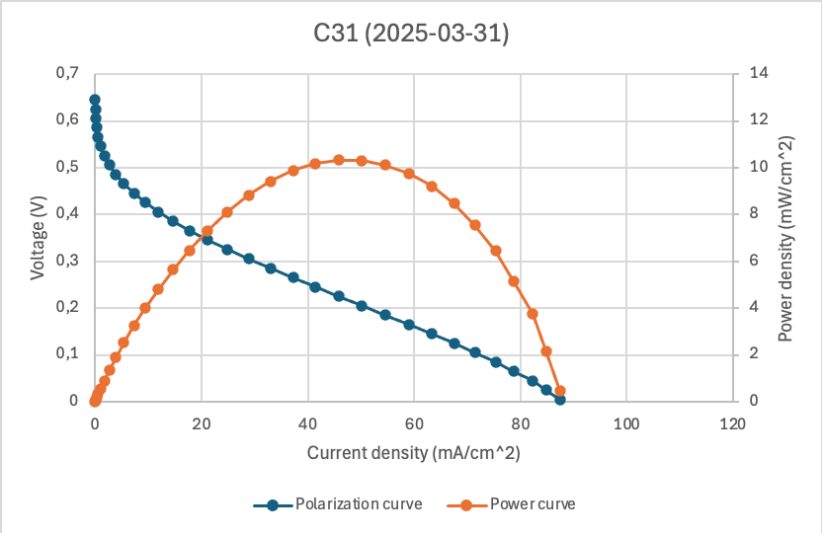

Figure 16. Best curve measured for the DMFC 1(Excel)

The maximum power density achieved was 10,33 mW/cm², considering an active area of 16 cm², and it occurred at a current density of 45,82 mA/cm². This current density will be used as the reference value for this first DMFC, as it represents the optimal operating point of the cell.

5.1.2 DMFC 2

The results obtained for the second tested DMFC are now analyzed. Compared to the first cell, this one features a higher number of channels, a smaller channel width, and the same channel depth, as shown in *Table 14*. This is also an anode plate with a single serpentine flow field design with the inlet and outlet at the opposite side of the plate.

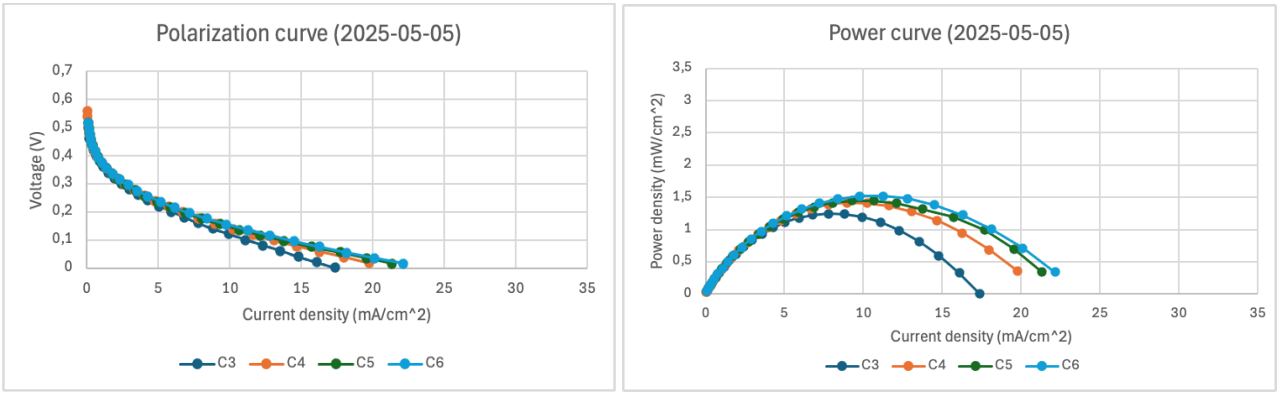

Figure 17. (17.1) Polarization curves and (17.2) Power curves measured in the first day for the DMFC 2 (Excel)

As shown in *Figure 17*, the trend of the curves is similar to that observed for the first DMFC. However, the limiting current density is lower, ranging between 15 and 25 mA/cm². The maximum power density is also reduced: while the best curve on the first day for the previous DMFC reached approximately 2 mW/cm², in this case it is around 1,5 mW/cm².

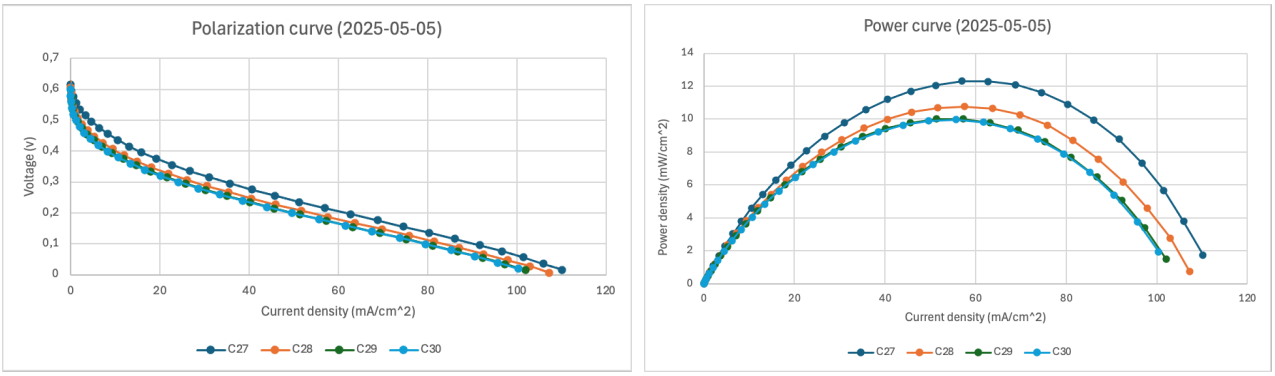

Figure 18. (18.1) Polarization curves and (18.2) Power curves measured in the last day for the DMFC 2 (Excel)

As for the curves recorded on the final day in *Figure 18*, they appear to be closely grouped, as observed for DMFC 1, except for curve 27, which is the first of the last day. This curve shows a significantly higher power density compared to the others from the same day and also those from the final day of DMFC 1. The latter displayed a maximum power density of around 10 mW/cm², as did curves C29 and C30 from 2025-05-05. As shown in Figure 19, curve C27 reaches 12,29 mW/cm² at a current density of 57,02 mA/cm². It therefore represents the best performing curve measured for DMFC 2 and it will be used as the reference.

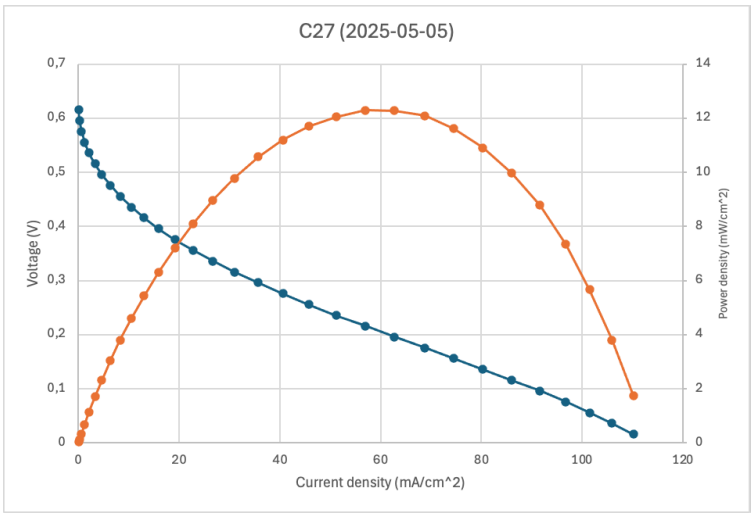

Figure 19. Best curve measured for the DMFC 2 (Excel)

The comments made for the first DMFC regarding the differences between the curves measured on the first and last day of testing remain valid.

Regarding the differences between the curves plotted for the first and second DMFCs, these can be attributed to the change in the anode flow field plate, since the operating conditions remained unchanged. As previously mentioned, the differences between the plates concern the number of flow channels and the channel width: the number of channels increases, and consequently, the channel width decreases, while the active area remains constant at 16 cm².

In summary, it can be observed that on the first day of testing, DMFC 1 showed a slightly better performance than DMFC 2. However, on the last day, the situation is reversed, with DMFC 2 performing better than DMFC 1 in both limiting current density and maximum power point.

The wider channels of DMFC 1 initially provide more uniform methanol distribution and lower pressure drops, resulting in better early performance. On the other hand, the higher number of narrower channels in DMFC 2 may initially lead to greater flow resistance and local non uniformity of fuel distribution. However, over time, these channels improved reactant transport and CO_2 removal once the system stabilizes, ultimately leading to superior performance on the final day.

5.1.3 DMFC 3

The third tested DMFC, unlike the first two, features an anode plate with a single serpentine flow field in which both the inlet and outlet are located on the same side of the plate. Additionally, the anode plate used in this case has a significantly lower number of flow channels (14), the same channel width as DMFC 2, but a greater channel depth, as shown in *Table 13*.

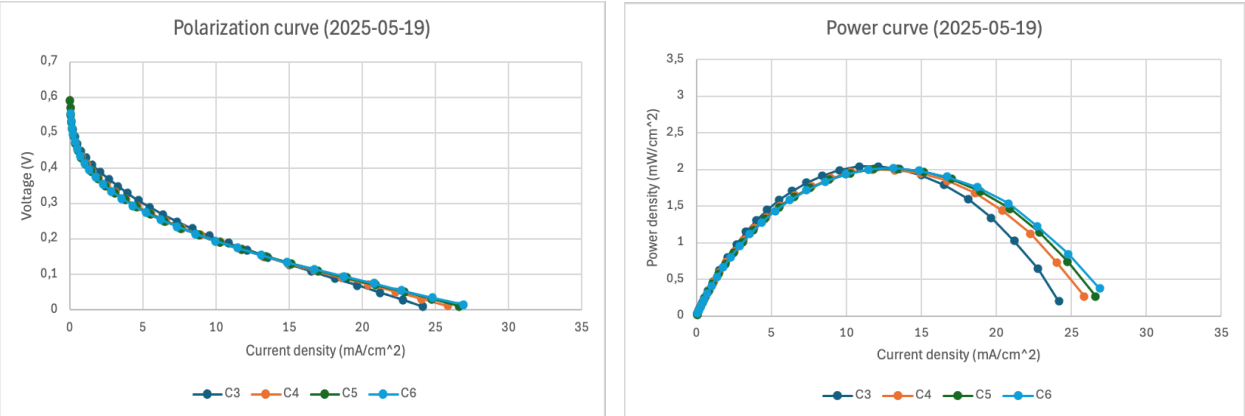

Figure 20. (20.1) Polarization curves and (20.2) Power curves measured in the first day for the DMFC 3 (Excel)

As it can be seen in *Figure 20*, the curves recorded on the first day of testing are similar to those of DMFC 1 in terms of limiting current and maximum power point values, but they appear to be more closely grouped.

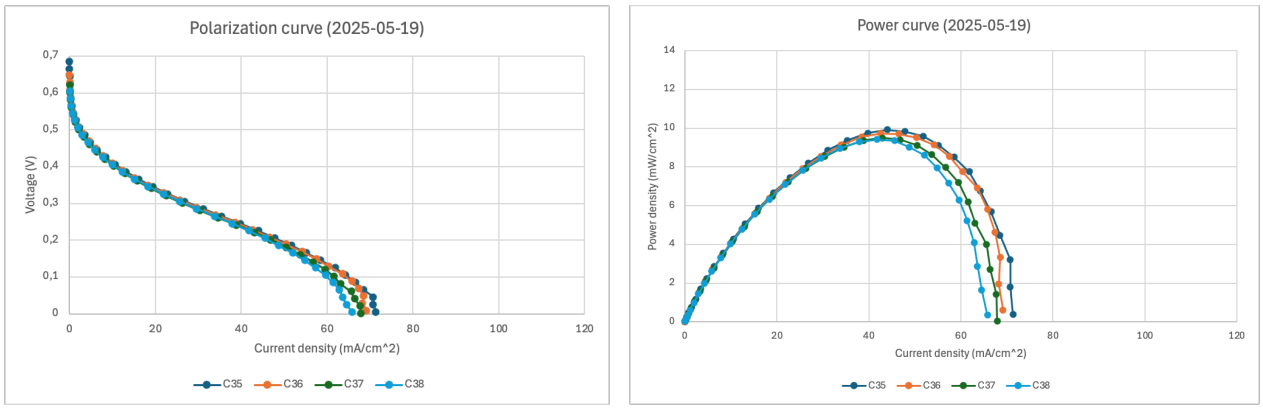

Figure 21. (21.1) Polarization curves and (21.2) Power curves measured in the last day for the DMFC 3 (Excel)

In *Figure 21*, it can be observed that the curves from the last day show a significantly lower limiting current compared to DMFC 1 (ranging between 80 and 90 mA/cm²) and DMFC 2 (between 100 and 120 mA/cm²). Regarding the maximum power point, DMFC 3 reaches values around 9 mW/cm², with the corresponding current density between 40 and 50 mA/cm².

So far, this is the lowest power density among the tested DMFCs, despite the maximum current density falling within the same range as that of DMFC 1. It should also be noted that the membrane deteriorated during the final days of DMFC 3. The pressure of the pump supplying methanol to the anode increases as it attempts to push the reactants through the few channels present, which are obstructed by CO_2 and water. Indeed, the final part of the polarization curve, which corresponds to the concentration losses region, appears to be inaccurate.

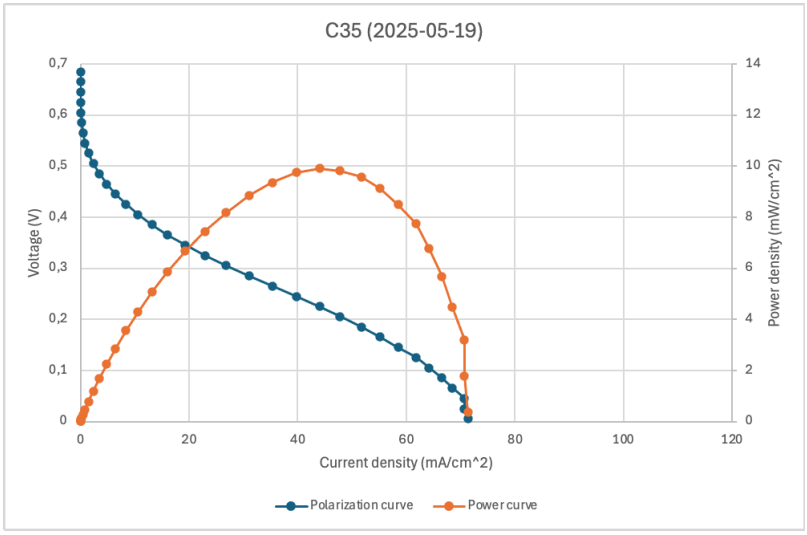

Figure 22. Best curve measured for the DMFC 3 (Excel)

The best-performing curve measured for DMFC 3 is shown in *Figure 22* and corresponds to curve C35, which was the first curve recorded on the final day. The maximum power density is 9,91 mW/cm², and the maximum current density is 44 mA/cm².

For this DMFC as well, a comparison with the previous two can be made based on the different geometry of the anode flow field plate. The lower number of flow channels, combined with the fact that the channel width is the same as in the DMFC with a much higher number of channels, results in a slightly lower power density on the last day. This is likely due to a less uniform fuel distribution. On the other hand, the greater channel depth compared to the other DMFCs facilitates the removal of CO_2, at least before reaching the maximum power point.

5.1.4 DMFC 4

For this DMFC as well, the anode flow field plate features a single serpentine configuration, with both the inlet and outlet on the same side, as in the previous DMFC. The number of channels and the channel width are also the same as in the previous cell; the only parameter that differs is the channel depth, which returns to 0,9 mm.

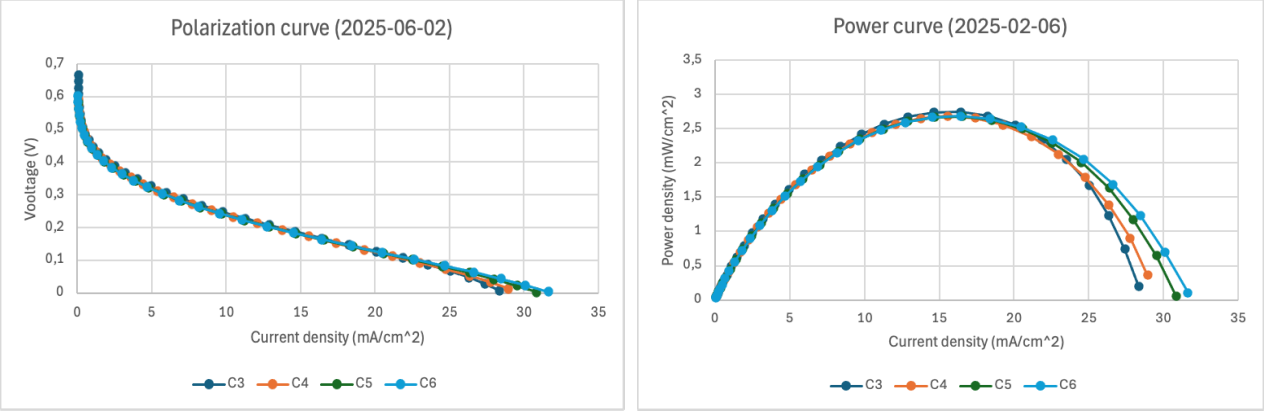

Figure 23. (23.1) Polarization curves and (23.2) Power curves measured in the first day for DMFC 4 (Excel)

It can be observed that the limiting current density is the highest among the DMFCs tested so far, exceeding 30 mA/cm². Referring to the power curve, it is also evident that the maximum power achieved is higher, reaching over 2,5 mW/cm². We can therefore state that, even by simply reducing the channel depth compared to DMFC 3, improved performance can be obtained, at least on the first day of operation.

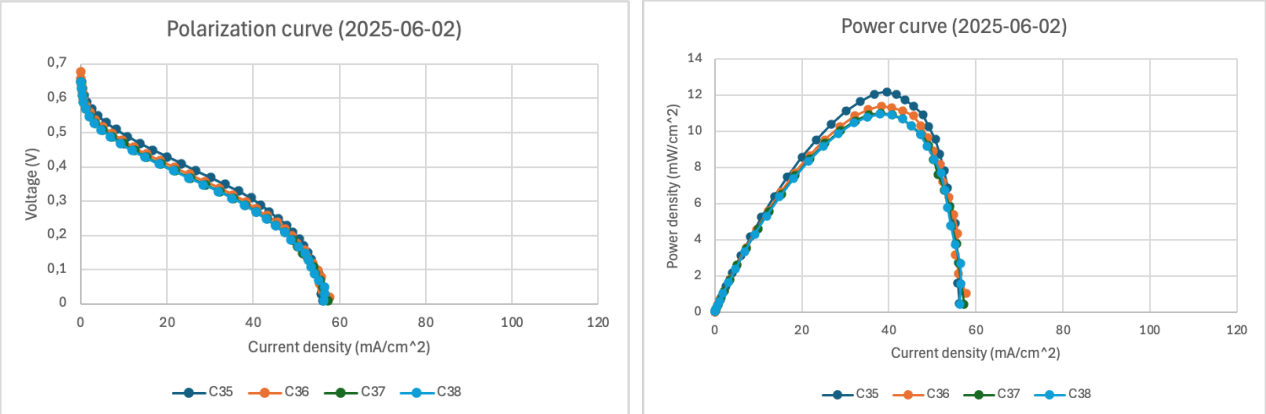

Figure 24. (24.1) Polarization curves and (24.2) Power curves measured in the last day for DMFC 4 (Excel)

In contrast to what was observed on the first day, the limiting current density is now significantly lower than the previous DMFCs, almost half that of DMFC 2. As a result, the peak of the power curve shifts toward lower current values. Nevertheless, the maximum power density remains comparable to that of DMFC 2, reaching up to 12 mW/cm² in the best case, and around 11 mW/cm² for the others.

As observed for DMFC 3, a performance degradation occurred in DMFC 4 during the final days of operation, likely due to membrane degradation. This was accompanied by an increase in the pressure required by the methanol feed pump, indicating a higher flow resistance. Such behavior can be explained by the partial blockage of the channels caused by the accumulation of CO_2 and water, which hinders reactant transport and leads to instability in cell operation.

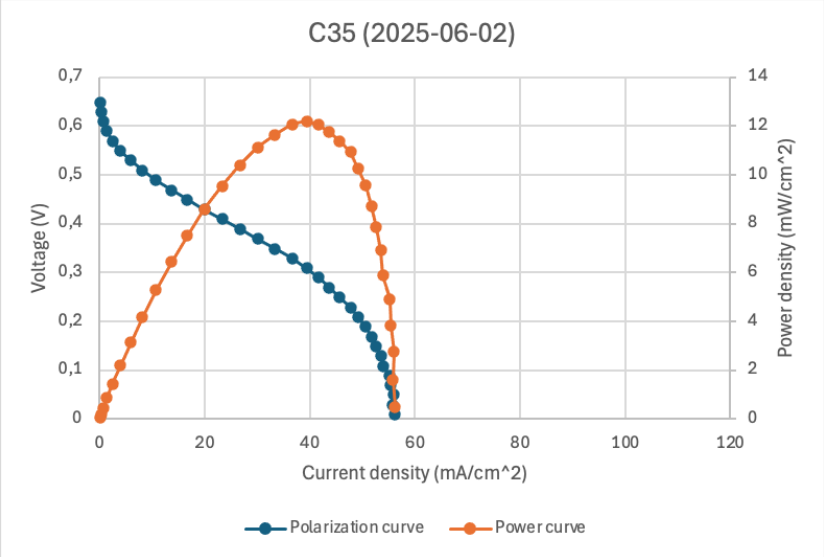

Figure 25. Best curve measured for DMFC 4 (Excel)

As already mentioned, the best-performing curve shows a peak at 12.197 mW/cm², corresponding to a current density of 39,478 mA/cm². The voltage at this current density is 0,308 V. This value is essential for assessing the cell's performance: in fact, it manages to achieve a power density comparable to DMFC 2, thanks to a lower current density and a higher voltage. Therefore, the cell operates in a more favorable region of the polarization curve compared to all the previously tested DMFCs.

5.1.5 DMFC 5

For the fifth fuel cell tested, the anode plate features inlet and outlet ports positioned on opposite sides. The number of channels increases compared to the previous configuration, reaching 21, while both the channel width (1,133 mm) and depth (1,7 mm) are also larger.

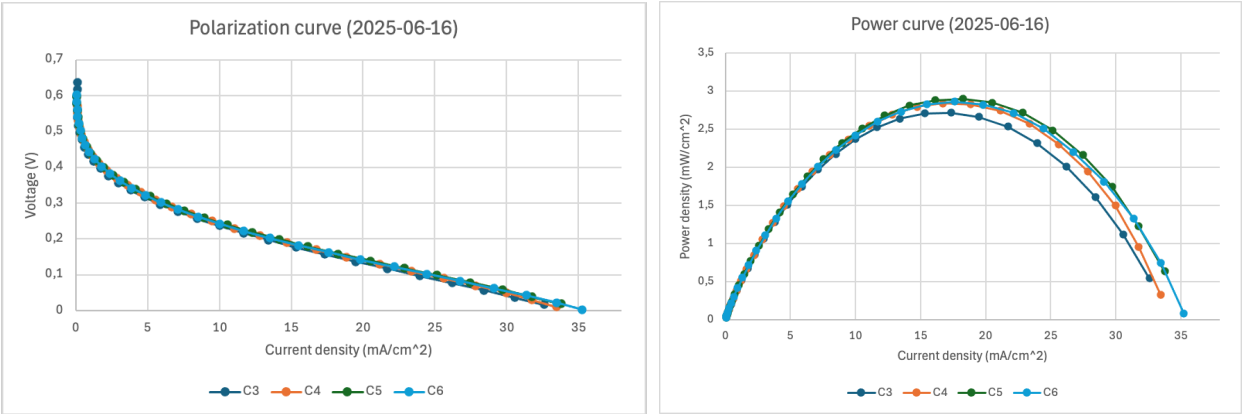

Figure 26. (26.1) Polarization curves and (26.2) Power curves measured in the first day for DMFC 5 (Excel)

During the first day of testing, the best polarization curve shows a limiting current density of approximately 35 mA/cm², higher than that obtained with all the previously tested DMFCs. The improved mass transport at the anode can be attributed to a more uniform distribution of the reactants, resulting from the larger number of flow channels, which are also wider and deeper. The maximum power density achieved is likewise higher than in the other DMFCs, reaching about 3,3 mW/cm².

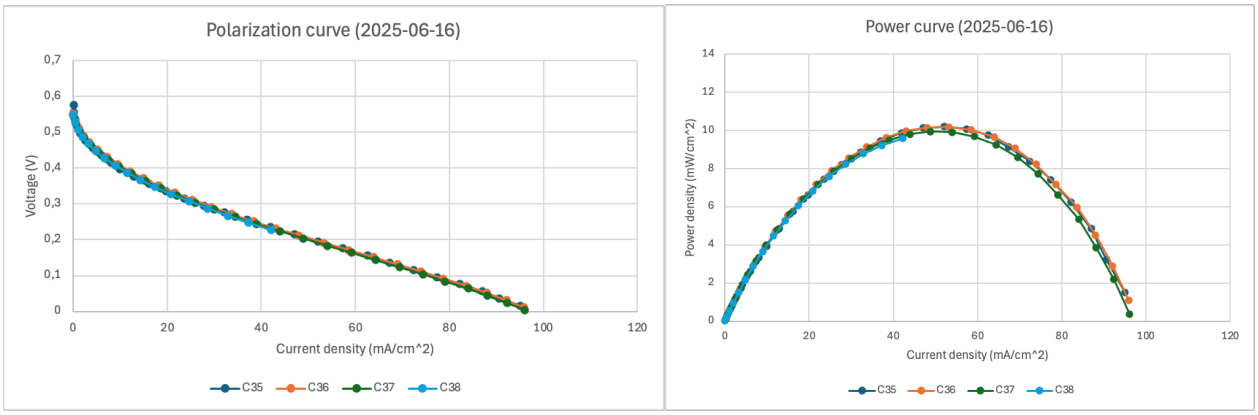

Figure 27. (27.1) Polarization curves and (27.2) Power curves measured in the last day for DMFC 5 (Excel)

In the last day, the limiting current density is not the highest, highlighting the role of channel depth. Recalling DMFC 1, its geometric parameters are mostly the same as those of DMFC 5, except for the greater channel depth in DMFC 5. Comparing *Figure 27* with *Figure 15*, which presents the curves from the last day of DMFC 1, both the limiting current density and the maximum power density show little variation. This contrasts with the first day of testing, where the differences with DMFC 1 were significant. In practice, the improvement obtained by increasing the channel depth is limited to the initial days of fuel cell operation. Over time, the advantage of greater depth becomes negligible due to the accumulation of CO_2 and water within the channels.

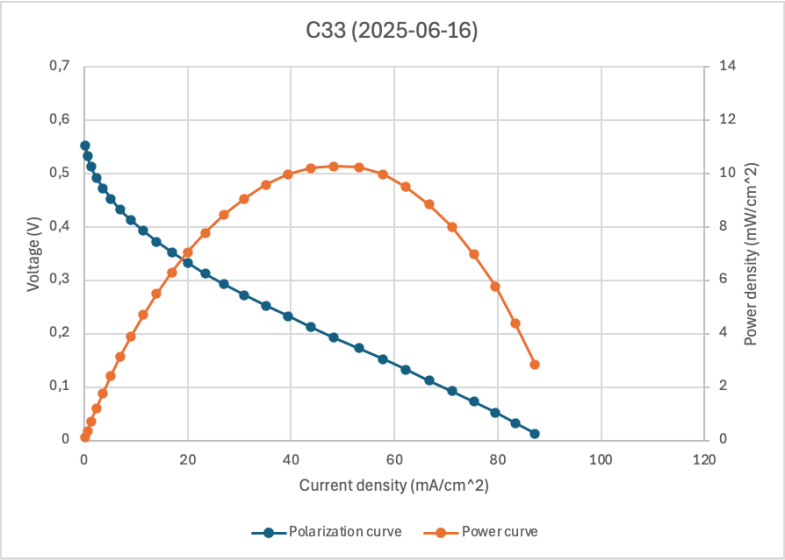

Figure 28. Best curve measured for DMFC 5 (Excel)

The highest power density, equal to 10,27 mW/cm², was achieved on the penultimate day with curve number 33. However, as previously noted, this value is lower than that obtained for other DMFCs tested and is very similar to the result of DMFC 1.

5.1.6 DMFC 6

In the sixth and final DMFC analyzed, both the inlet and outlet are located on the same side. This DMFC has the lowest number of channels (10), while the channel width and depth are the same as in DMFC 5, representing the largest values considered, namely 1,133 mm and 1,7 mm, respectively.

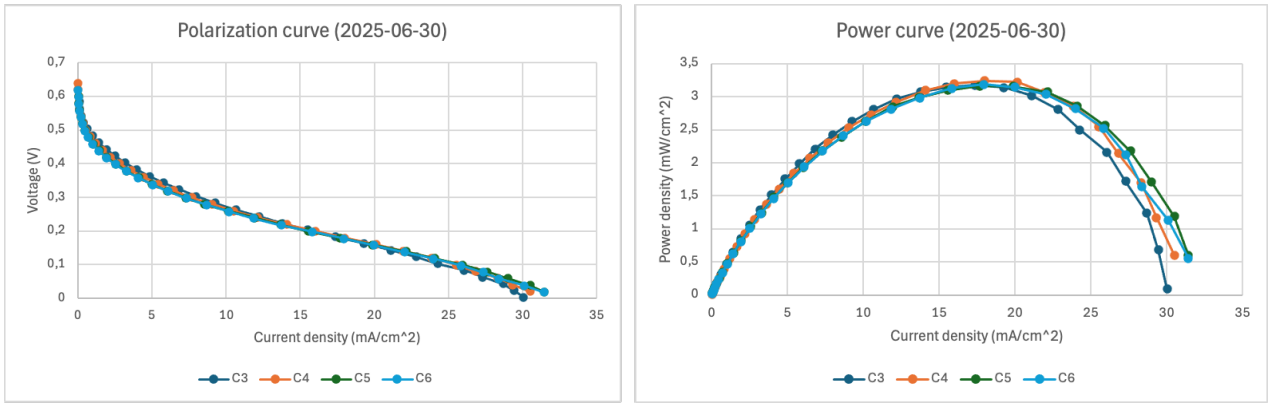

Figure 29. (29.1) Polarization curves and (29.2) Power curves measured in the first day for DMFC 6 (Excel)

The results obtained on the first day of testing are very similar to those of DMFC 5, with the limiting current density being slightly lower and the maximum power density comparable.

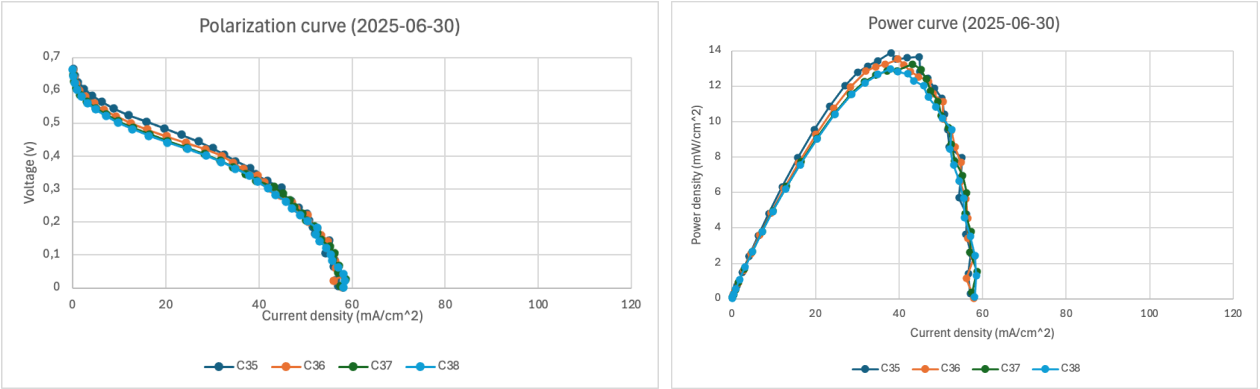

Figure 30. (30.1) Polarization curves and (30.2) Power curves measured in the last day for DMFC 6 (Excel)

On the final day of testing, it is observed that the maximum power density is the highest recorded among all DMFCs tested, while the limiting current density remains below 60 mA/cm², as is also the case for DMFC 4. Common characteristics include the low number of channels and the fact that both the inlet and outlet are located on the same side. Furthermore, in this case, instabilities occur once the current density associated with the maximum power density is exceeded, and these instabilities are even more pronounced than those already observed for DMFC 4. As previously noted for DMFCs with few channels, such as DMFC 3 and 4, an increase in pump pressure is observed, indicating a blockage in the channels caused by the accumulation of gaseous CO_2 and water. This, consequently, leads to the oscillations clearly visible in the polarization curve.

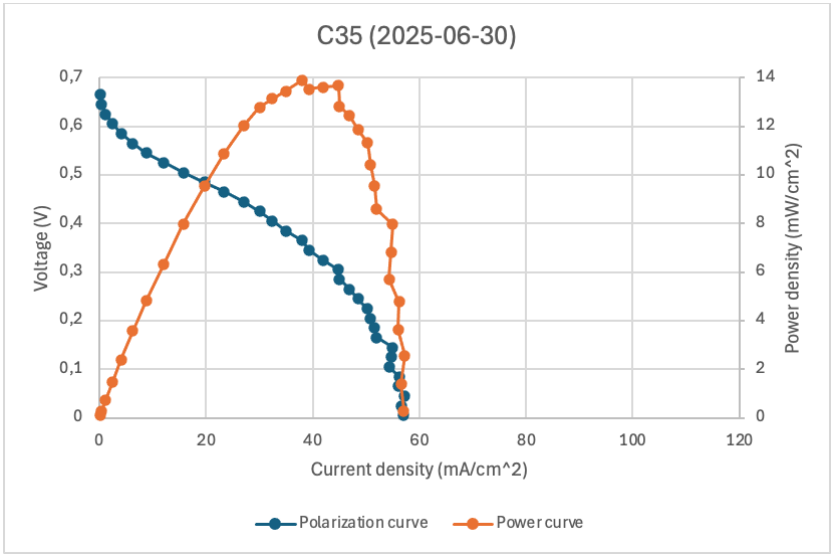

Figure 31. Best curve measured for DMFC 6 (Excel)

The best performance was achieved with curve C35, measured on the final day. As previously noted, the limiting current density remains low, while the maximum power density reaches 13,66 mW/cm², the highest recorded, corresponding to a current density of 44,81 mA/cm².

5.2 Efficiencies

Before calculating the efficiencies of the tested DMFCs, it is important to determine the methanol flow rate used.

As previously mentioned, all the DMFCs were supplied with the same 1 M aqueous methanol solution at a flow rate of 3 mL/min. This corresponds to a methanol molar flow rate of $5e-5$ mol/s at the anode.

$$\dot{m}_{CH3OH,real} = \frac{3 \cdot 10^{-3} \left[\frac{L}{min}\right]}{60} \cdot 1 \left[\frac{mol}{L}\right] = 5e-5 \left[\frac{mol}{s}\right] \quad \text{(Eq.44)}$$

Then, the actual methanol flow rate in mol/s was converted to g/s by multiplying it by the molar mass of methanol (MM_{CH3OH}= 32 g/mol).

$$\dot{m}_{CH3OH,real} \left[\frac{mol}{s}\right] \cdot 32 \left[\frac{g}{mol}\right] = 1{,}6e-3 \left[\frac{g}{s}\right] \quad \text{(Eq.45)}$$

To calculate the methanol flow rate that actually reacts at the anode, i.e. the stoichiometric methanol flow rate in mol/s, Faraday's law is used, as already shown in *Eq. 39*.

$$\dot{m}_{CH3OH,stoic} = \frac{i_{\max} \cdot S_{cell}}{z_{CH3OH} \cdot F} \quad \text{(Eq.46)}$$

In this case, the flow rate depends on the current, which varies for each DMFC. For this reason, the results are reported in *Table 14*. The active area (S_{cell}) is 16 cm², the number of electrons involved in the methanol oxidation reaction is 6, and *F* is the Faraday constant, as introduced earlier in Section 3.6.

Using the same equations, it is also possible to calculate both the actual and stoichiometric oxygen flow rates. As already mentioned in Section 4.3, an oxygen flow rate of 110,01 mL/min was supplied to the cathode. The stoichiometric flow rate, in this case as well, is calculated using Faraday's law (*Eq. 36*).

Since pure oxygen is used instead of air, the required volumetric flow rate is lower than it would be if air were used. However, this reduced flow rate may be insufficient to effectively remove the reaction products, leading to the accumulation of CO_2 and water, which in turn lowers the cell's performance.

	Power max (W)	Voltage mpp (V)	Current mpp (A)	Methanol mass flow rate stoic (mol/s)	Methanol mass flow rate stoic (g/s)	Methanol mass flow rate real (mol/s)	Methanol mass flow rate real (g/s)	Oxygen mass flow rate stoic (mol/s)	Oxygen mass flow rate stoic (g/s)	Oxygen mass flow rate real (mol/s)	Oxygen mass flow rate real (g/s)
DMFC 1 (2025-03-31)	0,165	0,225	0,733	1,3E-06	4,1E-05	5,0E-05	1,6E-03	3,8E-06	6,1E-05	6,7E-05	1,1E-03
DMFC 2 (2025-05-05)	0,197	0,215	0,912	1,6E-06	5,0E-05	5,0E-05	1,6E-03	4,7E-06	7,6E-05	6,7E-05	1,1E-03
DMFC 3 (2025-05-19)	0,159	0,225	0,704	1,2E-06	3,9E-05	5,0E-05	1,6E-03	3,6E-06	5,8E-05	6,7E-05	1,1E-03
DMFC 4 (2025-06-02)	0,195	0,308	0,632	1,1E-06	3,5E-05	5,0E-05	1,6E-03	3,3E-06	5,2E-05	6,7E-05	1,1E-03
DMFC 5 (2025-06-16)	0,205	0,276	0,745	1,3E-06	4,1E-05	5,0E-05	1,6E-03	3,9E-06	6,2E-05	6,7E-05	1,1E-03
DMFC 6 (2025-06-30)	0,218	0,305	0,717	1,2E-06	4,0E-05	5,0E-05	1,6E-03	3,7E-06	5,9E-05	6,7E-05	1,1E-03

Table 14. Maximum power point (mpp) parameters for the best performing curve of each DMFC and reactant flow rates, both stoichiometric and real (Excel)

It is now possible to calculate the fuel utilization (FU) in % for each single cell as follows:

$$FU = \frac{\dot{m}_{CH3OH,stoic}}{\dot{m}_{CH3OH,real}} \cdot 100 \qquad \text{(Eq.47)}$$

This parameter indicates how much of the methanol fed into the cell actually reacts to produce electricity. As shown in *Table 15*, the value is quite low for all the DMFCs, meaning that a significant portion of the methanol is not utilized. This loss is mainly due to crossover through the membrane, as well as transport related losses and not uniform fuel distribution. It should also be noted that the methanol feed rate used during the tests, equal to $1{,}6e-3\ \left[\frac{g}{s}\right]$, was relatively high for a single cell. This may have further reduced the apparent fuel utilization by allowing a large excess of unreacted methanol to exit the cell.

To calculate the efficiency considering only the reacted methanol, the following equation was used:

$$\eta = \frac{i_{\max} \cdot V_{max} \cdot S_{cell}}{\dot{m}_{CH3OH,stoic} \cdot \Delta h_{CH3OH,reaction}} \qquad \text{(Eq.48)}$$

Where $\Delta h_{CH3OH,reaction}$ is the molar enthalpy of reaction, as defined in *Eq.32*. The reference values to calculate it were taken from *Table 10* and *Table 3*, and the resulting value is 726 kJ/mol.

The efficiency was also calculated using the actual flow rate of the methanol solution introduced $\dot{m}_{CH3OH,real}$, so taking into account the fuel utilization.

$$\eta = \frac{i_{\max} \cdot V_{max} \cdot S_{cell}}{\dot{m}_{CH3OH,real} \cdot \Delta h_{CH3OH,reaction}} \qquad \text{(Eq.49)}$$

The efficiency in *Eq.48* can be called stoichiometric efficiency and it provides insight into the intrinsic electrochemical behavior of the cell, whereas the second one (*Eq. 49*), called global efficiency, reflects its real operating performance, since it includes the fraction of fuel that actually reacts within the cell. These efficiencies can be seen for each DMFC in *Table 15* in the third and second column, respectively.

	FU (%)	Efficiency with the all amount of methanol feed (%)	Efficiency with only the reacting methanol (%)
DMFC 1 (2025-03-31)	2,53	0,46	17,96
DMFC 2 (2025-05-05)	3,15	0,54	17,19
DMFC 3 (2025-05-19)	2,43	0,44	17,95
DMFC 4 (2025-06-02)	2,18	0,54	24,62
DMFC 5 (2025-06-16)	2,57	0,57	21,99
DMFC 6 (2025-06-30)	2,48	0,60	24,28

Table 15. Fuel utilization (FU) and efficiency values for each DMFC, based on the maximum power point conditions (Excel)

Comparing the stoichiometric efficiencies (third column), the first three DMFCs show very similar values (around 17–18%), confirming comparable electrochemical behavior under identical operating conditions. However, looking at the last three cells, there is a clear improvement: DMFC 4, 5 and 6 reach values around and above 22%, demonstrating that the geometry of the anode flow field has a significant impact on methanol conversion and current generation.

The global efficiencies (second column), which account for fuel utilization, are considerably lower (0,44–0,60%) but reveal stronger differences between the cells. DMFC 6 achieves the highest overall efficiency (0,60%), followed by DMFC 5 (0,57%) and DMFC 2 (0,54%). DMFC 3 is the least efficient, confirming that flow field geometry strongly affects the methanol distribution and removal of CO_2 from the anode channels.

Since all the tested DMFCs adopt a single serpentine flow field design, the inlet and outlet position does not substantially change the flow pattern: the methanol solution is forced to travel along the entire anode surface in every configuration. What really differentiates the cells is therefore the geometry of the serpentine channels, specifically their number and cross section (width multiplied by depth). These parameters control both the flow velocity and pressure drop, as well as the effectiveness CO_2 removal from the anode.

By analyzing each DMFC in more detail, DMFC 1, with 21 channels of intermediate dimensions (width 1,133 mm, depth 0,9 mm), shows a balanced behavior: its channel cross section (1,02 mm^2) ensures good distribution and moderate pressure losses, though slightly lower overall performance compared to DMFC 2.

The latter shows the highest fuel utilization. In line with the expectations, it is the single cell with the largest number of channels (29) and the smallest channel width (0,825 mm), allowing for a more uniform and fine distribution of the fuel. Its narrow channel cross section (0,74 mm^2) increases the local velocity of the methanol solution, enhancing reactant supply and CO_2 removal. However, its stoichiometric efficiency is not the best, which results in a global efficiency equal to that of DMFC 4, despite their opposite fuel

utilization behavior. DMFC 4 indeed exhibits the lowest fuel utilization but the highest stoichiometric efficiency among all cells.

DMFC 3, characterized by the same channel width and number as DMFC 4 but with deeper channels (1,7 mm, cross section 1,40 mm^2), presents a slower flow, higher residence time and greater CO_2 accumulation, leading to poor methanol distribution and the lowest global efficiency.

The last two ones, DMFC 5 and DMFC 6, have the largest channel sections (1,93 mm^2) and deeper profiles (1,7 mm) that ensure a longer residence time of the methanol solution and better CO_2 removal. Among them, DMFC 6, with only 10 wide channels, achieves the highest global efficiency, likely due to the combination of a smoother flow path that leads to a reduced pressure drop and an effective gas removal, at least up to the maximum power density.

Overall, the results confirm that the cross section and number of the anode channels play a dominant role in determining the fuel distribution and utilization. Narrow and shallow channels, as in DMFC 2 favor higher fuel utilization due to enhanced methanol transport and uniform distribution, but they also increase pressure drop and may slightly limit the local reaction rate. In contrast, wider and deeper channels, as in DMFC 5 and 6, promote better CO_2 removal and higher stoichiometric efficiencies, but at the cost of less uniform flow distribution.

In conclusion, the optimal performance is achieved through a balance between these two effects. The results of DMFC 2 and DMFC 6 illustrate this trade off: DMFC 2 maximizes the fuel utilization through fine and dense channels, whereas DMFC 6 achieves the best overall efficiency by minimizing pressure losses and improving mass transport. This confirms that in serpentine flow fields, the interplay between channel cross section, flow velocity, and CO_2 removal efficiency determines the actual methanol utilization and, ultimately, the overall energy efficiency of the DMFC.

5.3 CO2 emissions

At the end of the data acquisition phase for the first tested DMFC, the analysis of CO_2 emissions was carried out. The DMFC 1 underwent a 30-minute galvanostatic procedure at a constant current of 0,8 A, using the Nova 2.1 software. This test aims to study the behavior of the cell under constant current conditions by observing the voltage variation over time, allowing for comparison with the polarization curve. Additionally, this analysis enables the evaluation of CO_2 emissions resulting from methanol oxidation.

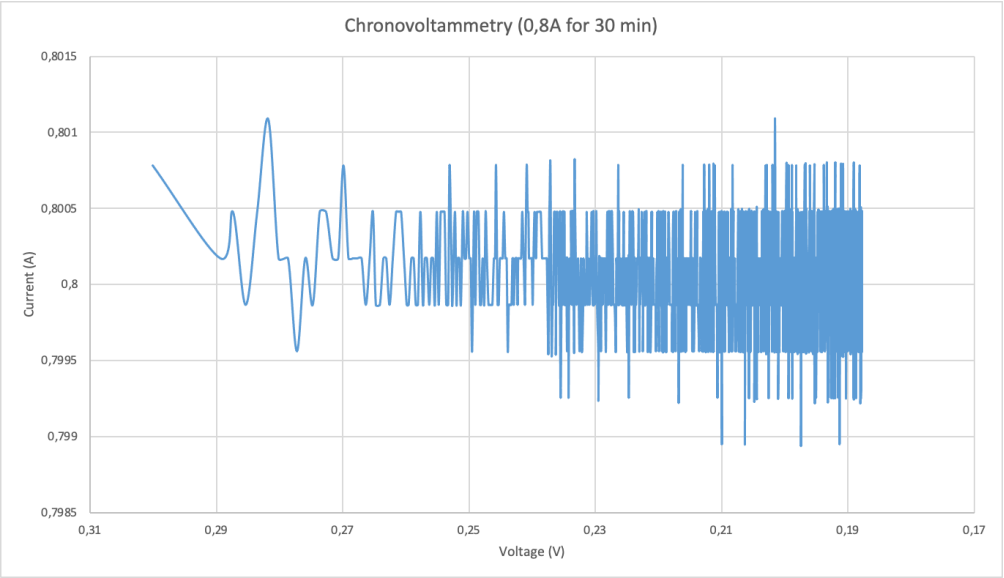

Figure 32. Chronovoltammetry test at 0,8A for 30min (Excel)

Figure 32 shows the chronovoltammetry curve obtained during the experiment. The x-axis displays the measured voltage values in decreasing order, while the y-axis shows the current, which was set at 0,8 A but exhibits small oscillations, particularly noticeable toward the end of the graph. This behavior may be attributed to instabilities in the instrument's control circuit, i.e., the galvanostat's difficulty in maintaining a constant current. Additionally, this effect can be explained by the formation of CO_2 bubbles, which hinder methanol transport and cause disturbances in the local fuel concentration, resulting in the observed current fluctuations.

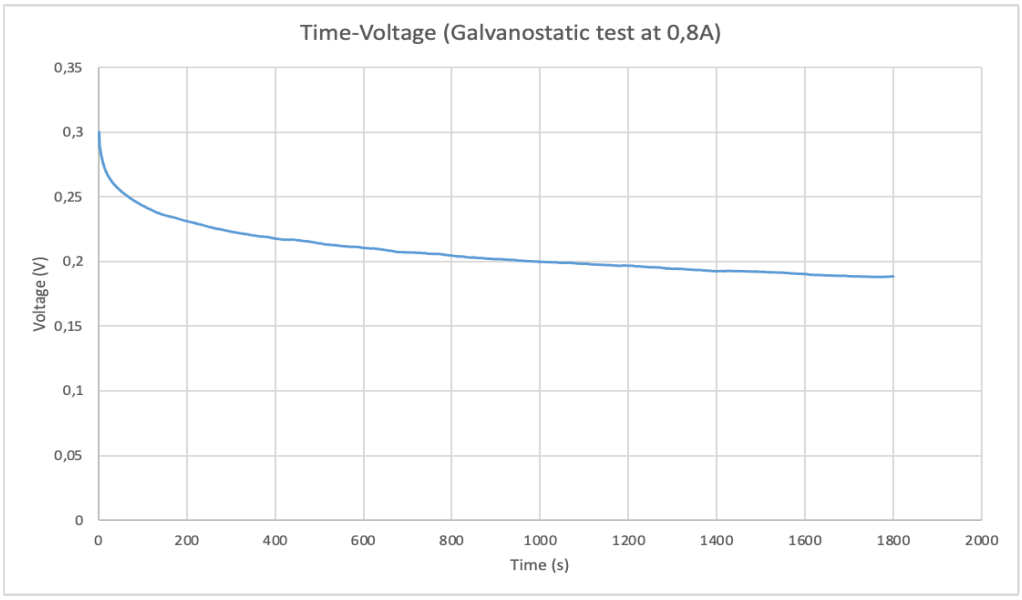

Figure 33. Time-Voltage graph from galvanostatic test (Excel)

By plotting the Time–Voltage graph shown in *Figure 33*, it is possible to observe that the voltage initially decreases sharply, then more gradually and slowly, reaching 0,188 V at the end of the test. This behavior is due to the progressive depletion of methanol at the anode over time, which leads to a reduction in the cell's reactivity and, consequently, a

drop in voltage. Additionally, the previously mentioned accumulation of CO_2 also contributes to the decline in cell performance.

By comparing the last polarization curve measured before this test, it can be observed that at a voltage of approximately 0,18 V, the corresponding current is about 0,8 A, which is exactly the current applied during the galvanostatic test. As said in the Section 4.3, each point on the curve represents the average current value over three minutes of operation. This means that the current recorded at 0,18 V reflects the same steady-state operating condition later reproduced in the galvanostatic test. In practice, the slight voltage decrease observed at the beginning of the galvanostatic test is due to the transient adjustment of the cell, but after this initial phase the voltage stabilizes around 0,18 V, the same value identified from the polarization curve, confirming that both experiments describe the same steady-state operating condition of the DMFC.

Current (A)	0,8
Time (s)	1800
Faraday constant (C/mol)	96485
Methanol stoichiometric mol (mol)	2,5E-03
CO2 stoichiometric mol (mol)	2,5E-03
CO2 produced (g)	1,1E-01
gCO2/kWh	1,5E+03

Table 16. Results obtained for the chronovoltammetry test: stoichiometric methanol and CO2 moles, CO2 produced in grams and CO2 emission in grams per kWh (Excel)

The stoichiometric amount of moles produced during this test, which corresponds to the amount of methanol consumed, can be calculated with the Faraday law as shown in *Table 16*. To determine the mass of CO_2 produced, the number of moles is multiplied by the molar mass of CO_2, which is 44 g/mol.

A useful parameter to assess is the amount of CO_2 emitted per kilowatt hour of electricity generated. This value turns out to be quite high, mainly due to the low electrical efficiency of the DMFC.

5.4 Economic analysis

The economic analysis is performed for both methanol utilization options: electricity generation through a Direct Methanol Fuel Cell (DMFC) and hydrogen production through a Methanol Electrolysis Cell (MEC). As previously mentioned, the entire methanol supply chain is considered in the calculation of both the Levelized Cost of Electricity

(LCOE) and the Levelized Cost of Hydrogen (LCOH). This means that all facilities required for methanol production, transportation, and final use are included in the analysis.

The main purpose of computing these two economic indicators, LCOE and LCOH, by accounting not only for the end-use plant but also for all the upstream infrastructures, is to assess the overall feasibility and potential economic advantage of producing methanol in a country with low renewable energy costs, transporting it by ship to a country where energy is more expensive, and using it in a DMFC or MEC system. The two countries selected for this case study are Brazil (production site) and Spain (consumption site), connected by a maritime route of 5.629 km.

The fundamental data and simplifications required to proceed with the economic analysis are reported below:

• electricity cost at production site: 40 USD/MWh [42];
• electricity cost at consumption site: 150 USD/MWh [42];
• all costs expressed in 2021 USD;
• plant lifetime: 30 years;
• capacity factor: 1;
• costs assumed constant over time: inflation is not included;
• real discount rate: 5%;
• hydrogen production at the source (from water electrolysis): 100 kt/year [42].

A capacity factor equal to 1 assumes that all process units operate continuously at full load throughout the entire year. This assumption is made to simplify the LCOE calculation and keep the focus on comparing the techno-economic performance of the system components.

A real discount rate of 5% is selected because it provides a reasonable representation of both the cost of capital and the investment risk associated with technologies that are still emerging and not yet fully commercial at this scale. In line with this approach, inflation is not considered in the base case, and all operating expenses are therefore assumed constant over the project lifetime. The objective of this simplification is to maintain a clear focus on the main economic drivers of the integrated methanol-to-power supply chain, while reducing the influence of secondary financial assumptions.

When analyzing the entire chain, the process begins with seawater desalination, which is required to supply purified water to the PEM electrolyzer. The electrolyzer produces hydrogen, which is then combined with CO_2 for methanol synthesis. The methanol is subsequently stored and shipped from the departure port to the arrival port. Once delivered, it is used either to produce hydrogen in a MEC or electricity in a DMFC system.

The reference DMFC considered in this study corresponds to the best-performing laboratory-tested unit. Two additional DMFC configurations with higher nominal power

are also evaluated for comparison purposes. Finally, a Carbon Capture and Storage (CCS) infrastructure based on Zeolite 13X technology is included in both scenarios to ensure consistency and complete carbon management.

It is important to emphasize that intermediate energy carriers within the chain are not double counted. For instance, since hydrogen is produced within the PEM electrolyzer, its cost is not considered as an external purchase in the methanol synthesis stage. The same principle applies to methanol when it is used in the DMFC or MEC plants.

5.4.1 Analysis of system facilities and scenario comparison

Detailed cost results for each plant are presented below, making use of the formulas already outlined in Section 3.

Starting with the infrastructures common to both electricity and hydrogen production scenarios, the analysis first focuses on the seawater desalination system.

Total water volumetric flow rate (m^3/y), Vt	2,3E+06
Total water volumetric flow rate (m^3/d), Vt	6301
Total water volumetric flow rate (m^3/s), Vt	0,073
Volumetric flow rate to the HPP (m^3/y), Vro	2E+06
Volumetric flow rate to the HPP(m^3/d), Vro	5479
Volumetric flow rate to the HPP (m^3/s), Vro	0,063
Volumetric flow rate to the turbine (m^3/s), Vbrine	0,035
Area RO (m^2)	37
Volumetric flow rate to the RO (m^3/d per module)	25
Number of RO	219

RO cost (USD)	81.096
PC_swip (USD)	1.296.880
PC_high pump (USD)	3.982
SWIP annaul energy cost (USD/year)	17.184
HPP annual energy cost (USD/year)	118.889
PC_Pelton turbine (USD)	181
Equipment purchase cost (CAPEX diretto)	1.382.139
TCI (=CAPEX diretto+CAPEX indiretto)	8.735.117
Chemical treatment cost (USD/y)	37.260
RO mambrane replacement cost (USD/y)	2.000
O&M equipment (USD)	1.222.916
Total annual energy cost (USD/y)	136.073
2 replacement of pumps and turbine in 30 years	43.368
OPEX (USD/y)	1.441.617

Table 17. Desalination plant results (Excel)

Table 17 summarizes the main parameters related to the total water flow required. This value is determined based on the need to produce 100 kt of hydrogen per year in the PEM electrolyzer. From this, the flow rates through the high-pressure pump and turbine are derived, allowing the determination of the number of reverse osmosis (RO) membranes required, and consequently, the overall equipment cost.

The direct CAPEX, which corresponds to the sum of all equipment costs, combined with the indirect CAPEX, results in a total CAPEX of 8.737.039 USD. The total OPEX is estimated at 1.441.886 USD/year, accounting for electricity consumption for plant operation, chemical treatment costs, RO membrane replacement, two equipment replacements for pumps and turbine.

The second facility in the chain is the water electrolyzer. Here, the desalinated water is fed into a PEM electrolyzer, where hydrogen production occurs at a rate of 100 kt/year.

Hydrogen production rate (kt/y)	100
Hydrogen production rate (kg/s)	3,17
H2O inlet flow rate (m^3/y)	9E+05
H2O inlet flow rate (kg/s)	28,54
O2 outlet flow rate (kg/s)	25,37
H2 Enthalpy (kJ/kg)	781
O2 Enthalpy (kJ/kg)	50,49
H20 Enthalpy (kJ/kg)	-15879
Electrical power consumed (kW)	5,71E+05
Total energy lost (kW)	5,69E+05
Electricity price USD/kWyear	350,4

Lifespan PEM (h)	100000
2 PEM replacements in 30 years(USD/y)	15.028.824
Yearly O&M (USD/year)	3.381.485
Electricity cost (USD/year)	200.138.778
OPEX (USD/y)	218.549.087
PEM cost (USD) = CAPEX	225.432.359

Table 18. Water electrolysis plant results (Excel)

A key aspect of this plant is determining the annual electricity cost, which represents one of the main components of the OPEX, together with the replacement cost of the PEM electrolyzer stack. The CAPEX is determined from the cost of the PEM electrolyzer, calculated using the correlations and equations provided in the Section 3.

The next facility is the methanol synthesis plant.

H2 reacting flow rate (kt/year)	100
Methanol production flow rate (kt/year)	520,83
Methanol production flow rate (kg/year)	5,21E+08
Methanol production flow rate (kg/s)	16,52
Required CO2 flow rate (kg/year)	7,28E+08
Required CO2 flow rate (kg/s)	23,07
Electrolyzer plant cost, C_ec (USD)	225.432.359
Methanol synthesis plant cost, C_synth (USD)	56.859.028
Annual energy consumption (MWh/year)	9,11E+04

Energy consumed cost (USD/year)	3.645.833
CO2 cost (USD/year)	16.662.135
2 replecaments in the lifetime (USD/y)	3.790.602
Yearly fixed O&M (USD/year)	852.885
TOTAL OPEX (USD/year)	24.951.456
CAPEX (USD) = C_synt	56.859.028

Table 19. Methanol synstesis plant results (Excel)

Similarly, the starting point is the annual hydrogen production (100 kt/year), from which the required CO_2 flow rate for methanol synthesis is derived.

As previously mentioned, the OPEX does not include the cost of hydrogen, since it is directly produced by the upstream electrolyzer. In other words, if the cost of producing hydrogen is already accounted for in the electrolysis plant, it cannot be included again as an input cost in the methanol synthesis step, this would otherwise lead to double counting. However, the CO_2 cost and the electricity consumption cost are both included in the operational expenditure. The corresponding CAPEX and OPEX values for this facility are summarized in *Table 19*.

Once the methanol is produced, it must be stored first at the departure terminal and later at the arrival one. The storage costs are estimated based on the total methanol volume handled. Since a fraction of the methanol is used as fuel for the vessel during transportation, the stored quantity at the arrival port is slightly lower than that at departure. The amount of methanol offloaded at the destination is calculated in the following section on transport logistics.

Methanol to be stored (kg)	9,44E+07
Storage cost at sending terminal (USD)	5.010.494.760

m_OL methanol unloaded from the ship (kg)	9,33E+07
Storage cost at receiving terminal (USD)	4.956.845.240

Table 20. Methanol storage costs (Excel)

These costs are overestimated since they do not consider scale effects. The original reference explicitly states that a 200 ton storage tank was used as cost basis.

For methanol transport, it is estimated that the annual production volume can be handled by a single ship performing 5 round trips per year. The cost per round

trip (including both outbound and return journeys) is calculated as 1.334.001 USD, leading to a total annual transport cost of 7.013.867 USD.

Distance covered (km)	5629
Time charter rate (USD/day)	19.000
Non-proportional voyage cost per land terminal (USD per round trip)	15.000
Roundtrip time (s)	6E+06
Roundtrip time(day)	69
m_L methanol loaded on the ship (kg)	9,5E+07
m_C methanol consumed on the ship (kg)	1,69E+06
m_OL methanol unloaded from the ship (kg)	9,33E+07
cr_c navigation consumption rate (kg/m)	0,52
cr_L;OL loading/unloading consumption rate (kg/s)	0,033
s_V (m/s)	1,9
Methanol production flow rate (kg/s)	16,52
Number of ship	1
cr_c with formula	0,03
Number of voyages in a year	5
Life cycle fleet cost (USD per roundtrip)	1.334.001
Annual ship transportation cost (USD/y)	7.013.867
Cost for the entire lifetime (USD)	210.415.995
Number of voyages in 30 years	158

Table 21. Methanol transport results (Excel)

An additional relevant metric is the specific transport cost, equal to 0,074 USD/kg of methanol transported. This value provides a useful benchmark for comparing alternative energy carriers or transport routes.

At this stage, the analysis focuses on the two methanol utilization options: Direct Methanol Fuel Cell (DMFC) for electricity production and Methanol Electrolysis Cell (MEC) for hydrogen generation.

The first set of calculations considers the lab DMFC with the highest overall efficiency, namely the DMFC 6 and then the DMFC described in Section 3.6 taken from reference [25].

DMFC 6 LAB	
Cells in the stack	10
Stack power (W)	2,18
Stacks required per 3kW module	1373
Cost per stack (USD/stack)	4,30
Cost per 3kW module (USD)	5898
Total cost per 3 kW module with BoP (USD)	14.160

DMFC DURAMET [25]	
Cells in the stack	10
Stack power (W)	200
Stacks required per 3kW module	15
Cost per stack (USD/stack)	393
Cost per 3kW module (USD)	5898
Total cost per 3 kW module with BoP (USD)	14.160

Table 22. Costs for stack and module with DMFC 6 from laboratory test and DMFC from reference [25] (Excel)

Initially, DMFC 6 is used as the reference unit. However, a single stack composed of 10 cells delivers a power output slightly above 2 W, which is two orders of magnitude lower than the performance achieved in the DURAMET Project [25]. Therefore, to assemble 3 kW modules using DMFC 6, a much larger number of stacks is required, specifically 1.373 stacks, compared to only 15 in the DURAMET configuration.

DMFC 6 LAB	
Module replacement cost (USD/y)	278.545
Methanol flow rate to the stack (g/s)	1,6E-02
Methanol flow rate to the 3kW module (kg/s)	0,022
Annual methanol consumption per 3kW module (kg/year)	6,93E+05
Total annual methanol consumption (kg/year)	4,91E+08
Number of required modules	708
Plant nominal power (kW)	2125
Annual electricity production (kWh/year)	1,86E+07
Costo totale plant = CAPEX (USD)	10.031.619
O&M (% CAPEX)	2%
O&M (USD/y)	200.632
OPEX (USD/y)	479.177

DMFC DURAMET [25]	
Module replacement cost (USD/y)	25.496.543
Methanol flow rate to the stack (g/s)	1,6E-02
Methanol flow rate to the 3kW module (kg/s)	2,40E-04
Annual methanol consumption per 3kW module (kg/year)	7569
Total annual methanol consumption (kg/year)	4,91E+08
Number of required modules	64.848
Plant nominal power (kW)	1,95E+05
Annual electricity production (kWh/year)	1,70E+09
CAPEX (USD)	918.242.850
O&M (% CAPEX)	2%
O&M (USD/y)	18.364.857
OPEX (USD/y)	43.861.400

Table 23. DMFC plants results with laboratory fuel cell 6 and reference [25] fuel cell (Excel)

It is assumed that all the methanol unloaded at the destination terminal during one year is consumed by the DMFC system. Moreover, the methanol flow rate per stack is assumed to be the same for both the 2 W laboratory cell and the 200 W prototype from literature. Therefore, with the same amount of methanol, the second configuration yields a much higher electricity production. This assumption was made because the methanol flow observed in laboratory experiments appears to be oversized compared to the actual fuel consumption.

As expected, the annual methanol consumption per 3 kW module is significantly higher in the laboratory-scale DMFC case, since a much larger number of stacks are needed to reach the same nominal power. A larger number of stacks means that the module in the lab DMFC case consumes much more methanol. Consequently, fewer 3 kW modules are required in this configuration to consume all the methanol transported by ship, leading to a lower CAPEX.

The methanol cost is not included in the economic assessment, for the same reason hydrogen was excluded earlier, that is to say to avoid double counting of internally produced intermediates. Therefore, in both cases, the OPEX was estimated by including the cost of module replacement, assumed to occur twice over the 30-year lifetime, and the operation and maintenance (O&M) costs, which were assumed to be equal to 2% of the CAPEX.

The resulting nominal annual power output of the entire plant is markedly different among the cases: 18,6 MWh/year for the laboratory scale DMFC and 1.704 MWh/year for the DURAMET configuration [25], indicating a much higher power generation capacity in the latter. Accordingly, both CAPEX and OPEX are considerably higher in the larger scale setup.

A third configuration considers a commercial DMFC, specifically the Efoy Pro 12000 Duo [40], which features a 500 W stack that can be combined to form 3 kW modules, similar to the previously analyzed systems.

DMFC Efoy Pro 12000 Duo [40]	
Stack power (W)	500
Stacks required per 3kW module	6
Stack cost (USD/stack) [41]	47.000
Total cost per module (USD)	282.000
Nominal consumption (l/kWh)	0,9

DMFC Efoy Pro 12000 Duo [40]	
Module replacement (USD/year)	82.096.699
Methanol flow rate to the 3kW module (kg/s)	3,56E-03
Annual methanol consumption per 3kW module (kg/year)	1,12E+05
Total annual methanol consumption (kg/year)	4,91E+08
Number of required modules	4367
Plant nominal power (kW)	1,31E+04
Annual electricity production (kWh/year)	1,15E+08
CAPEX (USD)	1.231.450.492
O&M (% CAPEX)	2%
O&M (USD)	24.629.010
OPEX (USD/y)	106.725.709

Table 24. Costs and results for plant with DMFC Efoy Pro 12000 Duo [40] (Excel)

In this case, the methanol consumption rate is directly provided by the technical datasheet, leading to a more accurate calculation of fuel use and performance. The annual energy production is approximately 115 MWh/year, while both CAPEX and OPEX are significantly lower compared to the previous cases.

Subsequently, the CCS block is evaluated for all three DMFC configurations.

CCS DMFC 6 LAB	
CO2 emitted per year (tonnelate/year)	2,71E+04
CO2 emitted per year (mol/year)	6,16E+08
AIC (USD/tCO2) [39]	175
AOC (USD/tCO2) [39]	48
CO2 captured(ton/y)	2,44E+04
OPEX (USD/y)	1.170.586
CAPEX (USD)	128.032.801

Table 25. CCS plant results for DMFC 6 from laboratory test (Excel)

CCS DMFC DURAMET [25]	
CO2 emitted per year (tonnelate/year)	2,48E+06
CO2 emitted per year (mol/year)	5,64E+10
AIC (USD/tCO2) [39]	175
AOC (USD/tCO2) [39]	48
CO2 captured(ton/y)	2,23E+06
OPEX (USD/y)	107.149.386
CAPEX (USD)	11.719.464.074

Table 26. CCS plant results for DMFC DURAMET [25] (Excel)

CCS DMFC EFOY PRO [40]	
CO2 emitted per year (tonnelate/year)	1,67E+05
CO2 emitted per year (mol/year)	3,8E+09
AIC (USD/tCO2) [39]	175
AOC (USD/tCO2) [39]	48
CO2 captured(ton/y)	1,5E+05
OPEX (USD/y)	7.215.447
CAPEX (USD)	789.189.500

Table 27. CCS plant results for DMFC Efoy Pro 12000 Duo [40] (Excel)

The highest CCS cost corresponds to the case using the DMFC from [25], as this configuration employs the largest number of modules and produces more, therefore emits the greatest quantity of CO_2.

To estimate the emitted CO_2, the results of the chronovoltammetry test were used, which relate grams of CO_2 to the energy produced (1.500 gCO_2/kWh). It should be noted that this test was performed only for DMFC 1, and the resulting emission value appears relatively high.

A 90% CO_2 recovery efficiency is assumed, meaning that 90% of the emitted CO_2 is captured by the CCS system.

The LCOE values for all three DMFC configurations (with and without CCS) are summarized in the following tables and figures.

	CAPEX (USD)	OPEX (USD/y)
DESALINATION	8.737.039	1.441.886
H2O ELECTROL	225.432.359	218.556.726
MeOH syntesis	56.859.028	24.951.456
MeOH storage sending	5.010.494.760	
MeOH storage receiving	4.956.845.240	
MeOH transport		7.013.867
DMFC 6 LAB	10.031.619	479.177
CCS	128.032.801	1.170.586
LCOE no CCS (USD/kWh)	49,44	
LCOE con CCS (USD/kWh)	49,95	

Table 28. LCOE cost breakdown for DMFC 6 from laboratory test (Excel)

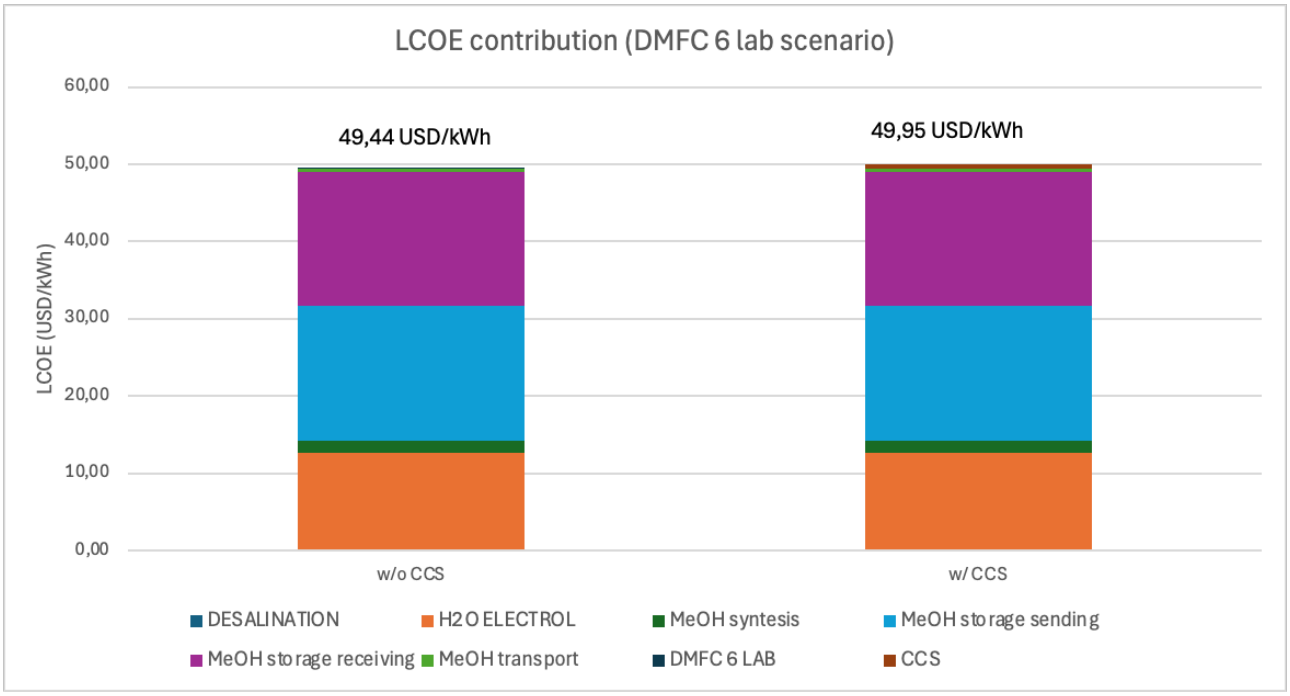

Figure 34. LCOE contribution by component for DMFC 6 (Excel)

The results show that for the lab scale DMFC 6, both LCOE values (with and without CCS) are significantly higher than current LCOE for renewable electricity, suggesting limited economic feasibility.

From *Figure 34*, the contributions of the different plants in the supply chain can be observed. The highest impacts on the LCOE come from methanol storage at both the departure and arrival ports, followed by the contribution from water electrolysis. Although the DMFC system has relatively high costs, it is not among the major contributors and does not significantly affect the final LCOE value. Desalination and transport also have minor contributions. Regarding the scenario with CCS, the addition of carbon capture slightly increases the LCOE, but not in a significant way.

	CAPEX (USD)	OPEX (USD/y)
DESALINATION	8.737.039	1.441.886
H2O ELECTROL	225.432.359	218.556.726
MeOH syntesis	56.859.028	24.951.456
MeOH storage sending	5.010.494.760	
MeOH storage receiving	4.956.845.240	
MeOH transport		7.013.867
DMFC DURAMET [25]	918.242.850	43.861.400
CCS	11.719.464.074	107.149.386
LCOE no CCS (USD/kWh)	0,60	
LCOE con CCS (USD/kWh)	1,11	

Table 29. LCOE cost breakdown for DMFC DURAMET [25] (Excel)

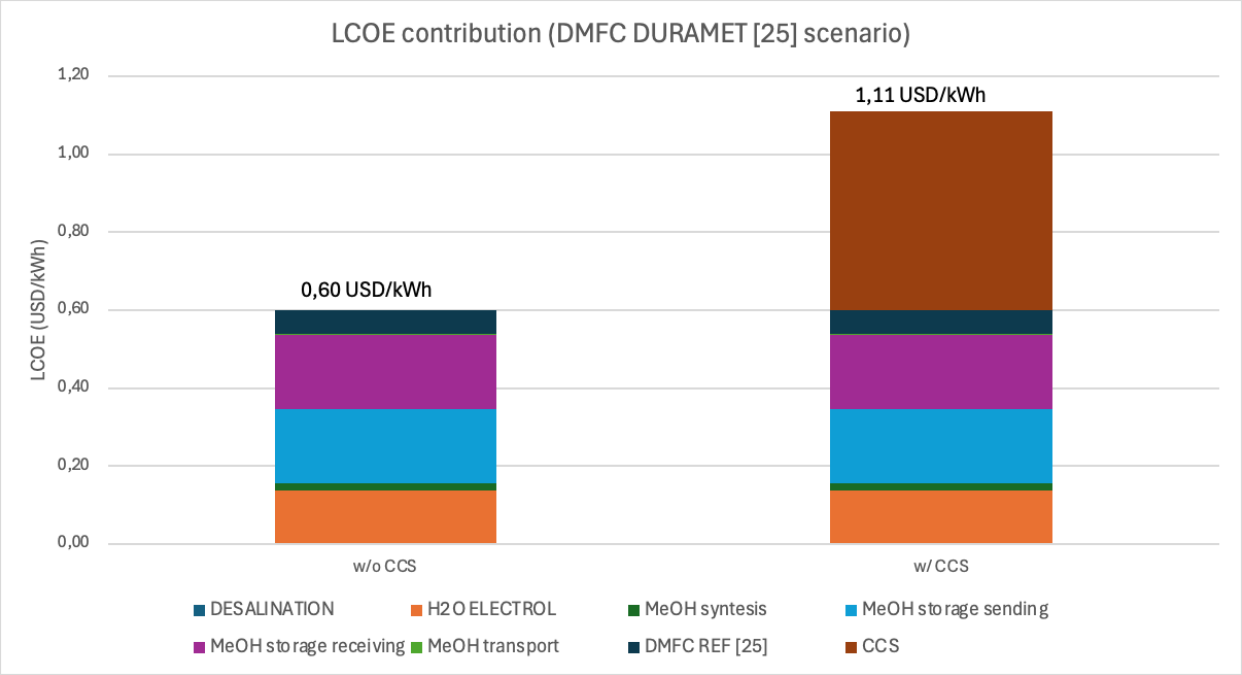

Figure 35. LCOE contribution by component for DMFC DURAMET [25] (Excel)

In the DURAMET-based configuration of reference [25], the resulting LCOE is substantially lower not because of reduced capital or operating costs, since the CAPEX and OPEX actually increase due to the larger number of 3 kW modules required to consume the same annual amount of methanol, but because the overall electricity production is dramatically higher. The prototype module described in reference [25] exhibits a significantly lower methanol consumption compared to the laboratory-scale unit; therefore, for the same annual methanol availability, the system can generate a much larger amount of electricity. This substantial increase in annual energy output is the primary driver behind the much lower and more reasonable LCOE obtained for this configuration.

Also in this case, the largest contribution to the LCOE in the scenario without CCS comes from storage and water electrolysis, although here the DMFC system shows a more evident impact. On the other hand, in the scenario with CCS the largest contribution is

given by the carbon capture unit itself, since this is the configuration in which the highest amount of electricity is produced and, consequently, the capture costs increase. Specifically, the LCOE increases from 0,60 USD/kWh to 1,11 USD/kWh when CCS is included, corresponding to a rise of 0,51 USD/kWh, which confirms the strong influence of carbon capture costs in this scenario.

	CAPEX (USD)	OPEX (USD/y)
DESALINATION	8.737.039	1.441.886
H2O ELECTROL	225.432.359	218.556.726
MeOH syntesis	56.859.028	24.951.456
MeOH storage sending	5.010.494.760	
MeOH storage receiving	4.956.845.240	
MeOH transport		7.013.867
DMFC Efoy Pro [40]	1.231.450.492	106.725.709
CCS	789.189.500	7.215.447
LCOE no CCS (USD/kWh)	9,64	
LCOE con CCS (USD/kWh)	10,15	

Table 30. LCOE cost breakdown for DMFC Efoy Pro 12000 Duo [40] (Excel)

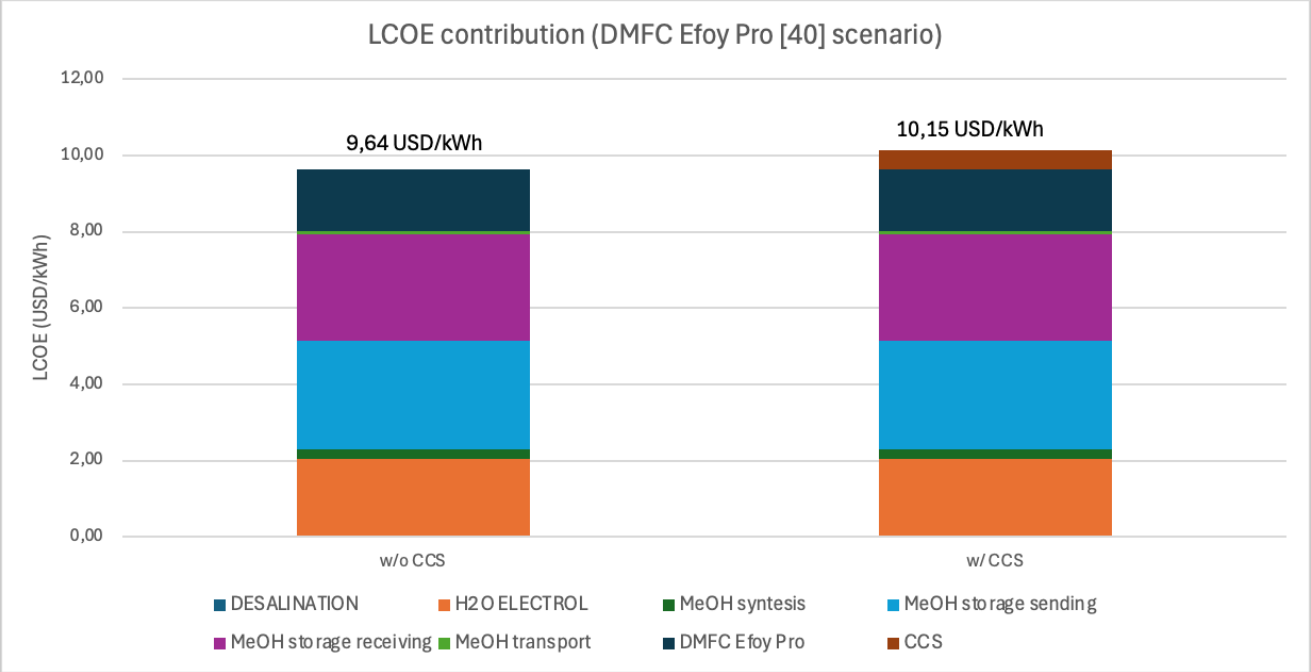

Figure 36. LCOE contribution by component for DMFC Efoy Pro 12000 Duo [40] (Excel)

Finally, for the commercial DMFC system (Efoy Pro 12000 Duo), the LCOE rises to about 9–10 USD/kWh. This relatively high value reflects the fact that the configuration considered here is based on the replication of many small commercial backup units, which are not designed for large-scale or continuous electricity generation.

In this scenario, an increase in the contribution from the DMFC system cost is observed. This is due to the fact that the stack cost used here is higher than in the previous two scenarios. As stated earlier, those scenarios used cost data from reference [25], which

were estimated based on manufacturing costs of the cell and the stack, material prices and the balance of plant. For this reason, the resulting value represents a minimum cost range. In contrast, for the DMFC Efoy Pro scenario the selling price of the system is considered, which is significantly higher and reflects the commercial cost of the technology. The LCOE increases from 9,64 USD/kWh to 10,15 USD/kWh when CCS is included. This increase remains moderate compared to the overall impact of methanol logistics.

In the second scenario, methanol is utilized in a Methanol Electrolysis Cell (MEC) for hydrogen production. As in the previous case, it is assumed that all the methanol unloaded at the destination port is consumed during one year of operation.

m_OL methanol unloaded from the ship in a year (kg)	4,91E+08
Annual hydrogen production (kg)	9,2E+07
H2 production flow rate (kg/s)	2,92
Methanol flow rate (kg/s)	15,56
H2O flow rate (kg/s)	8,75
CO2 flow rate (kg/s)	21,40
Hydrogen Enthalpy (kJ/kg)	786,5
Methanol Enthalpy (kJ/kg)	-7462,8
H20 Enthalpy (kJ/kg)	-15879,4
CO2 Enthalpy (kJ/kg)	-8897,2
Electrical power consumed (kW) in un anno	1,97E+05
Electrical consumption (kWh/year)	1,73E+09

Electricity Price USD/MWh	150
Electricity cost (USD/year)	259.400.175
Yearly O&M (USD/year)	6.800.033
OPEX (USD/y) no replacement	266.200.208
Electrolyzer cost = CAPEX (USD)	3.400.016.260

Table 31. Methanol Electrolysis cell plant results (Excel)

The system produces approximately 92.000 tonnes of hydrogen per year. The CAPEX is mainly determined by the electrolyzer cost, while the OPEX includes both the annual maintenance cost (assumed as 2% of CAPEX) and the electricity cost, which is particularly high about 259 million USD per year. The replacement is not considered in this case, since the cost of the electrolyzer is already very high.

The CCS block for the MEC case is evaluated using the same reference cost data adopted for the DMFC CCS system ([39]).

CO2 flow rate (kg/s)	21,4
Annual CO2 flow rate (t/year)	6,75E+05
CO2 emitted per year (mol/year)	1,53E+10
AIC (USD/tCO2) [39]	175
AOC (USD/tCO2) [39]	48
CO2 captured (ton/y)	6,07E+05
OPEX (USD/y)	29.154.030
CAPEX (USD)	3.188.722.025

Table 32. CCS plant results for MEC plant (Excel)

The resulting LCOH is slightly higher than the value reported in reference [42] (approximately 15 USD/kg H_2 compared to about 13 USD/kgH_2); nevertheless, it can still be considered consistent with the reference. When the CCS system is included, the LCOH increases up to 17,86 USD/kgH_2, which remains within the expected range for emerging methanol-based hydrogen pathways.

	CAPEX (USD)	OPEX (USD/y)
DESALINATION	8.735.117	1.441.617
H2O ELECTROL	225.432.359	218.549.087
MeOH syntesis	56.859.028	24.951.456
MeOH storage sending	5.010.494.760	-
MeOH storage receiving	4.956.845.240	-
MeOH transport	-	7.013.867
MEC	3.400.016.260	266.200.208
CCS	3.188.722.025	29.154.030
LCOH no CCS (USD/kgH2)	15,29	
LCOH con CCS (USD/kgH2)	17,86	

Table 33. LCOH cost breakdown (Excel)

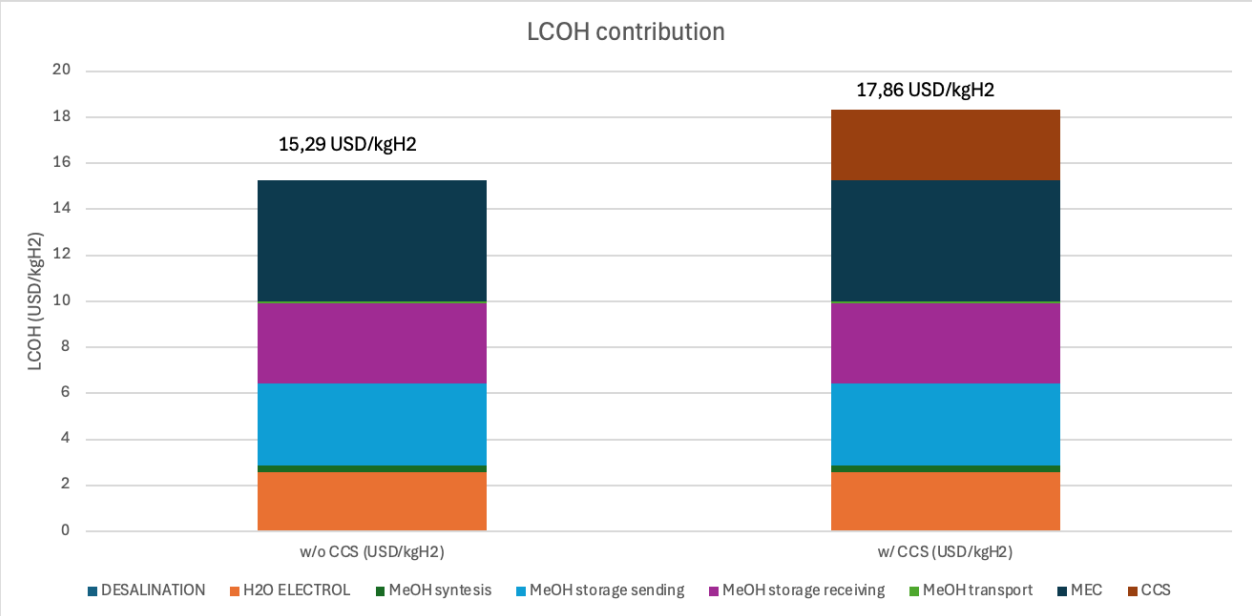

Figure 37. LCOH contribution by component (Excel)

Analyzing the contributions for this scenario, the largest share of the LCOH is again associated with methanol storage at both ports, while the MEC plant also accounts for a significant portion of the total cost. When CCS is included, the LCOH increases noticeably, highlighting the additional economic burden related to carbon capture. Specifically, the LCOH rises from 15,29 USD/kgH_2 to 17,86 USD/kgH_2, which corresponds to an increase of about 2,57 USD/kgH_2.

5.4.2 Sensitivity and cost-reduction analysis

A sensitivity analysis can be carried out for both scenarios.

Figure 38 shows the sensitivity of the LCOE to methanol price, calculated using the Efoy Pro 12000 Duo DMFC.

First, the methanol price resulting from the entire supply chain was determined. Considering all stages, from desalination to transport and storage at the destination terminal, the resulting LCOM is 1.873 USD/tonCH_3OH. This value is quite high and exceeds the current price range of e-methanol, which can reach up to 1.620 USD/tonCH_3OH [43]. However, it should be noted that the LCOM in this study includes not only production but also transport. In particular, storage has the largest cost contribution and is the main reason for the high final price. As previously discussed, the storage cost was likely overestimated and reducing it would lead to a noticeable decrease in the methanol price.

The dashed line indicates the Methanex European Posted Contract Price in the period April–June 2025 [44], which is considerably lower than the methanol price obtained from the Brazil-to-Spain supply chain.

Figure 38 also shows that the two cases (with and without CCS) do not differ substantially.

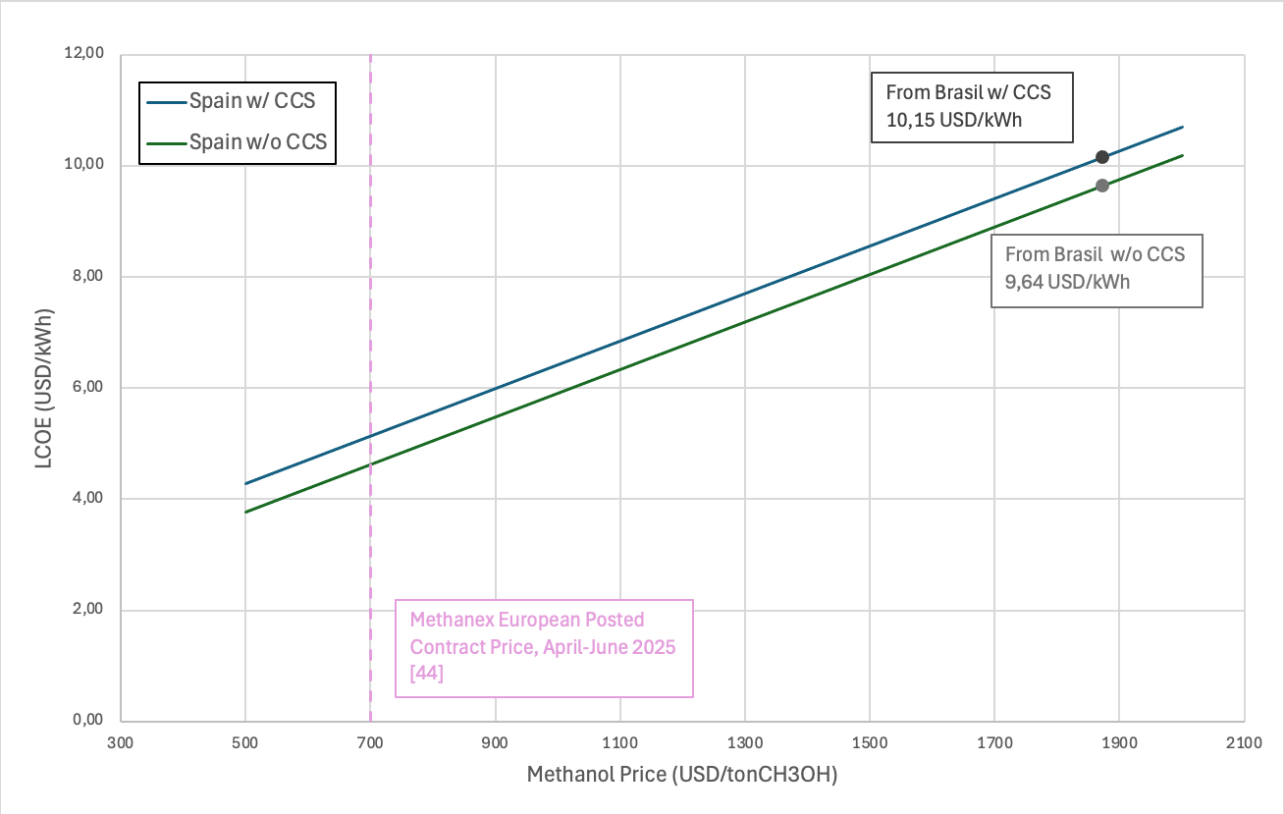

Figure 38. LCOE sensitivity to the methanol price (Excel)

Figure 39 shows the sensitivity of the LCOH to electricity price. In the case study analyzed, as mentioned at the beginning of this section, the electricity price in Spain was set at 150 USD/MWh. When this value decreases, the LCOH also declines.

It should be noted that, as in the previous scenario, the LCOH also depends on the methanol price; however, for the sensitivity analysis with respect to electricity price, the methanol price was kept constant.

In this scenario, the difference between the cases with and without CCS becomes more pronounced.

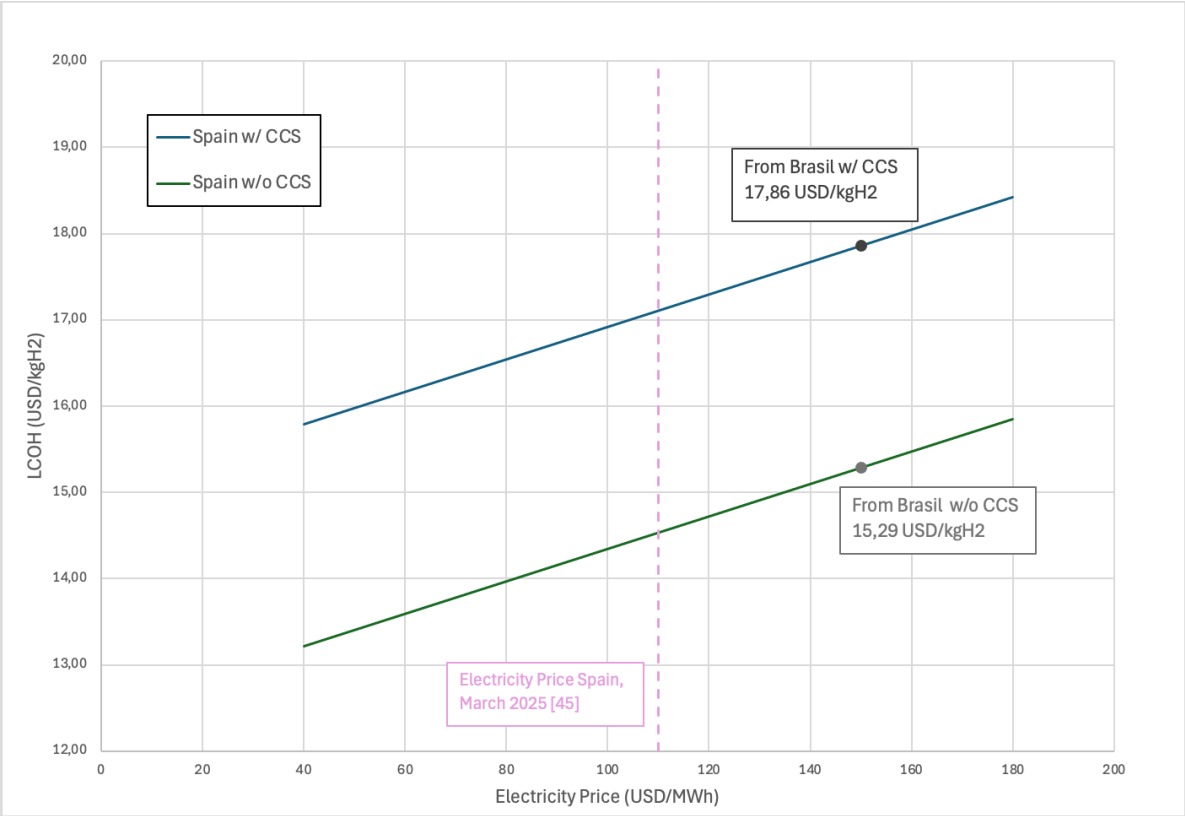

Figure 39. LCOH sensitivity to electricity price (Excel)

As a final analysis, the case in which the contribution of the most significant cost component (storage) is reduced has been investigated. Storage has a strong impact on the methanol price, which directly affects both LCOE and LCOH. Although the LCOH also depends on the electricity cost, the LCOM is influenced by the entire supply chain, whereas the electricity price in Spain is a fixed parameter that cannot be modified.

To identify ways to reduce overall costs across the supply chain, it is therefore essential to act on the storage block, which heavily affects the methanol import price from Brazil to Spain. The LCOM decreases from 1.873 USD/ton to 556 USD/ton simply by lowering storage costs, making methanol even more competitive than conventional methanol currently sold in Spain.

The storage cost used in this study refers to tanks with a capacity of 200 tons of methanol. The scale effect, which would significantly reduce costs for larger capacities, was not considered. Since the methanol produced in this study amounts to approximately 94.000 tons, storage costs become disproportionately high and represent the dominant contribution to both LCOE and LCOH.

Alternative cost data for larger storage capacities, closer to the scale of this study, were found in the literature and are reported in *Table 34*.

Capacity (ton)	Cost (USD/ton)	Ref.
200	53100	[32]
50000	144	[46]
100945	42	[47]

Table 34. Methanol storage cost for different tank capacities from literature data (Excel)

Using the price from reference [46] as a conservative estimate, both LCOE and LCOH were recalculated accordingly.

Figure 40 shows the same LCOE sensitivity analysis to methanol price previously presented in *Figure 38*, now including the results obtained with the reduced storage cost. In this case, the LCOE values decrease to 4,00 USD/kWh (without CCS) and 4,51 USD/kWh (with CCS). These values represent a substantial reduction compared to the initial results of 9,64 and 10,15 USD/kWh obtained with the higher methanol price (1.873 USD/tonCH_3OH). By lowering the storage cost, and consequently the overall methanol price, the system achieves an LCOE reduction of nearly 60%.

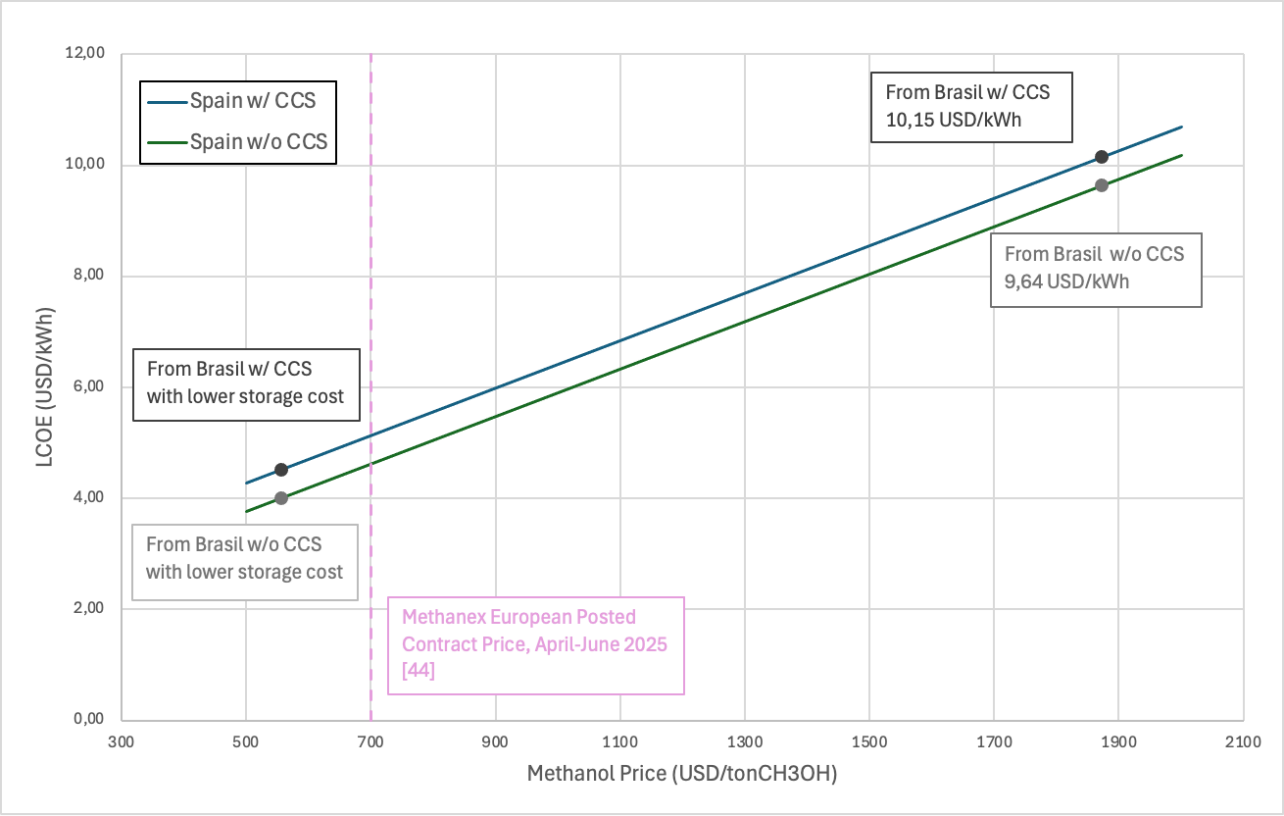

Figure 40. LCOE sensitivity to methanol price, showing the cases with reduced storage costs (Excel)

To evaluate how the methanol price reduction also affects hydrogen production costs, *Figure 41* presents the LCOH sensitivity to methanol price. As discussed earlier, the LCOH depends not only on the electricity price in the destination country (Spain), but also on the methanol cost, since hydrogen is produced through Methanol Electrolysis Cells (MECs). While the Spanish electricity price cannot be influenced by the supply chain, lowering the methanol price directly reduces LCOH.

The new LCOH values reach 8,26 USD/kgH_2 (without CCS) and 10,83 USD/kgH_2 (with CCS). These values show a clear improvement compared to the previous results (approximately 15–18 USD/kgH_2), confirming the strong influence of storage and methanol cost on the overall hydrogen production economics. Further improvements could be achieved by reducing the costs associated with the MEC plant, which, as shown in *Figure 37*, represents a significant contribution to the total LCOH.

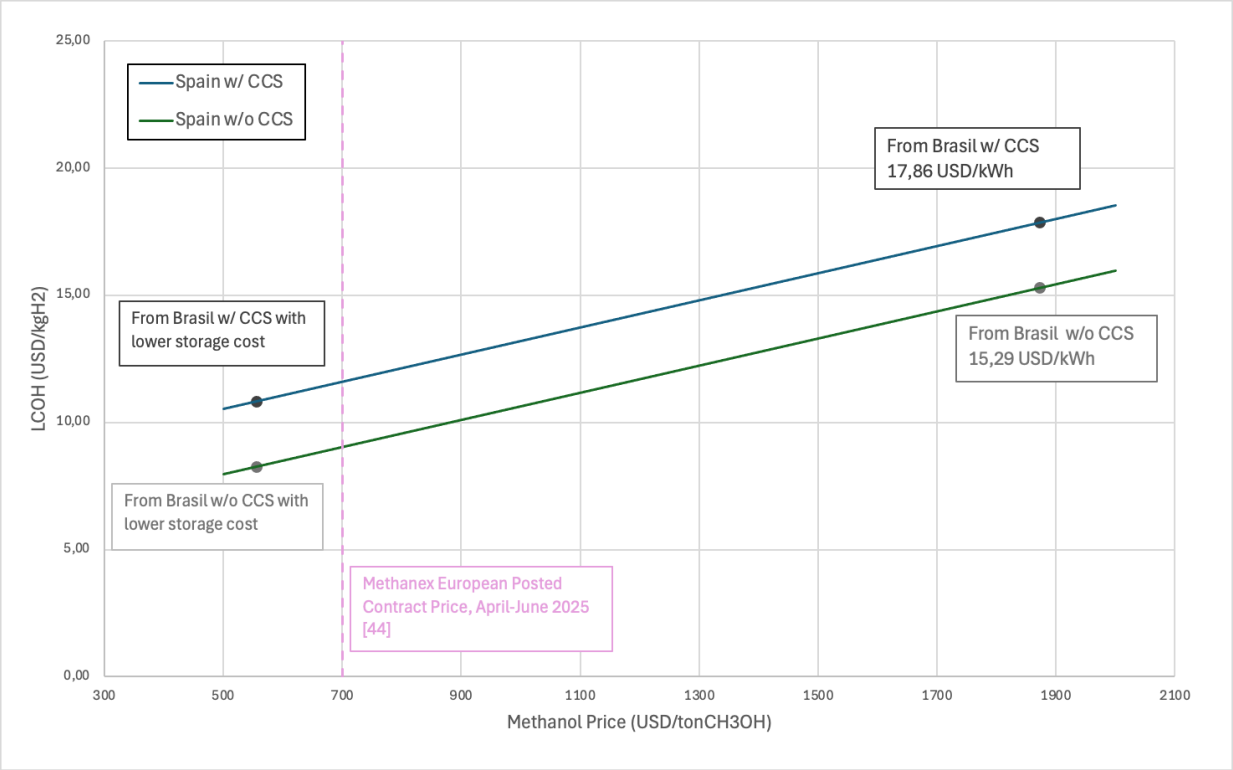

Figure 41. LCOH sensitivity to methanol price, showing the cases with reduced storage costs (Excel)

It is also possible to estimate the storage cost that would make the imported e-methanol supply chain from Brazil economically equivalent to the conventional methanol directly purchased in Spain.

Assuming a methanol price of 700 USD/tonCH_3OH, the resulting storage costs are 555.614.933 USD for the sending terminal and 561.628.531 USD for the receiving terminal. These values represent the maximum storage costs at which importing methanol from Brazil remains economically more favorable than using conventionally produced methanol in Spain. Beyond these thresholds, the imported supply chain would no longer be competitive.

6 CONCLUSION

It is now possible to summarize the main conclusions reached in this study.

Starting from the results of the experimental analysis, conducted to understand the behavior of different single DMFCs that differ in the geometry of the anode plate, the findings can be summarized as follows:

• All tested cells present a single-serpentine design; therefore, the inlet and outlet position does not significantly alter methanol flow distribution.

• The main geometric parameters influencing performance are the number of channels, their width and depth, which determine fuel distribution, flow velocity, and CO_2 removal.

• Cells with narrower and more numerous channels (such as DMFC 2) show more uniform methanol distribution and higher fuel utilization, but they suffer from higher pressure losses.

• Cells with wider and deeper channels (DMFC 5 and 6) promote better CO_2 removal and higher stoichiometric efficiency, but with less uniform fuel distribution.

• DMFC 3, with deep but narrow channels, presents lower overall efficiency due to CO_2 accumulation and slower flow.

• DMFC 6 is ultimately the most efficient in global terms, due to wider channels and fewer of them, ensuring lower pressure drop and more effective gas removal.

• In general, the balance between channel cross-section, flow velocity, and CO_2 removal determines the actual methanol utilization and thus the overall cell efficiency.

Since these tests were conducted on single cells, it remains important to extend the study to stack configurations, as only in these conditions do phenomena such as non-uniformity between cells, pressure gradient along the manifold, and thermal management issues emerge, which can significantly alter the real efficiency of the system. To obtain results applicable at plant scale, it is therefore essential to validate performance also in stack configuration, where fluid dynamic and thermal interactions become crucial to the overall performance.

The main objective of the economic analysis was to understand the cost-effectiveness of synthesizing and importing methanol from Brazil to Spain. The main results are:

• The production and supply chain of e-methanol from Brazil to Spain leads, in the base scenario, to a LCOM of 1873 USD/tonCH_3OH.

• Electricity production:

- With lab-scale DMFC:
  LCOE without CCS 49,44 USD/kWh;
  LCOE with CCS 49,45 USD/kWh.

These values are not economically competitive. However, the lab-scale DMFC system was designed to study the influence of anode plate geometry, not to optimize cost or efficiency for real applications.

- With reference DMFC from DURAMET project [25]:
  LCOE without CCS 0,60 USD/kWh;
  LCOE with CCS 1,11 USD/kWh.

This remarkably low LCOE results from the significantly lower methanol consumption of the DURAMET module, which allows a much higher annual electricity production for the same methanol availability.

- With commercial DMFC Efoy Pro 12000 DUO [40]:
  LCOE without CCS 9,64 USD/kWh;
  LCOE with CCS 10,15 USD/kWh.

• Hydrogen production:

- LCOH without CCS 15,29 USD/kgH_2;
- LCOH with CCS 17,86 USD/kgH_2.

The detailed cost analysis shows that storage is the dominant contribution in the entire supply chain.

By referring to literature values for storage plants scaled to the actual required capacity, the cost of methanol decreases to 556 USD/tonCH_3OH. With this reduced value, significantly lower costs are obtained:

• Electricity production with commercial DMFC:

LCOE without CCS 4,00 USD/kWh;
LCOE with CCS 4,51 USD/kWh.

• Hydrogen production:

LCOH without CCS 8,26 USD/kgH_2;
LCOH with CCS 10,83 USD/kgH_2.

The reduction is significant for both scenarios. However, in the case of electricity generation, even after the reduction, the LCOE values remain substantially higher than the global average LCOE of renewable sources such as wind and solar, typically ranging from 0,034 to 0,043 USD/kWh[48]. Blanco et al. [49] analyzed electricity production from methanol via the electrochemical pathway and reported an LCOE equal to 0,6 EUR/kWh, significantly lower than the values obtained in this study with the commercial Efoy Pro, also after storage cost reduction. However, their work explicitly notes that such

electrochemical processes are mainly suitable for portable applications or stationary systems with relatively low energy demand, and the system they consider operates at a scale of 1 MW. The configuration adopted in this work relies on the replication of many small commercial Efoy Pro 12000 Duo DMFC units originally intended for portable or low-power backup applications. When such devices are scaled up to achieve an annual production of around 115 MWh, the resulting LCOE naturally becomes considerably higher. A similar consideration applies to the other DMFC systems analysed in this study: they all operate at a scale and with characteristics typical of small, low-power devices, and when extrapolated to large energy outputs their economics inevitably become significantly less favourable compared to purpose-built large-scale systems.

This discrepancy is expected, since DMFC technology for stationary power generation is still at a pre-commercial stage, characterized by limited technological maturity and relatively high capital and operational costs, particularly when scaled beyond small or portable systems.

In contrast, the LCOH obtained here, after methanol cost reduction, becomes closer to the typical values reported in Europe for hydrogen produced from water electrolysis directly coupled to renewable energy sources, with an average value of 6,71 EUR/kgH_2 in 2024 [50].

Finally, it was calculated that, in order to reach cost parity with methanol purchased directly in Spain at 700 USD/tonCH_3OH, it is necessary that:

- Storage capacity at departure terminal should be 556 million USD;
- Storage capacity at arrival terminal should be 562 million USD.

If these thresholds are exceeded, importing methanol from Brazil becomes less convenient than purchasing conventional methanol directly in Spain, assuming that all other costs in the supply chain remain unchanged.

Furthermore, as already anticipated in the introduction, a potential future development of this work concerns the integration of circular economy principles within the methanol-based energy chain. Specifically, the CO_2 captured in the final stage of the process could be reused as feedstock in the methanol synthesis step. This would avoid the need to purchase additional CO_2 from external suppliers, thereby reducing the operating costs associated with methanol synthesis and, consequently, lowering the final LCOE or LCOH of the system. This closed loop approach would not only enhance the overall sustainability of the process but also improve its economic feasibility, making it a promising direction for further investigation.

7 REFERENCES

[1] Gabriel Blanco. CONSIDERATION OF THE IPCC 5th REPORT ON MITIGATION. Secretariat of the Convention on Biological Diversity (2017) The Lima Declaration on Biodiversity and Climate Change: Contributions from Science to Policy for Sustainable Development. Technical Series No.89. (Eds L. Rodríguez & I. Anderson) Secretariat of the Convention on Biological Diversity, Montreal, 156 pages.

[2] Loiy Al-Ghussain. Global Warming: Review on Driving Forces and Mitigation. Wiley Online Library (wileyonlinelibrary.com). DOI 10.1002/ep.13041

[3] Dina G. Boer; Jort Langerak; Paolo P. Pescarmona. Zeolites as Selective Adsorbents for CO_2 Separation. *ACS Appl. Energy Mater.* 2023, 6, 2634-2656.

[4] Hermann Harde. Scrutinizing the carbon cycle and CO_2 residence time in the atmosphere. Global and Planetary Change 152 (2017) 19–26.

[5] Rosenow J (2022). Europe on the way to net zero: What challenges and opportunities? PLOS Clim 1(7): e0000058. https://doi.org/10.1371/ journal.pclm.0000058.

[6] Jeffrey Y. Tsao, E. Fred Schubert, Roger Fourquet, matthew Lave. The electrification of energy: Long.term trends and opportunities. MRS Energy & Sustainability: A Review Journal page 1 of 14 © Materials Research Society, 2018 doi:10.1557/mre.2018.6.

[7] Chong Wei Ong, Jian-Xun Lin, Meng-Lin Tsai, Ka Sin Thoe, Cheng-Liang Chen. Techno-economic and carbon emission analyses of a methanol-based international renewable energy supply chain. International Journal of Hydrogen Energy 49 (2024) 1572–1585.

[8] Krishnaswamy Sankaran. Turning black to green: Circular economy of industrial carbon emissions. Energy for Sustainable Development 74 (2023) 463–470.

[9] Felix Schorn, Janos L. Breuer, Remzi Can Samsun, Thorsten Schnorbus, Benedikt Heuser, Ralf Peters, Detlef Stolten. Methanol as a renewable energy carrier: An assessment of production and transportation costs for selected global locations. Advances in Applied Energy 3 (2021) 100050.

[10] Huairong Zhou, Abo Cao, Wenliang Meng, Dongliang Wang, Guixian Li, Siyu Yang. Process integration and analysis of coupling solid oxide electrolysis cell (SOEC) and CO_2 to methanol. Energy 307 (2024) 132652.

[11] Jannis Hack, Nobutaka Maeda, and Daniel M. Meier. Review on CO_2 Capture Using Amine-Functionalized Materials. *ACS Omega* 2022, 7, 39520-39530.

[12] Muhammad Waseem, Mohamed Al-Marzouqi, Nayef Ghasem. A review of catalytically enhanced CO2-rich amine solutions regeneration. Journal of Environmental Chemical Engineering 11 (2023) 110188.

[13] Jinyue Cui, Muhammad Aziz. Techno-economic analysis of hydrogen transportation infrastructure using ammonia and methanol. international journal of hydrogen energy 48 (2023) 15737e15747.

[14] Oscar Santiago, Jaime Gonzalez-Domínguez, Manuel Botejara-Antúnez, Emilio Navarro, Justo García-Sanz-Calcedo, Teresa J. Leo. Environmental impact assessment of a direct methanol fuel cell and strategic mitigation guidelines. Renewable Energy 237 (2024) 121697.

[15] Vladimir L. Meca, Rafael d'Amore-Domenech, Antonio Crucelaegui, and Teresa J. Leo. Large-Scale Maritime Transport of Hydrogen: economic Comparison of Liquid Hydrogen and Methanol. *ACS Sustainable Chem. Eng.* 2022, 10, 4300-4311.

[16] Jian-Xun Lin, Wei-Jyun Wang, Bor-Yih Yu, Chong Wei Ong, Cheng-Liang Chen. Intensification of the CO2-capturing methanol steam reforming process: A comprehensive analysis of energy, economic and environmental impacts. Separation and Purification Technology 347 (2024) 127612.

[17] Qianqian Song, Rodrigo Rivera Tinoco, Haiping Yang, Qing Yang, Hao Jiang, Yingquan Chen, Hanping Che. A comparative study on energy efficiency of the maritime supply chains for liquefied hydrogen, ammonia, methanol and natural gas. Carbon Capture Science & Technology 4 (2022) 100056.

[18] Peeyush Phogat, Bhawana Chand, Shreya, Ranjana Jha, Sukhvir Singh. Hydrogen and methanol fuel cells: A comprehensive analysis of challenges, advances, and future prospects in clean energy. International Journal of Hydrogen Energy 109 (2025) 465–485.

[19] Ahmed, A.A.; Al Labadidi, M.; Hamada, A.T.; Orhan, M.F. Design and Utilization of a Direct Methanol Fuel Cell. Membranes 2022, 12,1266. https://doi.org/10.3390/ membranes12121266.

[20] M.S. Alias, S.K. Kamarudin, A.M. Zainoodin, M.S. Masdar. Active direct methanol fuel cell: An overview. international journal of hydrogen energy 45 (2020) 19620e19641

[21] Yaqoob L, Noor T, Iqbal N. Recent progress in development of efficient electrocatalyst for methanol oxidation reaction in direct methanol fuel cell. Int J Energy Res. 2021;45:6550–6583. https://doi.org/10.1002/ er.6316

[22] Meital Goor, Svetlana Menkin, Emanuel Peled. High power direct methanol fuel cell for mobility and portable applications. international journal of hydrogen energy 44 (2019) 3138e3143.

[23] Prabhuram Joghee, Jennifer Nekuda Malik, Svitlana Pylypenko, Ryan O'Hayre. A review on direct methanol fuel cells – In the perspective of energy and sustainability. MRS Energy & Sustainability: A Review Journal page 1 of 31 © Materials Research Society, 2015 doi:10.1557/mre.2015.4.

[24] Muhammad Qasim, Mohamed Badrelzaman, Noora N. Darwish, Naif A. Darwish, Nidal Hilal. Reverse osmosis desalination: A state-of-the-art review. Desalination 459 (2019) 59–104.

[25] Mauro Francesco Sgroi, Furio Zedde, Orazio Barbera, Alessandro Stassi, David Sebastián, Francesco Lufrano, Vincenzo Baglio, Antonino Salvatore Aricò, Jacob Linder Bonde and Michael Schuster. Cost Analysis of Direct Methanol Fuel Cell Stacks for Mass Production. Energies 2016, 9, 1008; doi:10.3390/en9121008.

[26] Gangadharan Sasikumar*, Arunachalam Muthumeenal, Sethu Sundar Pethaiah, Nachiappan Nachiappan, Rengarajan Balaji. Aqueous methanol eletrolysis using proton conducting membrane for hydrogen production. International journal of hydrogen energy 33 (2008) 5905–5910.

[27] Sethu Sundar Pethaiah, Kishor Kumar Sadasivuni , Arunkumar Jayakumar, Deepalekshmi Ponnamma, Chandra Sekhar Tiwary and Gangadharan Sasikumar. Methanol Electrolysis for Hydrogen Production Using Polymer Electrolyte Membrane: A Mini-Review. Energies 2020, 13, 5879. doi:10.3390/en13225879.

[28] Tetsuo Take, Kazuhiko Tsurutani, Minoru Umeda. Hydrogen production by methanol–water solution electrolysis. Journal of Power Sources 164 (2007) 9–16. doi:10.1016/j.jpowsour.2006.10.011.

[29] Faisal,M.;Pamungkas, A.Z.; Krisnandi, Y.K. Study of Amine Functionalized Mesoporous Carbon as CO2 Storage Materials. Processes 2021, 9, 456. https://doi.org/10.3390/pr9030456 .

[30] Rana, A.; Andino, J.M. A Review of Materials for Carbon Dioxide Capture. Catalysts 2025, 15, 273. https://doi.org/10.3390/catal15030273 .

[31] V. Indira, K. Abhitha. A review on recent developments in Zeolite A synthesis for improved carbon dioxide capture: Implications for the water-energy nexus. Energy Nexus 7 (2022) 100095.

[32] Vladimir L. Meca, Rafael d'Amore-Domenech, Antonio Crucelaegui, Teresa J. Leo. Supporting information of Large-scale maritime transport of hydrogen: economic comparison of liquid hydrogen and methanol. https://pubs.acs.org/doi/10.1021/acssuschemeng.2c00694.

[33] Prof. Massimo Santarelli, Ph.D., DENER Politecnico di Torino, Celle a combustibile a membrana polimerica Descrizione generale della cella e dei suoi principi di funzionamento.

[34] Michaelides, E.E. Power and Energy Requirements for Carbon Capture and Sequestration. Thermo 2025,5,8. https://doi.org/10.3390/thermo5010008 .

[35] Wan Yun Hong. A techno-economic review on carbon capture, utilisation and storage systems for achieving a net-zero CO2 emissions future. Carbon Capture Science & Technology 3 (2022) 100044. https://doi.org/10.1016/j.ccst.2022.100044 .

[36] Narges Sadat Nazari, Fatemeh Afshari, Mahdi Mahmoudkhani, Ahad Ghaemi. Optimization of carbon dioxide adsorption from industrial flue gas using zeolite 13X: A simulation study with Aspen Adsorption and response surface methodology. Results in Engineering 24 (2024) 103206. https://doi.org/10.1016/j.rineng.2024.103206 .

[37] R. Gonzalez-Olmos, A. Gutierrez-Ortega, J. Sempere, R. Nomen. Zeolite versus carbon adsorbents in carbon capture: A comparison from an operational and life cycle perspective. Journal of CO2 Utilization 55 (2022) 101791. https://doi.org/10.1016/j.jcou.2021.101791.

[38] Farzan Kazemifar. A review of technologies for carbon capture, sequestration, and utilization: Cost, capacity, and technology readiness. Greenhouse. Gas. Sci. Technol. 12:200–230 (2022); DOI: 10.1002/ghg.2131.

[39] Stefano E. Zanco, José-Francisco Pérez-Calvo, Antonio Gasós, Beatrice Cordiano, Viola Becattini, and Marco Mazzotti. Postcombustion CO2 Capture: A Comparative Techno-Economic Assessment of Three Technologies Using a Solvent, an Adsorbent, and a Membrane. ACS Eng. Au 2021, 1, 50−72. https://doi.org/10.1021/acsengineeringau.1c00002

[40] Enrico Berretti, Luigi Osmieri, Vincenzo Baglio, Hamish A. Miller, Jonathan Filippi, Francesco Vizza, Monica Santamaria, Stefania Specchia, Carlo Santoro, Alessandro Lavacchi. Direct Alcohol Fuel Cells: A Comparative Review of Acidic and Alkaline Systems. Electrochemical Energy Reviews (2023) 6:30 https://doi.org/10.1007/s41918-023-00189-3 .

[41] https://www.awilco.dk/product/fuel-cells/methanol-fuel-cells/efoy-pro-fuel-cells/efoy-fuel-cell-pro-12000-duo-set-24v-dc-500w/

[42] Vladimir Luis Meca López. Methanol electrolyser and direct methanol fuel cell for marine applications. DOCTORAL THESIS, Madrid 2024.

[43] IRENA AND METHANOL INSTITUTE (20219. Innovatio Outlook: Renewable Methanol. International Renewable Energy Agency, Abu Dhabi. https://www.irena.org/-/media/Files/IRENA/Agency/Publication/2021/Jan/IRENA_Innovation_Renewable_Methanol_2021.pdf.

[44] https://www.methanex.com/wp-content/uploads/Mx-Price-Sheet-May-29-2025.pdf

[45] https://www.intratec.us/solutions/energy-prices-markets/commodity/electricity-price-spain

[46] Lloyd's Register, UMAS. Fuel production cost estimates and assumptions. https://sustainableworldports.org/wp-content/uploads/Lloyds-Register_2019_Fuel-production-cost-estimates-and-assumptions-report.pdf

[47] Tansu Galimova, Mahdi Fasihi, Dmitrii Bogdanov, Gabriel Lopez, Christian Breyer. Analysis of green e-methanol supply costs: Domestic production in Europe versus imports via pipeline and sea shipping. Renewable Energy 241 (2025) 122336. https://doi.org/10.1016/j.renene.2024.122336

[48] IRENA (2025), Renewable power generation costs in 2024, International Renewable Energy Agency, Abu Dhabi. https://www.irena.org/-/media/Files/IRENA/Agency/Publication/2025/Jul/IRENA_TEC_RPGC_in_2024_2025.pdf

[49] Elena C. Blanco, Antonio Sáncheza, Mariano Martína, Pastora Vega. Methanol and ammonia as emerging green fuels: Evaluation of a new power generation paradigm. Renewable and Sustainable Energy Reviews 175 (2023) 113195. https://doi.org/10.1016/j.rser.2023.113195

[50] https://observatory.clean-hydrogen.europa.eu/index.php/hydrogen-landscape/production-trade-and-cost/cost-hydrogen-production